People's Democratic Republic of Algeria
Ministry of Higher Education and Scientific Research

Mohamed Boudiaf University of M’sila - M'sila

Faculty of Sciences
Physics Department

Serial number: ……………………
Enrolment number: D.PHC/3C/01/20

Thesis

Submitted for the diploma of
3rd cycle Doctorate degree

Major: Physics
Speciality: Condensed matter physics

THEME

Influence of additions on the preparation of ye’elimite from natural phosphate

Presented By:
Zeyneb HAMMOU
Defended on: 29/06/2025

In front of the jury composed of:

Name & First name	Grade	Establishment	Quality
Mayouf SI ABDALLAH	Professor	Univ. of M’sila	President
Hocine BELHOUCHET	Professor	Univ. of M’sila	Supervisor
Younes BENARIOUA	Professor	Univ. of M’sila	Examiner
Mohamed Redda BOUDCHICHA	Senior Lecturer	ENP. of Constantine	Examiner

Academic year: **2024 /2025**

THANKS

Primarily, I express my deepest gratitude to Almighty **Allah** for granting me good health, courage, patience, and the willpower that enabled me to successfully finish this project.

I would like to thank my heartfelt gratitude to **My Parents** for their boundless patience and for creating an optimal working environment. This project would not have been possible without their unwavering support.

I extend my heartfelt appreciation to Pr. **Hocine BELHOUCHET**, my supervisor, for proposing and overseeing this project. I truly appreciate his dedication in providing me with the essential resources, his trust in my capabilities, and the time he devoted to guiding me. I appreciate his assistance, guidance, expertise, and his humility.

I express my gratitude to Mr. **Mayouf SI ABDALLAH**, professor at Mohamed Boudiaf-M’sila University, for accepting the presidency of the jury responsible for examining this modest work.

I express my gratitude to Mr. **Younes BENARIOUA**, professor at Mohamed Boudiaf-M’sila University, and Mr. **Mohamed Redda BOUDCHICHA**, senior lecturer at the National Polytechnic School of Constantine, for accepting to judge this modest work.

I extend my appreciation to Professor **Mohammad Refa'at A. Rahim Irshidat** at Qatar University for offering me the opportunity to participate in a month-long training program and for his collaboration and support. I would also like to thank all the CAM staff for their cooperation and guidance. Special thanks to **Mujaheed Pasha** at Hamad Bin Khalifa University in Qatar for his valuable collaboration.

My sincere thanks also go to everyone who supported me directly or indirectly, including the engineers **Mahmoud Ouahchi** and **Meftah Messeguem** at Lafarge Holcim in M'sila. I would also like to thank **Dr. Aicha Mohadi** in the Physics Lab for her continuous support, as well as to all my colleagues.

Finally, I would like to express my gratitude to my sister, **Sarah Hammou**, and her husband, **Abdelkader Zerguine**, for their unwavering support. May Allah fill their hearts with happiness.

To: My Parents

Contents

CHAPTER I : Bibliographic overview

CHAPTER II: Materials and experimental techniques

CHAPTER III: Results and Discussions

***Part 01:** The effect of quartz on natural fluorapatite decomposition during the preparation of calcium sulfoaluminate-based multiphase composites*

Part 02: *The influence of magnesium oxide on natural fluorapatite decomposition during the preparation of spinel-ye'elimite based multi-phase composites.*

Appendix

The subsequent enumeration delineates the symbols and abbreviations employed across the entirety of the thesis.

- ✓ **Symbols and phases of cement**

Symbols and phases	Chemical formula	Name
A	Al_2O_3	Aluminium oxide
C	CaO	Calcium oxide
$	SO_3	Sulfur trioxide
S	SiO_2	Silicium oxide
H	H_2O	Water
M	MgO	Magnesium oxide
C_3S	Ca_3SiO_5	Tricalcium silicate (Alite)
C_2S	Ca_2SiO_4	Dicalcium silicate, (Belite)
C_3A	$Ca_3Al_2O_6$	Tricalcium aluminate, (Celite)
CA_2	$CaAl_4O_7$	Calcium Dialuminate, (Grossite)
$C_4A_3$$	$Ca_4\ (Al_6O_{12})\ SO_4$	Ye'elimite
C_2AS	$Ca_2Al_2SiO_7$	Gehlenite

- ✓ **ICDD codes and chemical formula for phases mineral.**

Mineral phase	Chemical formula	ICDD Code
Fluorapatite	$Ca_5(PO_4\ )_3F$	015-0876
Alumina	Al_2O_3	042-1468
Ye'elimite	$Ca_4Al_6O_{12}(SO_4)$	016-0440
Spinel	$MgAl_2O_4$	021-1152
Hibonite	$CaAl_{12}O_{19}$	038-0470
Grossite	$CaAl_4O_7$	023-1037
β-TCP	$Ca_3(PO_4)_2$	009-0169
Anhydrite	$CaSO_4$	006-0226
Gehlenite	$Ca_2Al_2SiO_7$	035-0755
Berlinite	$AlPO_4$	076-0228
Wollastonite	$Ca_6Si_6O_{18}$	043-1460

- ✓ **Members of the apatite family**

  MCPM: Monocalcium Phosphate Monohydrate.

  DCPD: Dicalcium Phosphate Dihydrate.

  DCPA: Dicalcium Phosphate Anhydrous.

  OCP: Octacalcium Phosphate.

  β-TCP: Beta Tricalcium Phosphate.

  α-TCP: Alpha Tricalcium Phosphate.

  HAp: Hydroxyapatite.

  FAp: Fluorapatite.

  OAp: Oxyapatite.

  TTCP: Tetracalcium Phosphate.

  CDHA: Calcium deficient hydroxyapatite.

Introduction

Cement is essential for construction but creates major environmental problems. Its production from limestone, clay, silica, and gypsum generates substantial CO_2 emissions and requires high-temperature manufacturing that contributes to climate change and environmental degradation [1]. While demand for traditional Portland cement remains strong, researchers are increasingly focusing on low-carbon alternatives that don't use Portland clinker and can be manufactured at lower temperatures to reduce environmental impact [2].

Calcium sulfoaluminate cement (CSA), also called "ye'elimite", is a leading green cement alternative that offers significant environmental advantages over traditional Portland cement. Made from gypsum, bauxite, and less limestone, CSA contains the highly reactive ye'elimite phase ($C_4A_3\$$) and can be produced at 1250-1350°C about 200°C lower than Portland cement. This reduced manufacturing temperature improves energy efficiency and substantially cuts CO_2 emissions [3][4]. CSA's high hydraulic reactivity provides rapid setting and exceptional early strength development, making it ideal for time-sensitive projects that demand quick completion [5]. This versatility allows CSA to serve effectively as both a primary binder and additive across diverse construction applications, including rapid concrete repair, pre-cast concrete production, self-leveling compounds, grouting materials, and coastal infrastructure projects [6].

Based on previous studies in this field [7][8], this thesis aims to investigate the possibility of preparing ye'elimite-based multiphase composites using fluorapatite extracted from Djebel Onk deposits in Algeria as a source of calcium oxide. This study addresses a fundamental scientific problem represented by replacing traditional raw materials (limestone) with fluorapatite in the ye'elimite synthesis process, which requires conducting an in-depth analysis of the chemical reactions and phase transformations accompanying this substitution.

This thesis seeks to conduct a comprehensive and systematic study of the effect of various addition such as natural quartz and MgO on the physical and chemical properties of fluorapatite, with the aim of improving the efficiency of forming ye'elimite-based multiphase composites. Through this experimental approach, the study aims to provide a valuable scientific contribution in the field of developing sustainable cementitious materials, which may open new horizons for using local resources in a more efficient and environmentally sustainable manner.

The thesis is structured into three distinct parts: the theoretical section, the experimental component, results, and discussion:

The theoretical segment encompasses a **Chapter I**, which is devoted to general information on cements and CSA cements. It also highlights the different areas of application of these CSA cements. In addition, it describes the different types and characteristics of cements, CSA cements, and natural phosphate. Finally, it emphasizes the importance of natural phosphate in the cement field.

Chapter II focuses on the significance of the raw materials used in the study, providing a detailed description of the key stages involved in powder preparation, mixture formulation, sample preparation at varying concentrations, and sintering at different temperatures. Furthermore, the main experimental equipment and techniques used for preparation and characterization throughout the study are thoroughly described.

Chapter III is divided into two parts:

- ✓ In the first part of the thesis, multiphase composites based on ye'elimite and fluorapatite were synthesized. The inherent CaO in fluorapatite improved the sintering densification. The study examined the effect of varying SiO_2 content (0–5.4 wt.%) on the reactive sintering of fluorapatite, bauxite, and gypsum. Adding quartz promoted the formation of phases like calcium hexaluminate, fluorapatite, ye'elimite, and gehlenite. Rietveld quantitative analysis (using Profex software) demonstrated a relationship between quartz content and the preferential formation of gehlenite over ye'elimite within the 1300-1350 °C range. Furthermore, quartz addition significantly altered the composite's microstructure, producing hexagonal and circular grains after sintering at 1400 °C.
- ✓ The second part of this thesis focused on studying the impact of MgO on the decomposition of natural fluorapatite during the synthesis of spinel-ye'elimite-based multiphase composites. Through advanced characterization techniques (XRD, Rietveld refinement, SEM-EDS, FTIR, and TG/DTG), we explored how varying temperatures (1000-1500 °C) and MgO contents (0-6 wt%) affected phase formation, including fluorapatite, ye'elimite, spinel, hibonite, beta-tricalcium phosphate, and grossite. The findings indicate that increasing MgO content enhances spinel formation and helps stabilize ye'elimite at higher temperatures.

Finally, the most important findings of the study are summarized in the **Conclusion**.

CHAPTER I

Bibliographic overview

Part I. Overview of Cement

I.1. History of cement

The history of cement dates back thousands of years, and its development can be traced through various civilizations. Here is an overview of the historical progression of cement [9]:

- ✓ Ancient civilizations

Both ancient Egyptian and Roman civilizations used various types of cementitious materials. The Egyptians used a form of lime-based cement to build the pyramids, while the Romans developed a more advanced hydraulic cement, which could be set underwater. This Roman cement was made by mixing volcanic ash with lime.

- ✓ Middle ages

Medieval Europe saw a decline in cement production knowledge while lime mortar remained in use for construction during this period.

- ✓ Renaissance and early modern period

During the Renaissance, interest in classical knowledge, including Roman cement production techniques, was revived which led to the return of hydraulic lime usage in construction.

- ✓ 18th and 19th centuries

The modern era of cement began in the 18th century with the development of Portland cement as in 1824 Joseph Aspdin, a British bricklayer, patented a process for producing cement by burning a mixture of limestone and clay which resembled Portland stone and was named Portland cement.

- ✓ Late 19th and early 20th centuries

With the advent of the Industrial Revolution, cement production expanded and became more efficient as demand grew significantly, making it a crucial material for construction projects.

- ✓ 20th century

The 20th century witnessed continuous advancements in cement technology, resulting in the development of various types with specific properties while the standardization of cement and the implementation of quality control measures improved the industry's reliability.

- ✓ Late 20th century to present

In recent decades, awareness of the environmental impact of cement production especially carbon dioxide emissions have grown. Research and development efforts have been directed towards more sustainable cement production processes [10].

- ✓ Current Trends

The cement industry continues to evolve with a focus on innovation and sustainability. Efforts are concentrated on reducing carbon emissions, utilizing alternative raw materials, and developing new types of environmentally friendly cement with enhanced performance [11].

I.2. Definition of hydraulic cement

Cement is a finely ground powder made by blending and grinding a mixture of minerals, primarily limestone and clay. When mixed with water, it undergoes a chemical reaction known as hydration, hardening over time to form a strong, durable solid material [12].

I.3. Type of hydraulic cement

There are several types of cement, each designed to meet specific construction needs and performance requirements. The most common types include:

- ✓ Portland cement (Type I, Type II, Type III, Type IV, Type V)

Type I: General-purpose Portland cement is suitable for most construction applications.

Type II: Portland cement with moderate sulfate resistance, suitable for environments with sulfate exposure.

Type III: High-early-strength Portland cement, which gains strength more quickly than Type I, making it suitable for fast-track construction projects.

Type IV: Low-heat Portland cement designed for massive concrete structures, reducing the risk of thermal cracking.

Type V: Portland cement with high sulfate resistance, used in environments with high sulfate concentrations, such as marine structures [13][14].

- ✓ Hydraulic lime

A type of lime-based cement that sets through hydration and is used in the restoration of historic buildings and specific niche construction applications [15].

- ✓ Expansive cement

Contains expansive agents that increase the volume of the cement paste, which is useful in applications where shrinkage cracking needs to be minimized [16].

- ✓ Oil-Well cement

Specifically designed for use in oil and gas well construction, providing the necessary durability and performance in downhole conditions [17].

- ✓ Rapid hardening cement

Similar to Type III Portland cement, this type gains strength quickly and is suitable for projects where fast setting and early strength development are crucial [18].

- ✓ Low heat cement

Formulated to produce less heat during hydration, reducing the risk of thermal cracking, and is suitable for massive concrete structures [19].

- ✓ High alumina cement

Contains high levels of alumina and is used in applications requiring rapid hardening and high resistance to chemical attacks [20].

I.4. The fabrication of hydraulic cement

The fabrication of cement involves a multi-step process, starting from the extraction of raw materials to the final product. Here is an overview of the typical steps involved in the cement fabrication [13-15]:

- ✓ Mining and extraction of raw materials

Limestone, clay, shale, and silica are the primary raw materials used in cement production. These materials are typically mined from quarries or extracted from natural deposits.

- ✓ Crushing and pre-blending

The extracted raw materials are crushed into smaller pieces to facilitate the subsequent stages of the manufacturing process. The crushed materials are then pre-blended to ensure a homogeneous mix.

- ✓ Raw Meal Preparation

The pre-blended raw materials are further processed to create a raw meal. This involves grinding the materials into a fine powder, which is then homogenized to achieve a consistent composition.

- ✓ Clinker formation in the CaO-Al_2O_3-SiO_2 system

The CaO-Al_2O_3-SiO_2 ternary phase diagram serves as the fundamental framework for understanding Portland cement clinker formation by mapping the relationships between the three primary oxide components that constitute 85-90% of cement composition. At the typical clinkering temperature of 1400-1450 °C, partial melting creates a liquid phase that facilitates the formation of key hydraulically active minerals including alite (C_3S), belite (C_2S), and aluminate phases (C_3A), with the pure three-oxide system requiring slightly higher temperatures due to the absence of industrial flux components like alkalis and iron oxide that lower melting points. During the heating process, the system approaches thermodynamic equilibrium through limestone decomposition and intermediate compound formation, while subsequent cooling involves crystallization of clinker minerals from the melt and critical solid-state transformations such as the $\alpha \rightarrow \beta$ conversion of C_2S. This phase diagram enables cement manufacturers to optimize raw material proportions, control burning conditions to maximize beneficial C_3S formation, predict raw meal behavior during processing, and design cooling regimes that produce the most reactive clinker minerals, providing the theoretical foundation for industrial cement production despite the need to account for additional minor components in practical applications [22].

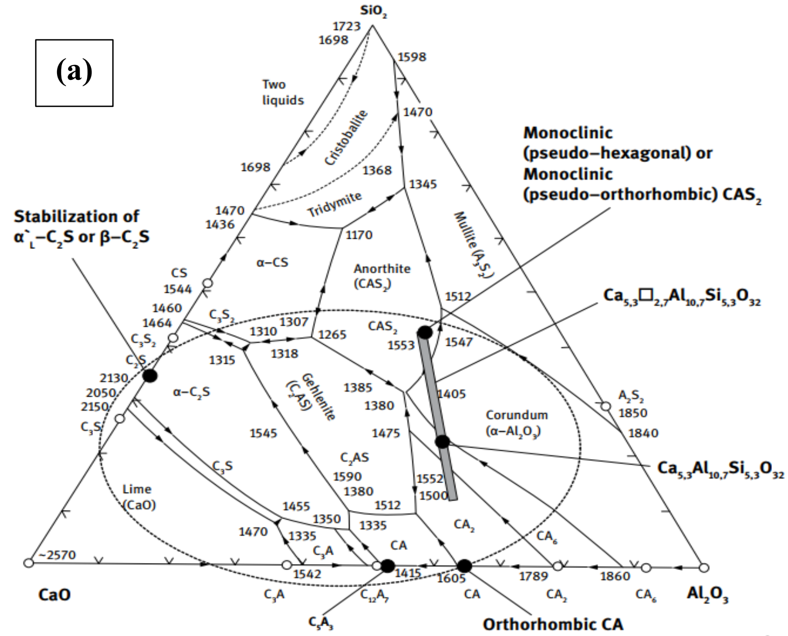

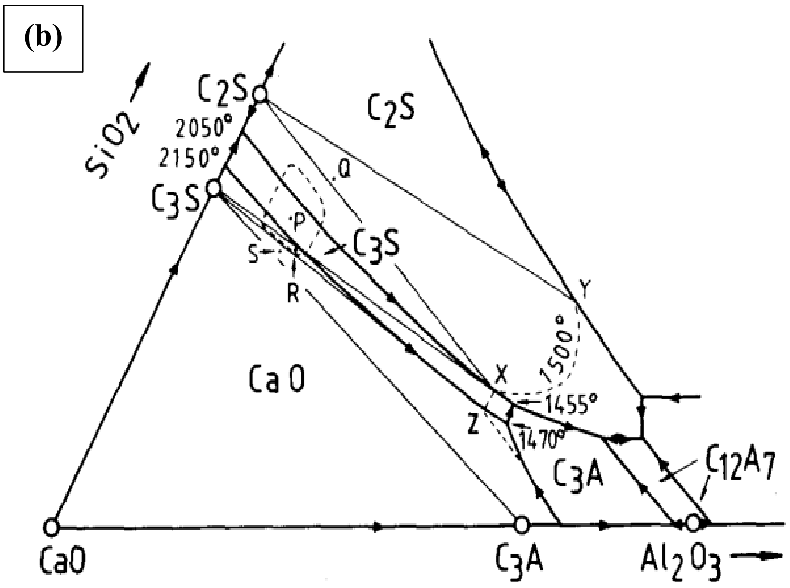

Fig.I.1. (a) Description of the $CaO-Al_2O_3-SiO_2$ system; (b) a portion of the $CaO-Al_2O_3-SiO_2$ system illustrating the formation of Portland cement clinker [22].

- ✓ Grinding of Clinker

The clinker is then finely ground with gypsum to produce cement powder. Gypsum is added to control the cement setting time.

- ✓ Storage and Packaging

The final cement product is stored in silos until it is ready for packaging. The cement is then packaged in bags or bulk for distribution to construction sites.

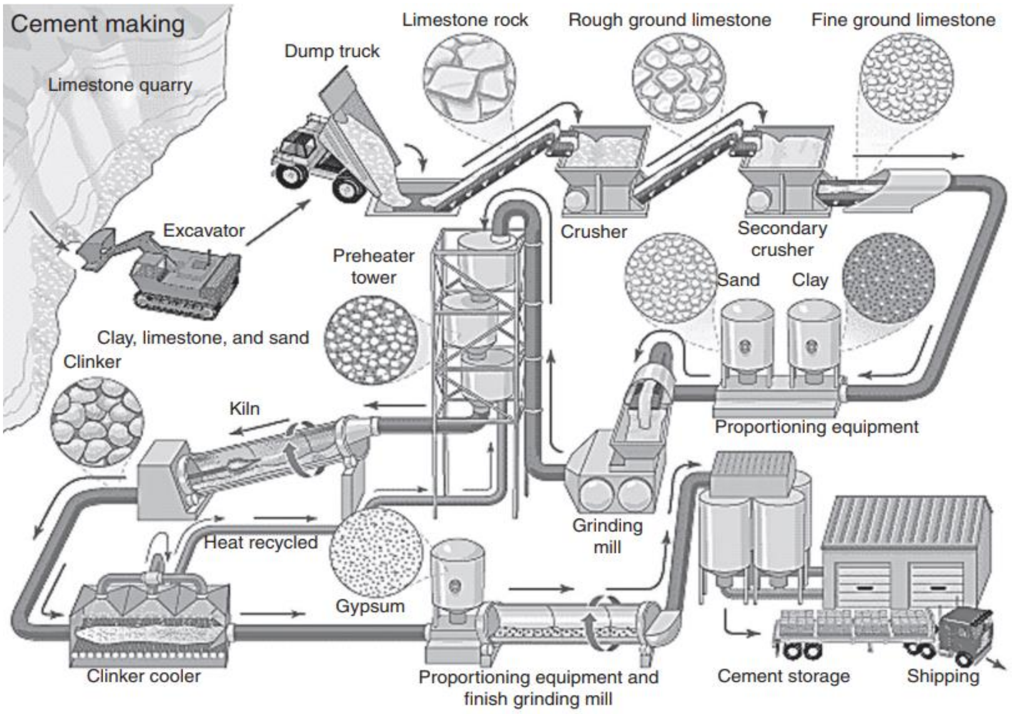

Fig.I.2. Cement production processes [12].

I.5. The hydration of hydraulic cement

The hydration of cement is a complex chemical process that occurs when cement particles are mixed with water. This process leads to the formation of various hydration products, contributing to the hardening and setting of the cementitious material. The primary compounds involved in the hydration of cement are tricalcium silicate (C_3S), dicalcium silicate (C_2S), tricalcium aluminate (C_3A), and tetracalcium aluminoferrite (C_4AF). Here is an overview of the key stages and reactions in the hydration process [13-14]:

- ✓ Initial contact with water

When water is added to cement, it initiates a series of chemical reactions. The water reacts with the various compounds in the cement, especially the calcium silicates, to form new compounds.

- ✓ Formation of Calcium Silicate Hydrates (C-S-H)

The primary reaction during cement hydration is the formation of calcium silicate hydrate gel (C-S-H). This gel is responsible for the strength and binding properties of concrete.

- ✓ Formation of Calcium Hydroxide (CH)

Simultaneously, calcium hydroxide (CH) is produced as a byproduct. This compound also contributes to the strength of the concrete, but to a lesser extent.

- ✓ Development of Ettringite and Monosulfate

Another reaction involves the formation of ettringite (AFt) and monosulfate (AFm) from tricalcium aluminate (C_3A). These compounds contribute to the early strength of concrete.

- ✓ Setting and Hardening

The hydration process leads to the setting and hardening of the concrete. Setting refers to the transition from a plastic, workable state to a solid state, while hardening involves the progressive development of strength over time.

- ✓ Continued Hydration over Time

Fig.I.3 illustrates the cement hydration process, showing how separate cement grains (shaded areas) transform into a hardened paste structure through distinct phases. Initially, during the dormant period, cement grains remain separate while producing mainly calcium hydroxide (hexagonal shapes) and ettringite (heavy short lines). After one hour, calcium silicate hydrate

(CSH) gel begins forming as long fibers (thin short lines), causing the paste to stiffen through intergrowth while reducing porosity as solid volume increases. By 24 hours, sulfate depletion triggers the formation of alumina and iron oxide phases, ettringite converts to monosulphate, and calcium silicates continue hydrating to produce shorter CSH fibers. Throughout this progressive process, hydration products continuously fill pores, steadily decreasing the paste's porosity and creating the final hardened cement structure through the intergrowth and volume expansion of these various hydration products [21].

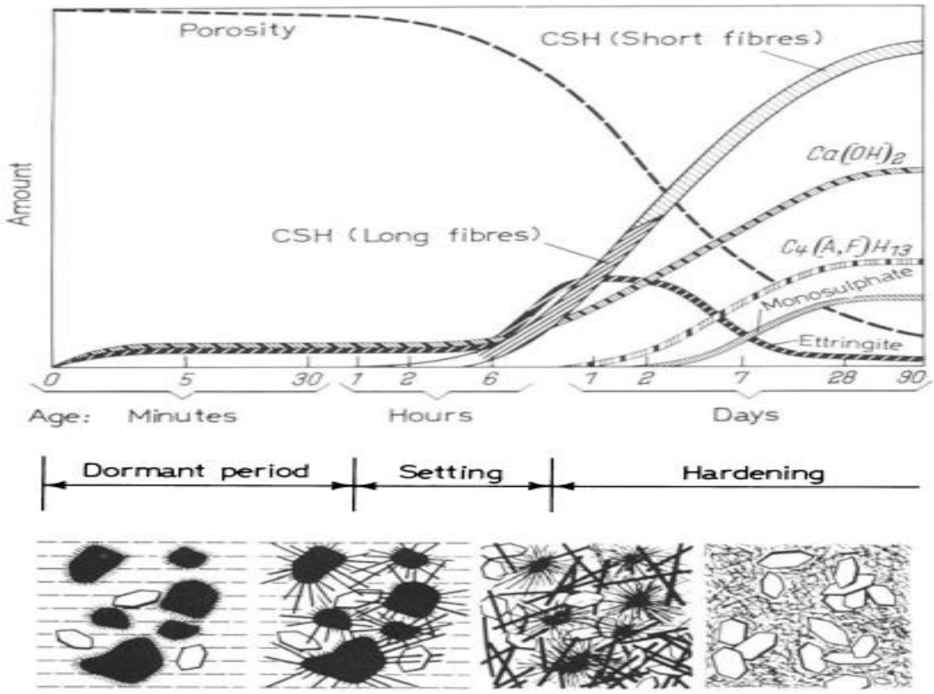

Fig.I.3. Schematic description of the hydration process and structure formation in cement paste [21].

I.6. Characterization of hydraulic cement

Characterization of cement involves assessing its physical, chemical, and mechanical properties. This process is crucial for ensuring the quality and performance of cement in various construction applications. Here are some key aspects of the characterization of cement [1, 16].

- ✓ Chemical composition

The chemical composition of cement is critical, particularly the amounts of key compounds such us: C_3S (tricalcium silicate), C_2S (dicalcium silicate), C_3A (tricalcium aluminate), and C_4AF (tetracalcium aluminoferrite) and free CaO, is critical. X-ray fluorescence (XRF) and other analytical techniques are often used to determine these compounds accurately.

- ✓ Physical properties

Fineness: The fineness of cement particles influences the rate of hydration and, consequently, the strength development. The Blaine's specific surface area test is commonly used for this assessment.

Setting Time: Initial and final setting times are measured using standardized methods to ensure suitability for construction processes.

Soundness: The soundness of cement refers to its ability to retain volume after setting. Tests such as the Le Chatelier apparatus or autoclave expansion tests assess this property.

- ✓ Mechanical properties

Compressive Strength: This is a crucial property that indicates the ability of cement to withstand loads. Compressive strength tests are conducted at various curing ages to assess the strength development over time.

Tensile Strength: Although cement has low tensile strength, its combination with reinforcement materials addresses structural tensile requirements.

Flexural Strength: This property is important for materials subjected to bending stresses. Flexural strength tests assess the ability of cement to withstand such stresses.

- ✓ Heat of hydration

The heat generated during the hydration process is measured using calorimetry to predict potential thermal cracking and optimize concrete mix designs.

- ✓ Durability

Resistance to Sulfates: The ability of cement to resist sulfate attack is essential, especially in environments where exposure to sulfates is a concern. Sulfate resistance tests are conducted to evaluate this property.

Resistance to Chloride Ion Penetration: The penetration of chloride ions can lead to the corrosion of reinforcing steel. Tests like the Rapid Chloride Permeability test assess the resistance of cement to chloride ion penetration.

- ✓ Microstructure Analysis

Techniques such as scanning electron microscopy (SEM) and X-ray diffraction (XRD) are used to analyze the microstructure of cement, providing insights into the hydration products and overall composition.

Part II. Calcium Sulfoaluminate

II.1. History of calcium sulfoaluminate

Calcium sulfoaluminate (CSA) cements primarily consist of ye'elimite ($C_4A_3\$$) as the major cementing phase, ranging from 30 to 70%. Alexander Klein patented ye'elimite, also referred to as "Klein's compound, in 1960, recognizing it's expansive or shrinkage compensating properties when added to cementitious binders. In China, CSA cements, recognized as the "third cement series," have been produced, utilized, and standardized for approximately three decades. In recent years, various European cement producers have initiated research and development endeavors in this domain and have successfully entered the market [17,18].

Throughout its history, the development of CSA cement has been marked by collaboration among researchers, contributions from various countries, and a growing awareness of the potential benefits of this alternative cementitious material [19,20].

II.2. What is Ye'elimite?

Ye'elimite is a mineral with the chemical formula ($4CaO{\cdot}3Al_2O_3{\cdot}SO_3$ or $C_4A_3\$$ in cement notation). It belongs to the class of minerals known as calcium sulfoaluminate. It is a key component in the formation of certain types of hydraulic cements, particularly calcium sulfoaluminate cements [25].

Ye'elimite is the primary calcium sulfoaluminate phase responsible for the unique properties of CSA cement, such as rapid setting and high early strength. It forms during the linearization process of CSA cement, where raw materials containing calcium, aluminum, and sulfur are heated at high temperatures. Its distinct crystal structure characterizes ye'elimite and plays a crucial role in the overall performance of CSA cement in construction applications [26].

II.3. Types of ye'elimite

Ye'elimite-based cement exhibits a broad spectrum of phase compositions that require clarification. To improve clarity and standardize the criteria for of these cements, the terminology has been standardized based on the predominant crystalline phase content [17,18,23]. The following is a proposed scheme for standardization of terminology:

Table I. 1: Suggested acronyms for ye'elimite-based cements [27].

Cement types		Major phase	Secondary phases	other phase(s)
CSA	Calcium sulfoaluminate cement	$C_4A_3\overline{S}$ (68.5%)	C_2S (15.9%)	$C\overline{S}$ -$C_{12}A_7$-CT-
BCSAF	Iron-rich belite calcium sulfoaluminate cement	C_2S (49.07%)	C_4AF (19.16%)- $C_4A_3\overline{S}$ (10.15%)	$C\overline{S}$ -C
BCSAA	Aluminum-rich calcium sulfoaluminate cement	C_2S (56.2%)	$C_4A_3\overline{S}$ (34.4%)	C_3A
ACSA	Alite calcium sulfoaluminate cement	C_3S (48.3%)	C_4AF (12.9%)	$C_4A_3\overline{S}$ $C\overline{S}$ C_2AS $C_5S_2\overline{S}$
BCSA	belite calcium sulfoaluminate cement	C_2S (50%)	$C_4A_3\overline{S}$ (30%)	$C\overline{S}$ -C

II.4. Mineralogical composition of ye'elimite

A thorough understanding of ye'elimite formation via thermal treatment could play a crucial role in addressing the burnability issues encountered during the production of CSA clinkers. The composition of CSA clinkers typically comprises multiple cementitious phases , as detailed in Table (I. 2) [28]. To identify the mineralogical phases within cement clinkers, modified Bogue equations tailored for the CaO-Al_2O_3-SiO_2-Fe_2O_3-SO_3 system are employed, as illustrated in Fig.I.4 [29]. These equations are used to calculate the proportions of cement phases [30].

$\%C_4AF= 3.043\ (\%Fe_2O_3)$

$\%C_4A_3\$= 1.995\ (\%Al_2O_3) – 1.273\ (\%Fe_2O_3)$

$\%C_2S =2.867(\%SiO_2)$

$\%C\$= 1.700\ (\%SO_3) – 0.445\ (\%Al_2O_3) + 0.284\ (\%Fe_2O_3)$

$\%C= 1.000(\%CaO) – 1.867\ (\%SiO_2) – 1.054\ (\%Fe_2O_3) – 0.550\ (\%Al_2O_3) – 0.700\ (\%SO_3)$

Table I. 2: Several compositions of CSA clinkers have been documented in the literature.

Composition Wt.%						**Reference**
$C_4A_3\$$	**CA**	**CA_2**	**$C_{12}A_7$**	**CA_3**	**Another phases**	
68.1	3.2	0.7	1.4	-	26.6	[31]
68.1	7.8	1.2	-	3.4	19.5	[32]
57	15	-	1	-	27	[32]
52.1	-	-	1.2	9.4	37.3	[3]
50	8	-	-	-	42	[33]
50	-	-	-	< 8	42	[34]

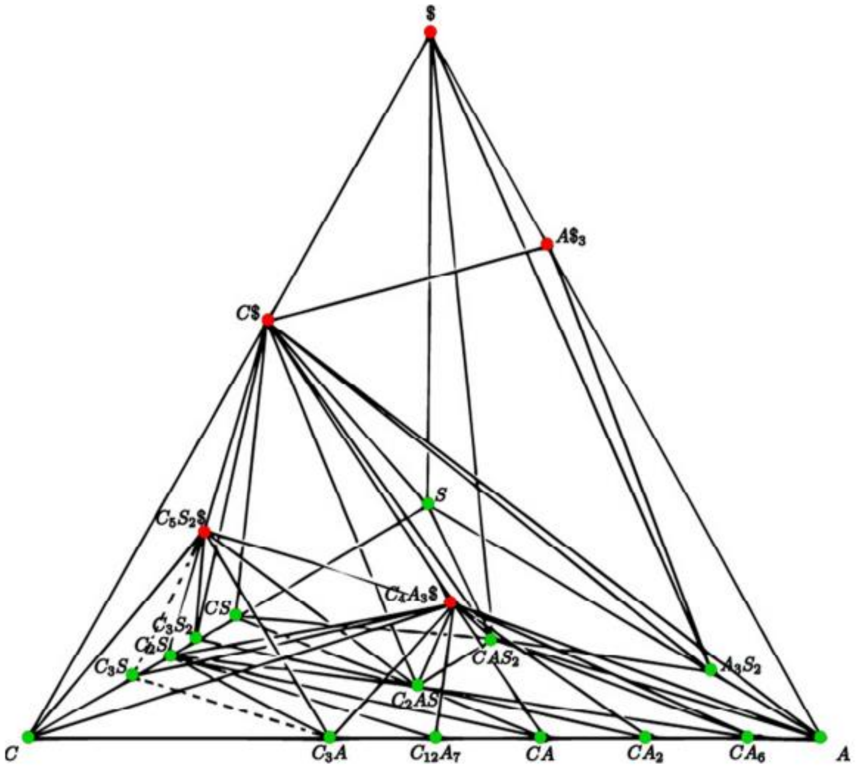

Fig.I.4. tetrahedral diagram of the phase compatibility in the quaternary $CaO-Al_2O_3-SiO_2-SO_3$ system [29].

Comparison between the mineralogical composition of CSA and Portland clinker. It is highly variable and differs from it in several aspects Table (I. 3) [35]:

- The presence of $C_4A_3\$$.
- A very high dosage of calcium sulfate (gypsum or anhydrite).
- The total absence of C_3S and the very low content of C_3A.
- A fairly high calcium ferro-aluminate content in certain cements.

Table I.3: Mineralogical composition of a Portland cement and a CSA cement, in percentage by weight.

	C	**C_3S**	**C_2S**	**C_2AS**	**$C_{12}A_7$**	**C_3A**	**CA**	**C_4AF**	**$C_4A_3\$$**	**$C\$$**
CSA cement	0-25	/	5-62	0-16	0-10	0-1	0-10	0-40	5-70	0-25
Portland cement	/	50-70	15-30	/	/	5-15	/	5-15	/	1-5

II.5. Crystallographic structure of $Ca_4[Al_6O_{12}]SO_4$

Understanding the crystallographic structure of ye'elimite is essential for various applications, particularly in cement chemistry, where ye'elimite plays a significant role in certain cement formulations. Techniques such as X-ray diffraction are commonly used to study and analyze the crystallography of ye'elimite and similar compounds, providing insights into their physical and chemical characteristics.

The crystal structure of ye'elimite, $Ca_4[Al_6O_{12}]SO_4$, belongs to the sodalite mineral family, which encompasses compounds with the general composition $M_4\ [T_6O_{12}]\ X$. These compounds have been recognized for an extended period, existing both as in natural minerals and as artificially synthesized substances. In this context, T occupies tetrahedral sites, typically represented by elements such as Si or Al. M denotes a low-charge cation, including ions like Na^+, K^+, Ca^{2+}, Sr^{2+}, and others. X serves as a charge-balancing anion, with examples including Cl^-, SO_4^{2-}, WO_4^{2-}, and CrO_4^{2-} [36].

The crystallographic structure of ye'elimite is complex and challenging to determine precisely. As a result, no single-crystal structure of ye'elimite has been resolved to date [37]. Previous literature has suggested that ye'elimite can exhibit cubic, tetragonal, and orthorhombic structures based on powder X-ray diffraction data. However, recent observations indicate that only cubic ($I\bar{4}3m$) and orthorhombic ($Pcc2$) structures are present. These two crystallographic polymorphs display distinct physical and chemical properties, including differences in their reactivity with water. Theoretical calculations using density functional theory (DFT) suggest that the orthorhombic structure of ye'elimite is energetically more stable than the cubic structure, as shown in Table I. 4 [38].

Table I. 4: DFT calculations for different ye'elimite phases [38].

Space group	Lattice axis/angle	Length, angle (Å)	Angle (°)				
			α, β, γ	V (Å^3)	ρ (g/cm^3)	K (GPa)	ΔE (eV)
I$\underline{4}$3m	A	9.385	90	826.55	2.45	109.4	1.65
Cm	A	9.445	90	845.60	2.40	114.9	0.41
	B	13.333					
	C	8.246					
Pcc2		13.397	90	1692.68	2.39	105.7	0.00
	B	13.445					
	C	9.398					
I$\underline{4}$	A	9.505	90	859.77	2.36	107.8	0.33
	C	9.516					

[a] Structural data for the lattice, bulk moduli, and relative energy stabilities (ΔE) normalized per single unit cell $Ca_8[Al_{12}O_{24}]$ $(SO_4)_2$ are also shown.

The orthorhombic structure of ye'elimite demonstrates higher energy stability compared to the cubic structure. Consequently, the cubic structure is not stable at ambient temperatures and only appears at elevated temperatures. The transition from the orthorhombic (Pcc2) to the cubic (I$\underline{4}$3m) structure is reversible, occurring at approximately 470°C, with a thermal hysteresis of 10-30 °C. Two variations of $Ca_4[Al_6O_{12}]SO_4$ share a similar crystal structure, as shown in Fig.I.5. The structure consists of irregular six-membered and four-membered rings, formed by AlO_4 tetrahedra, which interconnect by sharing their vertices within the framework. Calcium (Ca)and sulfur (S) atoms are positioned within these four-membered or six-membered rings, forming the corresponding CaO_n polyhedra and SO_4 tetrahedra [36,37].

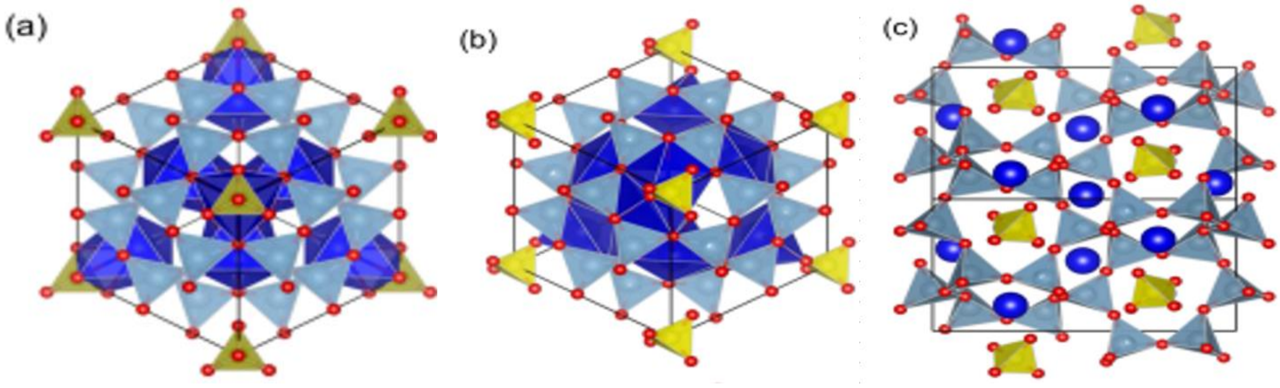

Fig.I.5. Calculated crystal structures of ye'elimite phases: (a) cubic I$\underline{4}$3m, (b) tetragonal I$\underline{4}$, and (c) orthorhombic Pcc2. Ca denoted within dark-blue prisms, Al within light-blue tetrahedra, S within yellow tetrahedra, and O are red [38].

II.6. Manufacturing and environmental impact

II.6.1. Manufacturing CSA cement through the clinkerization process

The clinkerization process of calcium sulfoaluminate (CSA) cement is a crucial step in its production. This process, which has been used for several decades, relies on solid-state reaction among the oxides of the initial materials. Due to its solid-state nature, clinkerization requires substantial energy to facilitate the diffusion of atoms and molecules within the crystals.

During clinkerization, CSA clinker (a calcined material) is formed by heating a mixture of raw materials to a high temperature. The typical raw materials used in CSA clinker production include [17,18]:

- ✓ Limestone ($CaCO_3$): Provides the necessary calcium oxide (CaO) component.
- ✓ Bauxite or Alumina-Rich Materials: Supply aluminum oxide (Al_2O_3), contributing to the formation of sulfoaluminate phases.
- ✓ Gypsum ($CaSO_4{\cdot}2H_2O$): Acts as a source of sulfur trioxide (SO_3), aiding in the formation of sulfoaluminate phases.
- ✓ Silica (SiO_2): Typically found in raw materials such as clay or other aluminosilicates, it contributes to the formation of belite (C_2S).

The clinkerization process typically involves the following steps:

- ✓ Raw Material Preparation: The raw materials are carefully proportioned and ground into fine powder to ensure a homogenous mixture.
- ✓ Mixing and Blending: The finely ground raw materials are mixed thoroughly mixed to achieve a consistent composition.
- ✓ Clinkerization Kiln: The prepared mixture is fed into a rotary kiln, where it undergoes high-temperature treatment (typically around 1250-1350 °C). This process is known as clinkerization, and it involves calcining the raw materials to form clinker nodules [40][41].
- ✓ Cooling: The clinker is then rapidly cooled to ambient temperature to prevent the formation of undesired phases.
- ✓ Grinding: The cooled clinker is ground into a fine powder to produce CSA cement.

The main reactions during the clinkerization process involve the formation of sulfoaluminate and belite phases. For example, ye'elimite is a key phase in CSA clinker and is formed through the following reaction [42][43]:

$$3CaO \cdot Al_2O_3 + CaSO_4 \rightarrow Ca_4Al_6O_{16}S \qquad (I.\ 1)$$

$$2CaO + SiO_2 \rightarrow Ca_2SiO_4 \qquad (I.\ 2)$$

This reaction involves the combination of calcium oxide, aluminum oxide, and sulfur trioxide to form ye'elimite. It is important to note that the clinkerization process for CSA cement differs from the more common Portland cement clinkerization process. The resulting CSA cement exhibits unique properties, including rapid setting and high early strength [41].

II.6.2. Energy consumption and CO_2 emissions in the production of CSA cement

The manufacturing of one tonne of Portland cement results in the release of approximately 851 kg of CO_2 and requires an energy input of about 4.5 GJ. The clinkering process alone accounts for roughly 60% of the total energy expended in cement production. The production of a Portland cement clinker theoretically requires 1,674 to 1,799 GJ/t depending on the composition of the raw material. However, in practical applications, the actual energy input is higher, typically ranging from 3.1 to 3.9 GJ/t, contingent on the energy source employed (such as fuel oil, electricity, hydraulic energy, etc.). Variations in these values arise due to energy losses during degassing, clinker cooling, and heat dissipation through convection and thermal radiation at the kiln level. Carbon dioxide emissions are distributed between two primary sources: approximately 60% results from the decarbonation of raw materials, while around 40% originates from the combustion of fossil fuels during the production phase [19,23,26,46].

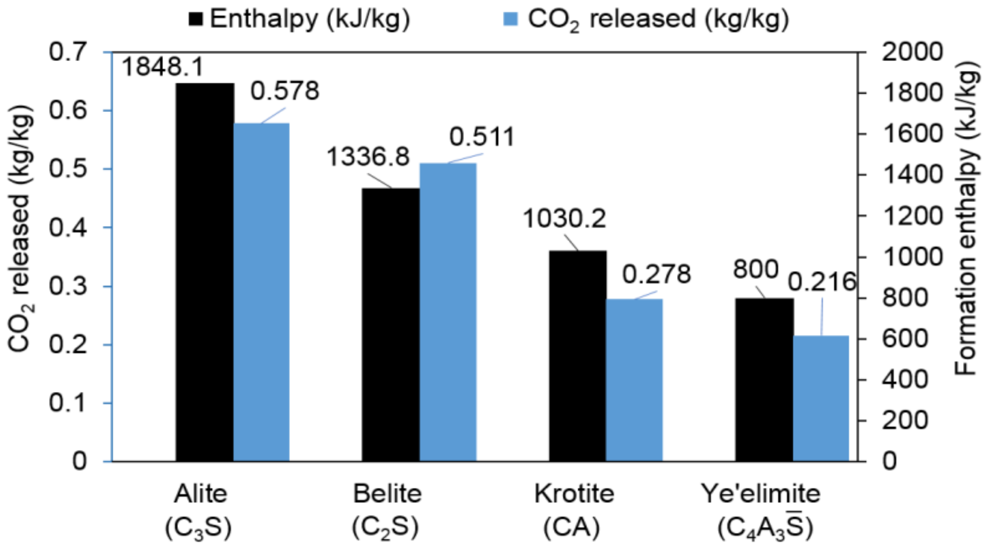

Fig.I.7. CO_2 released and energy requirements during cement phase formation [44].

The manufacture of CSA clinkers requires lower energy input and emits less CO_2 than Portland cement production. Furthermore, the quantity of limestone required is significantly reduced. Limestone calcination, a major source of CO_2 emissions in the clinkering process, is minimized. Fig.I.7 illustrates the energy demands and corresponding CO_2 emissions during this process [44].

CSA cement offer environmental advantages, but their production and availability are limited by the high cost and scarcity of alumina sources like bauxite. This challenge can be mitigated by using industrial by-products such as bauxite waste, fly ash, slag, and dam sludge [33]. However, large-scale adoption of CSA cements is unlikely unless CO_2 emission costs increase substantially [19,46] .

II.7. Hydration process of ye'elimite

The hydration process of ye'elimite involves a chemical transformation that leads to the formation of hydrated phases, which solidify over time. This process generally consists of two key stages. The first stage involves the dissolution of ye'elimite, with the dissolution rate influenced by the reactivity of each phase present. For instance, the reactivity sequence of cementitious materials includes: C_2S, CA, C_4AF, and $C_{12}A_7$.

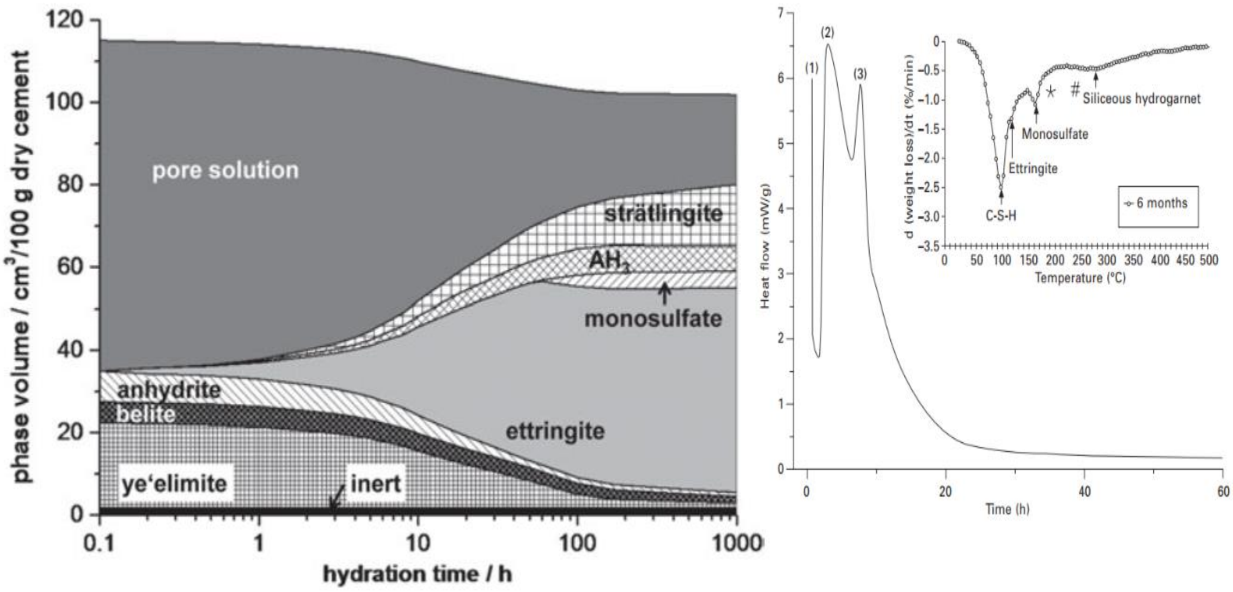

Fig.I.8. Heat flow curve of CSA cement and typical phase volume during the hydration of calcium sulfoaluminate cement with a W/C ratio of 0.8 at 20 °C [17,47].

The second phase involves the formation of hydration products through precipitation. The rate of this process depends on various factors like dissolution rate, hydration temperature, and the presence of accelerators or retarders. The quantity of precipitation is determined by water content and the presence of additives, such as calcium sulfate, as shown in Fig.I.8. The physical and mechanical properties of the solidified materials rely on the characteristics of the precipitates, including their type, fineness, particle shape, specific surface area, particle interactions, and compactness. In the chemical hydration of $C_4A_3\$$, calcium sulfate (C\$) is generally essential for the formation of new compounds, specifically trisulfoaluminate hydrate (ettringite) [17,18,47].

The formation of ettringite ($C_6AS_3H_{32}$), alternatively known as AFt, occurs through the reaction of $C_4A_3\$$ with soluble calcium sulfate and water, as dictated by the chemical reaction (I. 3). This reaction can also occur with anhydrite or bassanite, albeit at various rates. The continued formation of ettringite depends on the availability of calcium sulfates, as indicated by signal (2) in Fig.I.8. If there is an insufficient amount of sulfates to react with the ye'elimite phase, reaction (I. 4) will commence [27]:

$$C_4A_3\$ + 2C\$H_2 + 34H \rightarrow C_6\$_3H_{32} + 2AH_3 \qquad \text{(I. 3)}$$

$$C_4A_3\$ + (16 + x)\ H \rightarrow C_4A\$H_{(10+x)} + 2AH_3 \qquad x = 0,2,4 \qquad \text{(I. 4)}$$

Reaction (8) represents the hydration process of ye'elimite, leading to the formation of an AFm type phase with varying water contents. The final product depends on several factors, such as the hydration time, the water-to-cement (W/C) ratio, and the initial cement phase composition. This reaction is exothermic and initiates once calcium sulfates are depleted, as indicated by signal (3) in Fig.I.8. Both reactions can occur during the early stages of CSA cements hydration [27].

II.8. Applications of ye'elimite

This type of cement has properties that make it suitable for specific applications. Here are some common applications of ye'elimite cement:

- ✓ Sulfate Resistance

The composition of ye'elimite cement makes it resistant to sulfate attack. It is suitable for environments where sulfate resistance is crucial, such as in the construction of sewer pipes and other structures exposed to sulfate-rich soil or water [27].

- ✓ High-early strength concrete

Ye'elimite cement enables the production of high-early strength concrete by rapidly forming ettringite during hydration, allowing the concrete to achieve substantial strength within

6 to 24 hours. It is particularly suitable for fast-track construction projects where minimizing setting and curing times is essential [45]. Concrete made with this cement can reach a strength of approximately 40 MPa just 6 hours after preparation and exceed 55 MPa after 24 hours [6].

- ✓ Rapid setting and pre-cast concrete

Ye'elimite cement is widely utilized in both concrete repair and specialized pre-cast concrete applications due to its rapid setting and early strength development. The key mechanism behind this behavior is the rapid formation of ettringite during hydration, which enables the concrete to achieve significant mechanical strength within hours. This fast reaction makes ye'elimite cement ideal for repair works that require quick reopening to traffic or service, as well as for pre-cast concrete products where early demolding and high production efficiency are essential [44] [46].

Fig.I.9. Rehabilitation project for the Lokern Road Bridge in California, USA [44].

- ✓ Shrinkage control

Ye'elimite cement can be used in high-performance concrete mixtures to help control shrinkage. This is particularly important in applications where minimal cracking and reduced shrinkage are critical [49,50].

- ✓ Specialized grouts (grouting applications)

Ye'elimite cement-based grouts can be used for various applications, such as filling gaps, anchoring bolts, and other grouting needs [45].

Part III. Calcium Phosphate

III.1. Introduction

Calcium phosphate, a vital mineral compound, plays a significant role in cement by enhancing various properties essential to the construction industry. As a fundamental building material, cement benefits from the unique characteristics of calcium phosphate derivatives, which improve setting time, and overall durability. These contributions make concrete structures more resilient and long-lasting. As the construction industry advances, understanding the role of calcium phosphate in cement production becomes crucial for developing sustainable and environmentally conscious building materials. This introduction explores the key aspects of calcium phosphate and its profound impact on cement, highlighting its essential role in modern construction practices [52,53].

III.2. Calcium phosphates within geological systems

In geological terms, natural calcium phosphates are widely distributed, primarily occurring as apatite deposits-specifically fluorapatite in igneous rocks and phosphorites in sedimentary rocks. Some sedimentary rocks form through the weathering of igneous rocks into smaller particles, while others originate from the precipitation of dissolved igneous minerals or biomineralization processes. Francolite, also known as carbonated hydroxy-fluorapatite, is commonly considered the primary mineral in phosphorites. Natural phosphorites occur in various forms, including nodules, crystals, and masses. Additionally, other natural calcium phosphate minerals, such as clinohydroxylapatite, staffelite, and dicalcium phosphate dihydrate (DCPD), are occasionally found. Global reserves of natural calcium phosphates are estimated to surpass 150 billion tons, with phosphorites accounting for 85% and apatite for the remaining 15% [49].

III.3. Apatite

Apatites form a distinct supergroup of minerals characterized by the general chemical formula $M_5(TO_4)_3X$. The metal cation **(M)** can include Ca^{2+}, Pb^{2+}, Ba^{2+}, Sr^{2+}, Mn^{2+}, Mg^{2+}, Fe^{2+}, Na^{+}, K^{+}, Ce^{3+}, La^{3+}, $Y^{3+}$and Bi^{3+}; the tetrahedral cation **(T)** can include P^{5+}, As^{5+}, V^{5+}, Si^{4+}, S^{6+}, or B^{3+}; while the anion **(X)** can be F, OH, or Cl (see Fig.I.10) [55,56].

Apatites encompass orthophosphates, with calcium phosphate apatites-such as fluorapatite (FA), hydroxyapatite (HA), and calcium-deficient hydroxyapatite (Ca-def HA)-being the most prevalent members. Given the supergroup's vast diversity of over 40 mineral species, it is unsurprising that more than half of Earth’s long-lived isotopes bearing elements can integrate into the apatite structure in various valence states. While substitutions typically occur in trace amounts, ertain dopants (e.g., F^- and OH^-) can lead to significant concentrations and even complete solid solutions. Additionally, crystallographic defects may result in missing ions within the crystal structure, giving rise to nonstoichiometric compounds like Calcium-deficient hydroxyapatite [37,54].

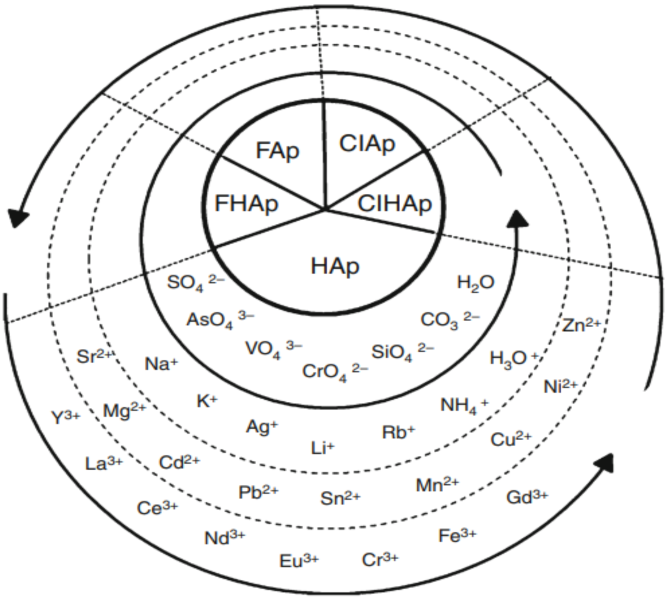

Fig.I.10. The main apatites and the different ions that are able to be incorporated into their crystal lattices [52].

Table I. 5: Calcium phosphate family and its main characteristics [54,57].

Formula	**Compound**	**Ca/P**	**Density (g/cm^3)**	**Solubility at 25 °C, -log (Ks)**	**Solubility at 25 °C (g/L)**	**pH stability range in aqueous solutions at**
$Ca(H_2PO_4)_2. H_2O$	MCPM	0.5	2.23	1.14	18	0.0–2.0
$Ca(HPO_4), 2H_2O$	DCPD	1	2.3	6.59	0.088	2.0–6.0
$Ca(HPO_4)$	DCPA	1	2.93	6.90	0.048	-
$Ca_8(PO_4)_4(HPO_4)_2,5H_2O$	OCP	1.33	2.67	96.6	0.0081	5.5–7.0

α-$Ca_3(PO_4)_2$	α-TCP	1.5	2.86	25.5	0.0025	-
β-$Ca_3(PO_4)_2$	β-TCP	1.5	3.07	28.9	0.0005	-
$Ca_{10}(PO_4)_6(OH)_2$	HAp	1.67	3.16	116.8	0.0003	9.5–12
$Ca_{10}(PO_4)_6F_2$	FAp	1.67	3.16	120	0.0002	7–12
$Ca_{10}(PO_4)_6O$	OAp	1.67	~3.2	~69	0.087	-
$Ca_4(PO_4)_2O$	TTCP	2	3.05	38	0.0007	-
$Ca_{10x}(HPO_4)_x(PO_4)_{6x}(OH)_{2x}$ (0<x <1)	CDHA	1.67	3.16	85	0.0094	6.5–9.5

III.4. Properties of calcium phosphates

The properties of calcium phosphates involve assessing various physicochemical and structural properties of these compounds. This process includes methods such as spectroscopy, X-ray diffraction, electron microscopy, and other analytical techniques. Understanding these properties is essential for both natural and synthetic calcium phosphates and plays a crucial role in fields such as medicine, materials science, and industry [57,58].

III.4.1. Standard spectra and diffractograms of calcium phosphates

X-ray diffraction (XRD) proves to be an essential method in characterizing calcium phosphate materials. XRD analyses can be conducted on single crystals, solid polycrystalline ceramics, coatings, or powders [37,58]. By examining the positions of peaks in XRD patterns, all crystalline calcium phosphate compounds can be identified using diffraction pattern databases such as those provided by the International Centre for Diffraction Data (ICDD), the Joint Committee for Powder Diffraction Standards (JCPDS), and others. In routine applications, specific intense peaks, known as "100% peaks," are utilized for the identification of key Ca/P phases. Table (I. 6) provides a summary of these 100% peaks, their corresponding orientations, inter-planar distances (d_{hkl}), and diffraction angles based on the crystallographic orientation (using the characteristic copper line λk1Cu) [57-59].

Table I. 6: Key data from the XRD spectra of calcium phosphate [53].

Phase	**JCPDS File**	**hkl (100%)**	**d_{hkl}(°A)**	**(2θ, λ_{Cu})**
α-TCP	09-0348	441	2.905	30.753
β-TCP	09-0169	210	2.88	31.027
TTCP	25-1137	040	2.995	29.807

HAP	72-1243	211	2.81	31.820
FAP	15-0876	211	2.80	31,937
DCPA	09-0080	112	2.958	30.189
DCPD	09-0077	020	7.57	11.681
	09-0077	121	4.24	20.935
OCP	26-1056	010	18.7	4.722

III.4.2. Fourier transform infrared spectra of calcium phosphates

Fourier transform infrared (FT-IR) spectroscopy is an effective technique for identifying the majority of calcium phosphate phases. This method primarily utilizes the internal vibrational levels of molecules and ions, which are influenced by their local chemical environments. Phosphate, carbonate, hydroxide, and water molecules can be effectively detected and differentiate through FT-IR spectroscopy. Moreover, it is particularly useful for identifying amorphous calcium phosphate phases, which may not be detectable by XRD. Table (I. 7) summarizes the principal characteristic bands corresponding to various vibrational modes of phosphate groups in infrared spectroscopy [57,58].

Table I. 7: Vibrational modes properties of (PO_4^{3-}) groups in calcium phosphate networks (cm^{-1}) [53].

Phase Vibration mode	**α-TCP**	**β-TCP**	**TTCP**	**HAp**	**FAp**	**DCPA**	**DCPD**	**OCP**	**ATCP**
υ_3 (PO_4^{3-})	1055 1039 1025 1013 997 984	1119 1094 1080 1041 1010	1105 1093 1073 1062 1046 1033 1010	1092 1040	1160 1038	1215 1132 1070 1060 1000	1400 1350 1175 1128 1064	1295 1193 1137 1121 1103 1077 1055 1037	1040

								1023	
								1000	
υ_1 (PO_4^{3-})		972	989			992	984		
			962	962	968			962	
	954		956						
		945	946						949
			941						
υ_4 (PO_4^{3-})	613		620					627	
	597	602	594	601	604			601	
	585	589							
	563		571	575	571	577	576	575	
	551	550		561	566		563	560	560
		541	501			526	525	524	
υ_2 (PO_4^{3-})	471		471	472	471	480			
	463							466	
	454								
	430	432	450			428	418	449	
	415		429			405	400		
			399			398			
OH^-				632					
				3570					

Part IV. Fluorapatite

IV.1. Fluorapatite

Fluorapatite (FAp), chemically represented as $Ca_5(PO_4)_3F$, is conventionally denoted as $Ca_{10}(PO_4)_6F_2$ to signify the presence of two formula units within the crystal unit cell. The presence of fluorides in natural apatites, was first recognized in 1798, marking Fluorapatite one of the earliest known fluoride-containing minerals. Among calcium phosphates, FAp stands out as the hardest (scoring 5 on the Mohs scale of mineral hardness), the most stable, and the least soluble. Furthermore, it is the most thermally stable calcium phosphate, with a high melting point of 1650 °C [54].

Due to these exceptional properties, FAp is the only calcium phosphate that naturally forms substantial deposits suitable for commercial applications. Fluorapatite readily forms solid solutions with Hydroxyapatite, featuring any desired F/OH molar ratio. These compounds are commonly referred to as Fluorhydroxyapatites (FHAp) or or Hydroxyfluorapatite (HFAp) and are represented by the chemical formula $Ca_{10}(PO_4)_6(OH)_{2-x}F_x$, where $0 < x < 2$. When the exact F/OH ratio is unknown or not a critical, their chemical formula is often expressed as $Ca_{10}(PO_4)_6(F, OH)_2$. The lattice parameters, crystal structure, solubility, and other properties of FHAp and HFAp fall between those of the pure Fluorapatite and Hydroxyapatite. Specifically, the substitution of F for OH results in a contraction along the a-axis with minimal changes to the c-axis, accompanied by a more pronounced resolution of the IR absorption spectra [54,57,58].

IV.2. Structure of fluorapatite

Fluorapatite crystallizes in the hexagonal system with space group P63/m and is represented by the formula $Ca_{10}(PO_4)_6F_2$. The structural elucidation of this compound was initially conducted by Naraz [61,62], followed by Beevers [56], and later refined by Young et al [57]. Its structure features as a honeycomb assembly of PO_4 ions (see Fig.I.11). The most prevalent form of this compound in nature is the phosphocalcic $Ca_{10}(PO_4)_6F_2$, with lattice parameters a = 0.9372 nm and c = 0.6885 nm. The structure consists of columns of calcium atoms situated at both the vertices and midpoints of the hexagonal mesh edges [58].

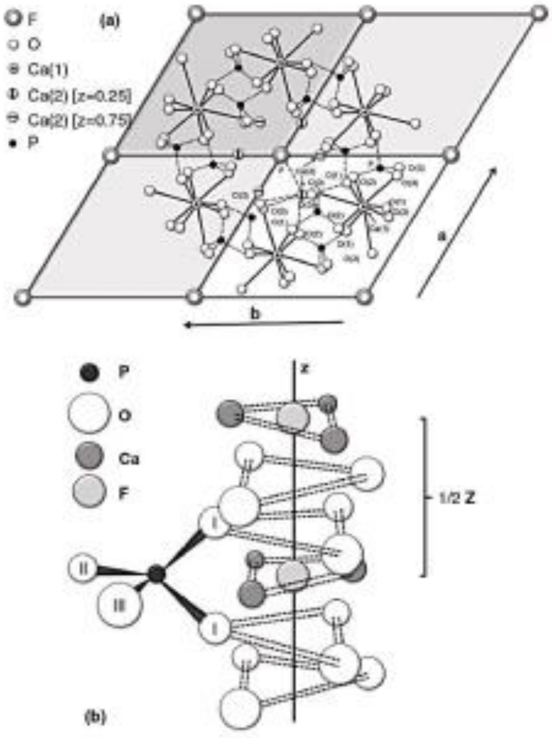

Fig.I.11. Structure of fluorapatite.

The structural framework is primarily composed of anionic groups (PO^{3-}_4) groups, forming a quasi-compact arrangement and revealing two distinct types of tunnels. The initial tunnel, aligned with the ternary axis of the lattice, accommodates Ca^{2+} cations spaced at intervals of c/2 along the oz axis. These Ca^{2+} ions are specifically labeled as Ca (I) (refer to Fig.I.11). The second tunnel, with a larger diameter, follows a helical axis and is occupied by fluoride ions. The surrounding walls contain the remaining Ca^{2+} ions, denoted as Ca (II), which are arranged in equilateral triangles with a mutual offset of 60°. These tunnels play a crucial role in the various substitution reactions observed within this structural family [58,62].

IV.3. Properties of fluorapatite

Fluorapatite consists of 38-50% CaO by mass, 18-28% P_2O_5, and 2-4%F, resulting in a Ca/P atomic ratio of 1.67-2. The diffraction lines specific to pure FAp are illustrated in (PDF codes*15-0876) [66,67].

The FT-IR spectrum of FAp is presented in Fig.I.12, where the prominent infrared bands correspond to the fundamental frequencies of tetrahedral phosphate ions $(PO4)^3$. The apatite structure reduces ion symmetry, resulting in the activation of the previously inactive ν_1 mode (four fundamental frequencies with IR inactive ν_1 mode). The degree of crystallinity in both natural and synthetic apatite samples is commonly assessed based on the broadening of the $\nu_4(PO_4)$ infrared absorption bands [60]. If calcite is present, the infrared spectrum of the analyzed sample exhibits the antisymmetric stretching mode (ν_3) associated with the planar CO_3^{2-} ion. Table (I. 8) provides an overview of its physico-chemical and mechanical properties properties of fluorapatite [65,69].

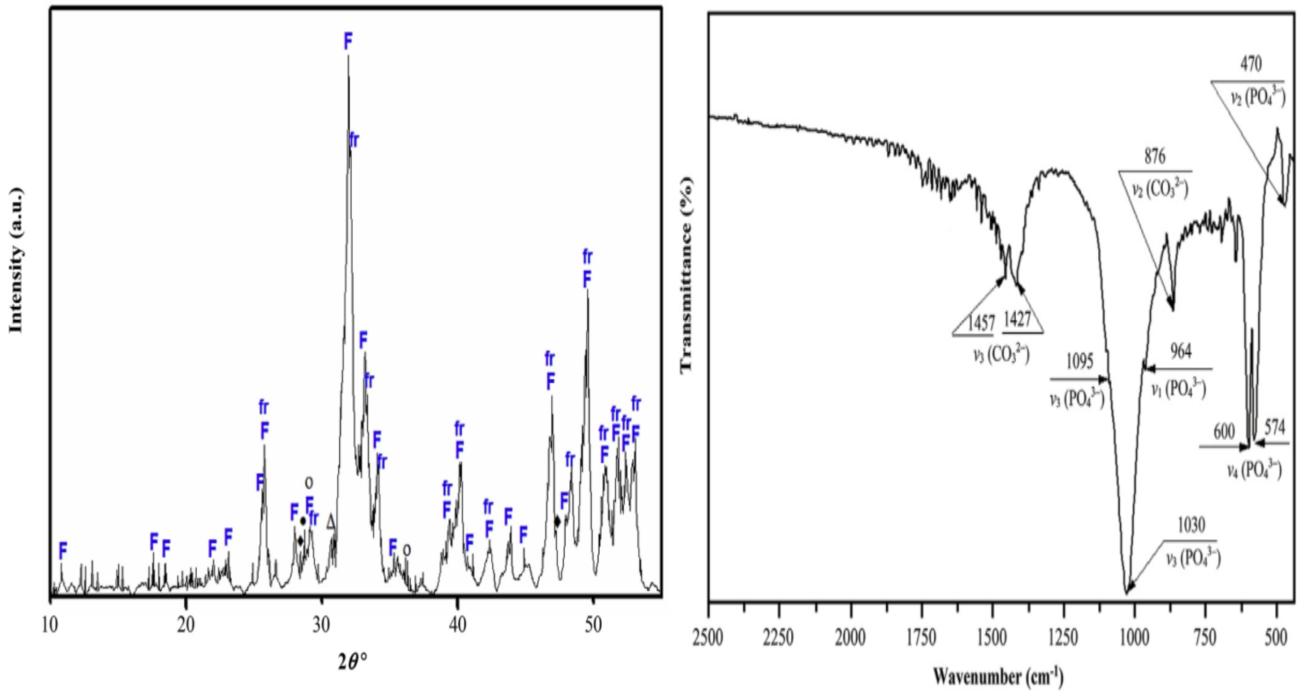

Fig.I.12. FTIR and XRD patterns of natural fluorapatite: the phases were identified as fluorapatite (F), francolite (fr), Ca $(OH)_2$ (●), $CaCO_3$ (○), CaF_2 (♦) and dolomite (Δ) [60].

Table I. 8: Physico-chemical and mechanical properties of fluorapatite [57,65,69].

Chemical formula	$Ca_{10}(PO_4)_6F_2$	**Melting point**	1640 °C
Structure	Hexagonale, $P6_3/m$	**Dielectric constant**	9,5-10,4 pFm^{-1}

Density	3,19	**Thermal conductivity**	0,02W/Cm.K
Solubility product	pks=60	**Zeta potential**	6,5-8,8
Enthalpy of formation	-35,59kJ/mol	**Young's module**	94 GPa

IV.4. Experimental methods for the decomposition of fluorapatite

Fluorapatite is a mineral belonging to the apatite group, composed of calcium phosphate with fluoride ions. The breakdown or decomposition of fluorapatite can be achieved through chemical, physical or mechanical methods. Here are some experimental methods for the decomposition of fluorapatite:

- ✓ Acid dissolution

Apatite minerals, including fluorapatite, can dissolve in hydrochloric acid. This reaction results in the release of calcium, phosphate, and fluoride ions into the solution. The rate and efficiency of dissolution depend on factors such as acid concentration, temperature, and reaction time [61].

$$Ca_5(PO_4)_3F + 10H_2O + 5H_2SO_4 \xrightarrow{Heat} 3H_2PO_4 + 5\ CaSO_4.2H_2O + HF \qquad (I.\ 5)$$

- ✓ Hydrothermal treatment

Hydrothermal treatment involves subjecting fluorapatite to high temperatures and pressures in the presence of water or other solvents. This process can alter the crystal structure and facilitate mineral decomposition [71,72].

- ✓ Mechanical methods

Physical methods involve breaking down the mineral through mechanical means. Grinding or milling fluorapatite reduces its particle size, increasing the surface area for available subsequent chemical reactions [63].

- ✓ Microwave-assisted methods

Microwave-assisted methods have been used in mineral processing. Microwave radiation can enhance the efficiency of certain chemical reactions or decomposition processes [74,75].

- ✓ Thermal decomposition

Heating fluorapatite to high temperatures (1645 °C) can cause thermal decomposition. This process may lead to the release of volatile components, leaving behind the remaining solid products, as described by the following reaction [76,56,77].

$$Ca_{10}(PO_4)_6F_2 \rightarrow 3Ca_3(PO_4)_2 + CaF_2 \qquad (I.\ 6)$$

$$3Ca_{10}(PO_4)_6F_2 \rightarrow 2Ca_3(PO_4)_2 + 6Ca_4(PO_4)_2O + 2\ POF_3 \qquad (I.\ 7)$$

IV.5. Role of fluorapatite in cement clinkerization

Fluorapatite within hydraulic cement systems can influence cementitious properties, setting characteristics, and concrete durability. Understanding these interactions is essential for optimizing cement formulations and achieving desired performance outcomes.

Xie et al. investigated the influence of fluorapatite on mineral formation and composition of cement clinker. Raw material mixtures containing varying phosphorus levels (0-5% FAp) were prepared using industrial materials such as phosphorus-bearing limestones, normal limestones, clays, and iron ore tailings. The findings revealed a gradual decrease in tricalcium silicate (C_3S) and tricalcium aluminate (C_3A) as fluorapatite content increased, while dicalcium silicate (C_2S) and free calcium oxide (CaO) showed corresponding increases. This study contributes to understanding how fluorapatite influences the critical mineral components of cement clinker, with potential implications for optimizing cement production and enhancing overall cement quality [66].

Staněk et al. assessed the phase composition of the clinkers burned to equilibrium using optical point counting method. The incorporation of P_2O_5 into clinker minerals was determined via electron microprobe analyses. The results demonstrated that at 0.7 wt.% of P_2O_5 in the clinker, C_3S content decreased while C_2S content increased. Notably, at a P_2O_5 content of 4.5 wt.%, the formation of C_3S was completely inhibited, leading to the production of clinker containing free lime in equilibrium with C_2S. These findings provide into the complex effects of phosphorous pentoxide on Portland clinker composition and formation, suggesting potential implications for refining cement manufacturing processes [67].

Boughanmi et al. focused on the mineralogy and reactivity of clinkers produced by incorporating natural fluorapatite into raw meals, with concentrations ranging from 0% to 15%. The findings indicated that fluorine stabilizes C_3S and β-C_2S, which remain present even at elevated P_2O_5 levels. Cement formulations incorporating up to 8% natural fluorapatite demonstrated acceptable properties, suggesting that natural fluorapatite holds significant potential as a decarbonized CaO source, thereby contributing to the reduction of CO_2 emissions in the cement industry.

A related study explored the impact of P_2O_5 on the mineralogical composition and reactivity of Portland cement (PC) through an industrial series of clinkers obtained from the same Tunisian cement plant. Samples were categorized based on P_2O_5 content manufactured under identical thermal and cooling conditions. The reactivity of cement prepared from these clinkers was monitored using isothermal calorimetry, and the compressive strength of resulting cement pastes was measured. The findings indicated that, within this specified range, phosphorous content did not significantly affect clinker mineralogy, cement reactivity, or concrete performance [80,81].

De Noirfontaine et al. conducted a comprehensive investigation of the triclinic T1 polymorph of C_3S (alite) doped with P_2O_5 in the range of 0-0.9 wt.%. All samples were characterized using XRD, SEM. The study observed the emergence of a phosphorus-rich phase with a structure derived from the belite polymorph. With increasing phosphorus content, alite progressively decomposition into free lime and belite. The C_2S phase was detected starting from 0.1 wt% P_2O_5 and was located at the interfaces of alite grains [69].

Yu, Jincheng, et al. investigated low-cost Magnesium Phosphate Cement (MPC) mortars containing ye'elimite. The study analyzes setting times, fluidities, hydration temperature developments, and compressive strength variations in magnesium phosphate mortars with ye'elimite. It compared the development of compressive strength, flexural strength, and bond strength under air and water curing conditions. Additionally, the study explored phase developments, microstructures, and pore diameter distribution in these mortars. Results showed that mortars with 51% ye'elimite and 26% MgO had a setting time of 27 minutes, free fluidity of 150 mm, a 3h compressive strength of 41 MPa, a 7-day compressive strength of 58 MPa, and 180-day compressive strength of 74 MPa. Ye'elimite promotes amorphous hydration products, while water curing enhanced hydration, leading to denser structures and higher strengths [70].

This study details the preparation of a sulfoaluminate-magnesium potassium phosphate cementitious composite material under low-temperature conditions:

Changzai, et al. detailed the preparation of a sulfoaluminate-magnesium potassium phosphate cementitious composite material under low-temperature conditions. The process involved selecting sulphoaluminate, magnesium, and potassium phosphate components, blending them in controlled proportions at low temperatures, and adding water to achieve the desired consistency. The material underwent low-temperature curing, with testing focusing on setting time, compressive strength, and durability. Optimization involved adjusting formulation and temperature control to develop a construction material with specific performance characteristics suitable for low-temperature applications [71].

CHAPTER II

Materials and experimental techniques

This chapter is focuses on elucidating the experimental materials, the methodologies applied in the preparation of powders and sintered samples, and the equipment used for the physico-chemical and microstructure characterization of the investigated samples.

II. 1. Materials used in the experiment

In this study, ye'elimite based multiphase composites were prepared using a raw mixture of natural materials. The components included the following: natural phosphates, bauxite, gypsum, and quartz. Additionally, laboratory magnesium oxide was included in the formulation.

II. 1.1. Natural Phosphate

Natural phosphate in Algeria is commonly found in various geological formations, and the country possesses significant phosphate reserves. The natural phosphate used in this study was obtained from the Al-Onq mountain, situated near Tebessa in southeastern Algeria. The Al-Onq mountain is recognized for its deposits of natural phosphate, a valuable raw material with applications in various industries, including agriculture and the fertilizers production. Algeria's natural phosphate resources play a crucial role in meeting both domestic and industrial needs, making them an important element in the country's natural resource portfolio [85,86].

Fig.II.1. Photo of natural FAp powder.

II.1.2. Bauxite

Bauxite is a naturally occurring ore that serves as the primary source of aluminum, it is composed mainly of hydrated aluminum oxides such as gibbsite, boehmite, and diaspore, along with impurities like iron oxides, silica, and titanium dioxide. This ore forms through the weathering and leaching of alumina-rich rocks in tropical or subtropical regions. The vast majority of mined bauxite (over 95%) is processed into alumina, which is primarily used in aluminum production, while the remainder is utilized in non-metallic applications like ceramics and refractories. As a critical industrial mineral, global bauxite production exceeds 50 million tons annually [73]. The bauxite used in this study was sourced from TREFISOUD /El-Eulma, where industries involved in metal smelting [74].

Fig.II.2. Photo of Bauxite powder.

II.1.3. Gypsum

Gypsum is a vital mineral in Algeria, extensively found in regions like Béchar, Tébessa, Biskra, and M'Sila. The gypsum used in this study is sourced from Boussaâda. It commo,ly occurs within sedimentary and evaporitic formations [75].

Fig.II.3. Photo of natural gypsum.

Algeria has considerable gypsum reserves, which are essential for industries like cement production, where gypsum serves as a setting retarder, and for the manufacturing of plaster used in both construction and decorative applications. The country's gypsum sector holds strong growth potential, particularly in the development of value-added products such as environmentally friendly building materials and lightweight plasters, aligning with global sustainability trends [76].

II.1.4. Quartz

Natural quartz is frequently used as a primary ingredient in cement manufacturing. It is a mineral composed of silicon and oxygen atoms, classified within the silicate mineral group. Naturally abundant, quartz can be sourced from various locations, rendering it a readily accessible and economical constituent [91,92]. In is study, we employed natural quartz sourced from Boussaâda in southern Algeria. Below are some key characteristics and benefits of natural quartz:

Fig.II.4. Photo of natural quartz.

- ✓ When added to cement formulations, it helps control concrete expansion, which is crucial for preventing cracks and ensuring structural integrity [78].
- ✓ Quartz-containing cement formulations are often used in repair and restoration projects. The durability and strength provided by quartz contribute to the longevity of repaired structures [79].

II. 1.5. Magnesium oxide

Magnesium oxide (MgO) with high purity (99%, provided by Sigma-Aldrich) is widely utilized across multiple industries owing to its distinctive properties. Some of the common applications of magnesium oxide include [80]:

- ✓ Refractory Materials: Magnesium oxide is a key component in refractory materials, particularly in the production of refractory bricks and crucibles. Its high melting point and resistance to heat make it ideal for use in furnaces and kilns [81].
- ✓ Construction Industry: MgO is used in producing of magnesium oxychloride cement and magnesium oxide boards, known for their fire resistance and insulating properties [82].
- ✓ Light-burned MgO is used as an expansive agent to reduce shrinkage in cement-based materials (e.g., shrinkage-compensating concrete) [83].
- ✓ MgO can combine with alumina in calcium aluminate cements to form spinel ($MgAl_2O_4$), which enhances thermal and mechanical properties [84].

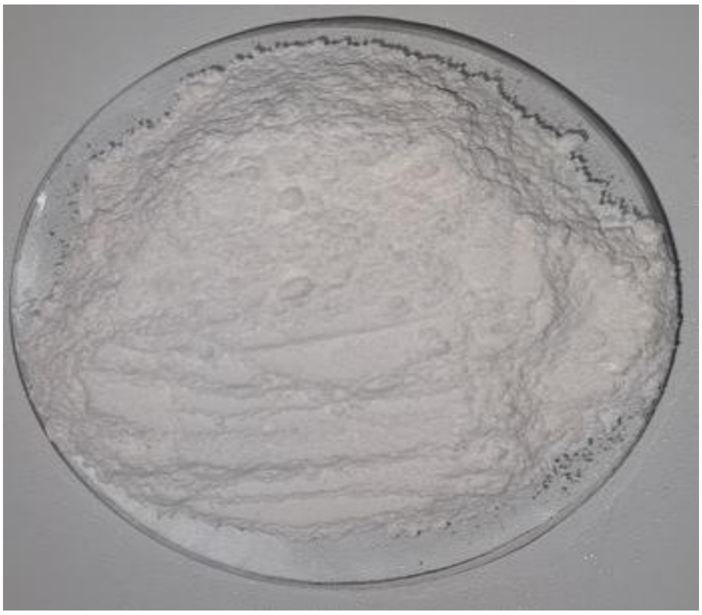

Fig.II.5. Photo of MgO powder.

II.2. Preparation of powders and samples

II.2.1. Preparations of powders by attritor ball milling

The raw materials used in the first experiment included natural fluorapatite, bauxite, and gypsum as the base mixture, with varying amounts of quartz and magnesium oxide added:

- ✓ Different quantities of quartz (0, 2.1, 3.8, and 5.4 wt%) were blended with the base mixture. The resulting samples were labeled as M-0Q, M-2,1Q, M-3,8Q, and M-5,4Q, corresponding to the respective quartz weight percentages.

Table II. 1 Amounts (wt%) of the initial raw mixtures.

Samples name	Fluorapatite	Bauxite	Gypsum	Quartz
M-0Q	43.20	44.50	22.10	0
M-2.1Q	46.67	40.76	20.24	2.1
M-3.8Q	49.62	37.61	18.68	3.8
M-5.4Q	52.13	34.91	17.33	5.4

- ✓ The raw materials were then mixed with different proportions of high-purity MgO (≥ 99 wt%), supplied by Sigma-Aldrich. Different quantities of MgO (0, 2, 4, and 6 wt%) were blended with the base mixture. The resulting samples were labeled as 0%MgO, 2%MgO, 4%MgO, and 6%MgO, corresponding to the respective magnesium oxide weight percentages. Table (II. 2) provides a detailed overview of the specific quantities of raw materials used in the preparation of each synthesized sample.

Table II. 2 Amounts (wt%) of the initial raw mixtures.

Samples name	Fluorapatite	Bauxite	Gypsum	MgO
0%MgO	38	40	22	0
2%MgO	37.24	39.2	21.56	2
4%MgO	36.48	38.40	21.12	4
6%MgO	35.72	37.60	20.68	6

The powder preparation process involved wet milling the raw materials with zirconia pellets (4-5 mm in diameter) in a mixture of distilled water. The raw materials were maintained at a 1:10 mass ratio relative to the pellets. Milling was conducted for 2 hours at a rotation speed of 700 rpm using an attritor-stirred ball mill (model JM-1) [85], as illustrated in Fig.II.6. After milling, the mixture was dried at 120 °C for 24 hours and subsequently ground manually using a mortar. The ground material was sieved through a 100 µm mesh to obtain particles smaller than 100 µm. The obtained powder was calcined at 1000 °C for 2 hours with a heating rate of 10 °C/min to eliminate residual organic compounds and reduce the risk of swelling or cracking during sintering. The calcined powders were then uniaxially pressed at 100 MPa to form disc-shaped samples with a diameter of 13 mm. The samples were sintered at temperatures between

1100 °C and 1500 °C for a duration of 2 hours, with a heating rate of 10 °C/min, using Nabertherm electric furnace, reaching a maximum temperature of 1750 °C (University of M’sila).

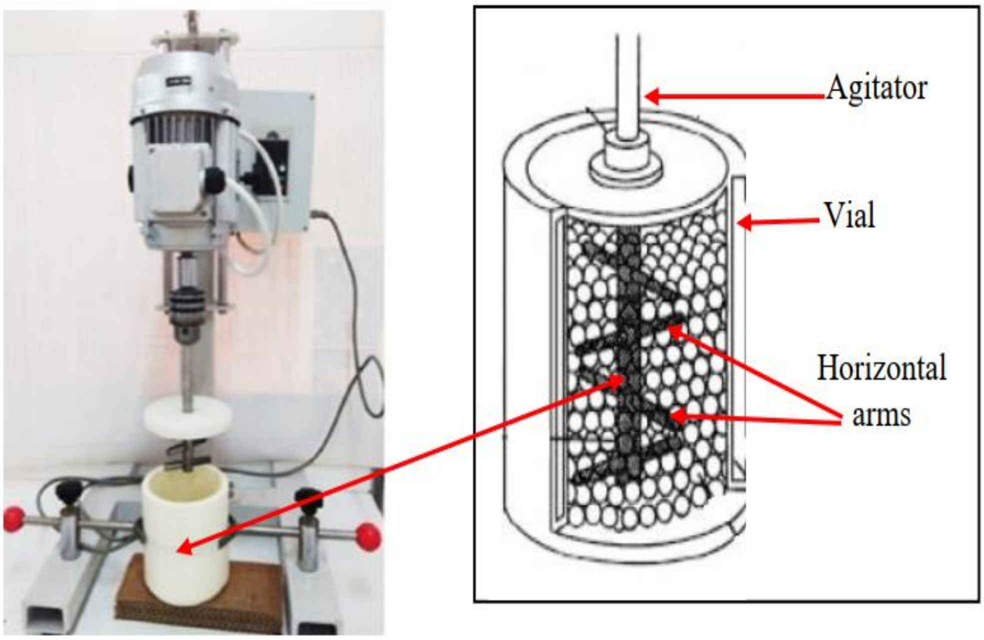

Fig.II.6. Attritor ball mill and a diagram illustrating the motion of the balls inside the mill.

II.3. Technical Properties

II.3.1. Particle size distribution

Particle size distribution (PSD) is a fundamental physical property of a powder and it is often determined using a technique based on the forward diffraction of a laser beam by particles. In this method, the angle of diffraction is inversely proportional to the particle size, and the intensity of the diffracted beam at any angle provides a measure of the number of particles with a specific cross-sectional area in the path of the beam.

Two optical models commonly employed to calculate PSD are the Fraunhofer diffraction model and the Mie theory [101,102]. The particle-size distribution of the sample powders was determined using a Mastersizer 3000 laser size analyzer manufactured by Malvern PANalytical (Lafarge cement, M'sila). This instrument utilizes laser diffraction principles to analyze the particle size distribution, as shown in Fig.II.7.

Fig.II.7. MAZ 3000 laser granulometry.

II.3.2. X-ray fluorescence

X-ray fluorescence (XRF) analysis is a technique used to determine the elemental composition of a sample by measuring the characteristic X-rays emitted when the sample is irradiated with X-rays. This technique can be used to a wide variety of materials. Under irradiation, the atoms in the sample transition from their fundamental state to an excited state. Since the excited state is unstable, the atoms tend to return to their fundamental state be emitting energy, especially in the form of X-photons. This phenomenon, known as XRF, involves the secondary emission of X-rays. Analysis of this secondary emitted X-rays gives the nature and the concentration of the chemical elements present in the sample [87].

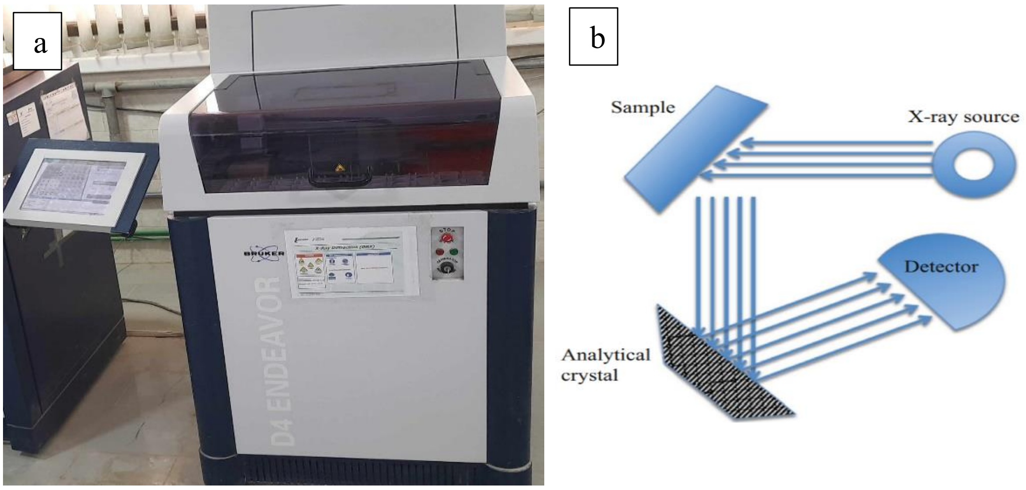

Fig. II.8. (a) XRF D4 ENDEAVOR model by BRUKER, and (b) schematic diagram illustrating the X-ray detection system used in the X-ray Fluorescence technique.

The chemical analysis of the raw materials was conducted using XRF, specifically the D4 ENDEAVOR model by BRUKER (Lafarge Holcim from M'sila), as shown in Fig.II.8. The samples were prepared as fused beads using glass discs, which were created by melting approximately 1 ± 0.001 g of sample powder with 10 ± 0.001 g of di-lithium tetraborate. Loss on ignition was determined for samples treated at 950 °C for 30 minutes. The oxide contents are reported in weight percent (wt%).

II.3.3. X-ray diffraction (XRD) analysis using X'Pert HighScore Plus software

The X-ray diffraction method is analytical technique used for characterizing crystalline and semi-crystalline materials. It can also provide certain insights into solid and liquid amorphous materials. This technique facilitates the examination of various aspects of crystallographic structure, including the degree of crystallinity, crystallite size, and preferred orientation in solid polycrystalline or powder samples, and crystal imperfections such as deficiencies or excesses in elements [103,104].

Furthermore, XRD can be used to identifying phases within samples and is particularly effective in distinguishing between phases that share the same chemical composition but possess different crystal structures, commonly known as polymorphs. The widely employed method for this purpose is X-ray powder diffraction (XRPD), which is extensively utilized for identifying unknown substances by comparing diffraction data with a curated Powder Diffraction File (PDF) database maintained by the International Center for Diffraction Data (ICDD) [88].

Additionally, XRPD can be applied to characterize heterogeneous solid mixtures, allowing for the determination of the relative abundance of crystalline compounds. When combined with lattice refinement methods, such as Rietveld refinement, X-ray diffraction can offer structural insights into materials. XRD involves the elastic scattering of X-ray photons by atoms arranged in a periodic lattice [89]. When scattered monochromatic X-rays are in phase, they undergo constructive interference [90]. Utilizing Bragg's law, XRD with crystal planes enables the derivation of lattice spacings:

$$2d.\sin \theta = n.\ \lambda$$

Where θ is the angle between the incident ray and the scattering planes, d is the spacing between the planes in the atomic lattice, n: is an integer determined by the diffraction order, and λ is the wavelength of the X-rays. Fig.II.9 illustrates a schematic depicting representation of the fundamental principle of X-ray diffraction analysis.

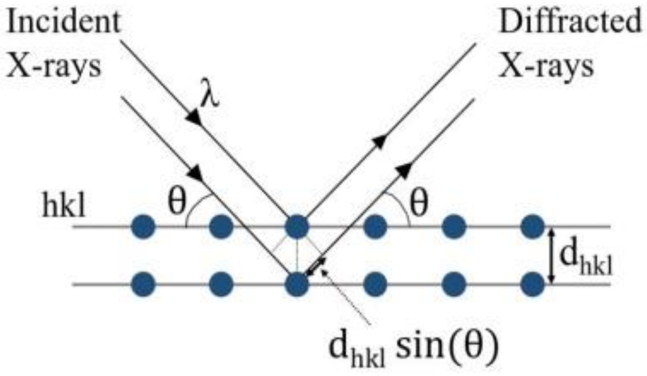

Fig.II.9. the fundamental principle of X-ray diffraction analysis.

The identification of phases in both the powders and sintered composites was performed using X-ray diffraction (XRD) with CuKα radiation, utilizing an X'Pert Pro instrument from Panalytical. The XRD analysis was conducted at 40 kV and 30 mA, with a scan speed of 4°/min and a step scan of 0.026°, as shown in Fig.II.10. The scanning range covered 2θ from 10° to 70°. To identify the phases present, the XRD patterns of the samples were compared with the database provided by the Joint Committee on Powder Diffraction Standards (JCPDS) using the High Score program (Qatar University).

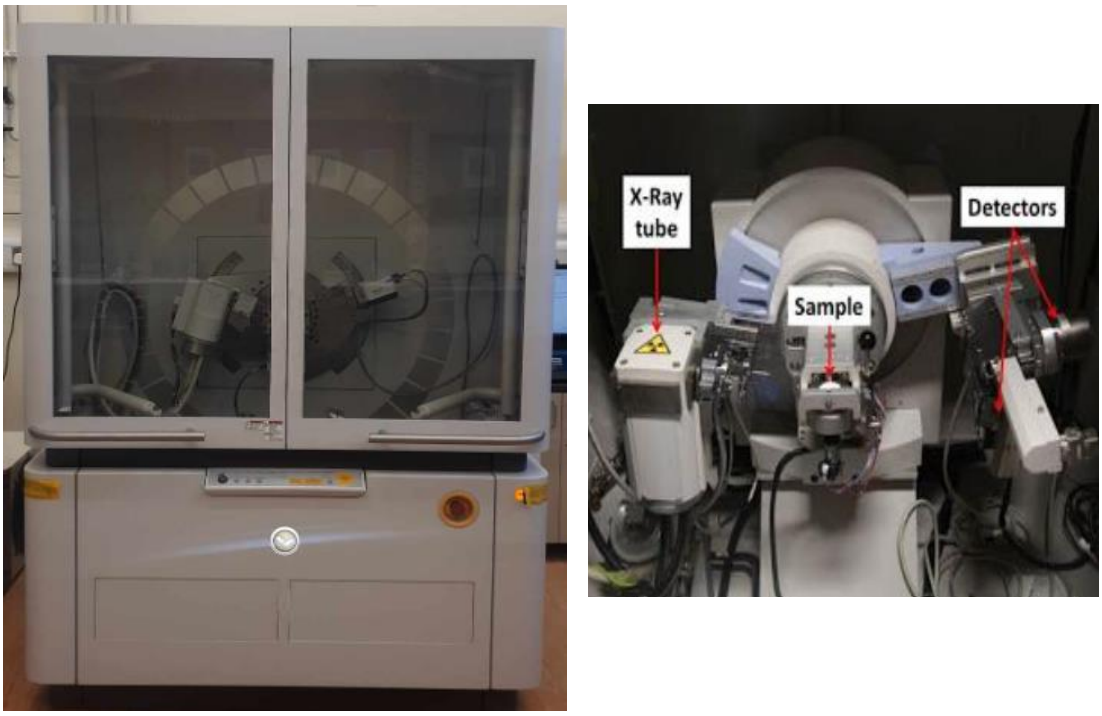

Fig.II.10. Panalytical X'pert Pro, XRD.

II.3.4. Analysis of X-ray Diffraction data using the Rietveld method

Many XRD analysis techniques rely on measuring the height or area of individual diffraction peaks. In contrast, the Rietveld method stands out by considering various additional factors. Unique features of this method include accounting for background noise signals, resolving overlapping peaks, and incorporating data collected across both small and large angles. The Rietveld method is capable of simulating a complete diffractogram when specific parameters, such as the space group, dimensions of the elementary cell, the type of atoms present, and the relative coordinates of atoms within the lattice, are known [108,109].

These factors are crucial for evaluating the agreement between the experimental and calculated diffraction patterns in Rietveld refinement, providing insights into the quality of the fit [92]:

$$\mathrm{Rwp} = \sqrt{\sum\nolimits_{i} \frac{w_i (I_{iM} - I_{iC})^2}{w_i (I_{iM})^2}}$$

$$\mathrm{Rexp} = \sqrt{\sum\nolimits_{i} \frac{N - P}{w_i (I_{iM})^2}}$$

$$\mathrm{GOF} = \left(\frac{\mathrm{Rwp}}{\mathrm{Rexp}}\right)^2$$

Where:

Rwp: weighted profile R-factor

Rexp: expected R-factor

GOF: goodness of fit

I_{iM}: is the measured intensity at data point i.

I_{iC}: is the calculated intensity at data point i.

N: is the number of data points.

P: is the number of refined parameters.

w_i: is the attributed weight for data point i.

In this study, the quantification of mineral phases in the synthesized samples was performed using the Rietveld refinement software Profex, as depicted in Fig.II.11. Profex stands out as an open-source, platform-independent solution designed for the analysis of powder X-ray diffraction datasets. It is based on the BGMN refinement kernel and incorporates a description of the diffractometer configuration to determine the instrument-related peak profile [111,112].

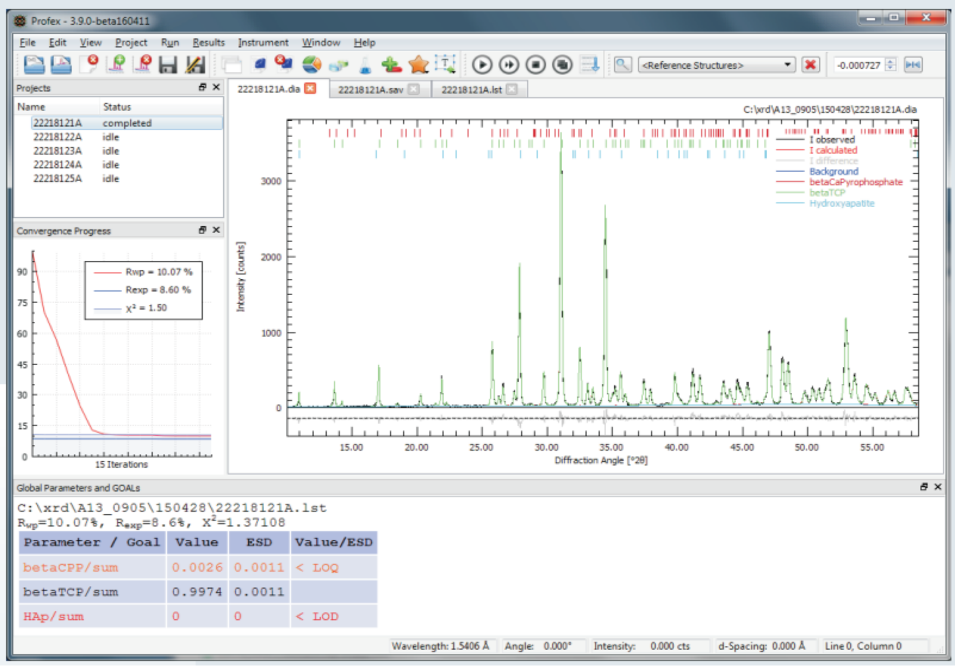

```
C:\xrd\A13_0905\150428\22218121A.lst
Rwp=10.07%, Rexp=8.6%, X²=1.37108
```

Parameter / Goal	Value	ESD	Value/ESD
betaCPP/sum	0.0026	0.0011	< LOQ
betaTCP/sum	0.9974	0.0011	
HAp/sum	0	0	< LOD

Fig.II.11. Model about PROFEX (Open Source) XRD and Rietveld Refinement.

II.3.5. Thermal analyzes (DTA and TGA)

When materials undergo heat treatment, various changes occur, including phase transitions, state alterations, and compositional modifications. A set of thermal analysis methods is employed to quantify these changes, including Differential Thermal Analysis (DTA), Thermogravimetric Analysis (TGA).

- DTA measures the temperature difference between a sample and a reference (a thermally inert material) as a function of time or temperature while both are subjected to a controlled heating program. Using the DTA method, any transformation is detectable for all categories of materials [113,114]. In this study, DTA was used to study the thermal behavior of the prepared mixtures, using a LABSYS Evo DSC Setaram (1600 °C) at the University of M'sila, with a heating rate of 10 °C/min from 25 to 1350 °C.
- TGA is a technique that measures the variation in mass of a sample when it is subjected to a controlled temperature program in a specific atmosphere. This variation can

manifest as a mass loss (due to the emission of steam or other gases) or a mass gain (due to gas fixation, oxidation, etc.). TGA was used to examine the thermal properties of the prepared mixtures using a METTLER TOLEDO at the National Polytechnic School of Constantine through IBTIKAR-DGRST. The analysis was performed with a heating rate of 10 °C/min over a temperature range of 25 to 1350 °C.

II.3.6. Fourier Transform Infrared (FTIR)

Fourier Transform Infrared (FTIR) spectroscopy is a widely utilized and potent method for exploring a broad spectrum of substances, investigating their characteristics, and studying their behavior under diverse conditions. Infrared (IR) spectra reflect the distinctive bonds present in molecular entities or in extended bonded structures like solid lattices. As a result, these spectra are commonly employed for substance identification, quality assessment, impurities detection, and alterations. The infrared portion of the electromagnetic spectrum is divided into near, mid, and far infrared. The mid-infrared range (approximately 4000-400 cm^{-1}) is particularly suitable for examining molecular vibrations and the associated vibrational-rotational structure [87].

In this study, The FT-IR analysis was conducted using a Cary630KBr Engine (Agilent Technologies) at room temperature (Fig.II.12). Infrared spectra were recorded in the wavelength range from 4000 cm^{-1} to 400 cm^{-1} with a spectral resolution of 2 cm^{-1}.

Fig.II.12. Cary630KBr Engine, Agilent Technologies FT-IR spectrometer (Univ-M'sila).

II.3.7. Measurement of bulk density and open porosity

We applied Archimedes principle in our measurements to assess the bulk density and open porosity of sintered samples at different temperatures. The methodology involves a series of steps, including precise mass measurements and the replacement of air with xylene. Here's a breakdown of the procedure [66,68]:

- ✓ Mass measurement in air

Initially, the mass of the sintered sample is measured in the air using an electromechanical balance with a sensitivity of approximately 10^{-4} g.

- ✓ Air removal and xylene replacement

A vacuum pump is then employed to extract air from the sample under low pressure. Once a vacuum is created within the sample, xylene is introduced to replace the air, filling the voids within the material.

- ✓ Mass measurement in air and water

After the air has been replaced with xylene, the mass of the sample measured again in air. The sample is then immersed in water, and its mass is measured once more to determine its buoyant mass in water.

- ✓ Calculation of bulk density

The bulk density is determined by dividing the mass of the sample in air by its total volume, taking into account the replaced with xylene. The equation for bulk density (ρ_{bulk}) is typically expressed as:

$$\rho_{bulk}\ (g/cm^3) = \frac{m_1 de}{(m_2 - m_3) - (m_2 - m_1) de/\ dx}$$

Where:

m_1: the mass of the sample in the air.

m_2: the mass of the sample filled with xylene in air.

m_3: the mass of the sample filled with xylene in water.

de: the density of water (0.9989 g/cm3).

dx: density of xylene (0.88 g/cm3).

- ✓ Calculation of Open Porosity: The ratio of open porosity to the total volume is determined by comparing the mass of the sample in air with its buoyant mass in water. The equation for open porosity (O.P %) can be expressed as:

$$\text{O.P (\%)} = 100\,\frac{m_2-m_1}{m_2-m_3}$$

II.3.8. Micro-hardness (Vickers hardness)

Micro-hardness, denoted as HV, is a measure of a material's resistance to indentation or penetration at a microscopic scale. It is typically expressed in Vickers hardness units (HV). The Vickers hardness test involves pressing a diamond indenter into the material, and the hardness value is determined based on the size of the resulting impression [115,116].

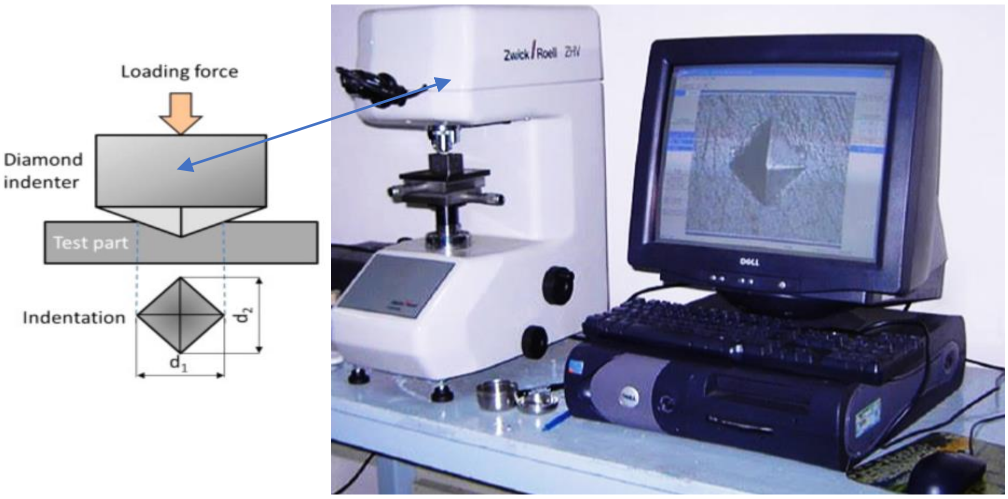

Fig.II.13. Zwick Roell Indentec apparatus, along with a schematic illustration depicting the operational principles of HV testing.

The micro-hardness value (HV) is calculated by dividing the applied force (in kilograms-force) by the surface area of the indentation (in square millimeters, mm^2). The formula for calculating Vickers hardness (HV) is [96]:

$$H_V = 1.854 \times \frac{P}{D^2}$$

Where:

H_V: is the microhardness value.

P: is the applied load.

D^2: is average diagonal lengths = ($\frac{d_1+d_2}{2}$).

In this work, the hardness of the sintered samples was assessed using a Vickers microhardness testing machine, specifically the Zwick Roell Indentec model. The measurements were conducted under an indentation load of 300 g with a loading time of 10 seconds. To ensure accuracy, the samples were meticulously polished before testing. The procedure involved taking five to ten measurements on each sample, and the average hardness was determined based on these measurements, following the established protocol.

II.3.9. Scanning electron microscope

The scanning electron microscope (SEM) is a microscopy technique that generates diverse images by directing a high-energy electron beam onto a sample's surface and capturing signals resulting from the interaction of incident electrons with the sample surfaces (see Fig.II.14). The signals collected in SEM include secondary electrons, sample-specific characteristics, and other interactions occurring near the surface of the sample. In its secondary electron imaging mode, SEM generates detailed, high-resolution images of a sample's surface [87].

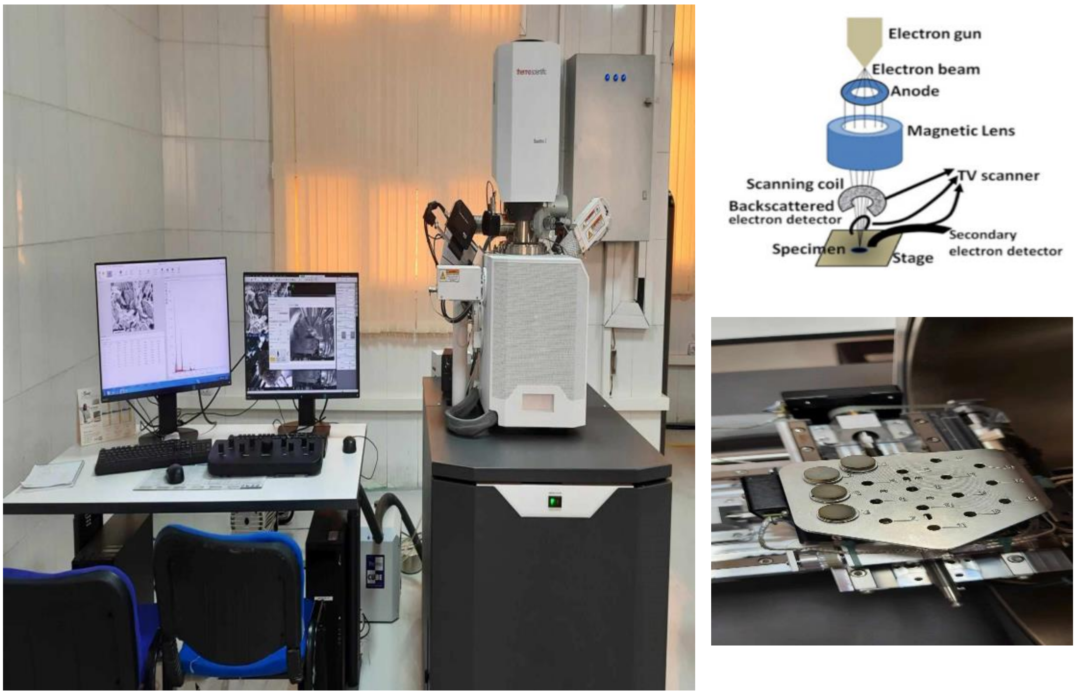

Fig.II.14. Thermo Scientific (Quattro S) SEM and schematic illustration depicting the operational principles of SEM testing.

The extensive depth of field and broad magnification capabilities establishes SEM one of the most widely recognized and extensively used imaging technologies. Backscattered electrons, emitted by the sample, can be employed independently to create an image, offering chemical contrast. Alternatively, they can be combined with characteristic X-rays for determining the elemental composition of the sample [97].

In our study, the SEM analysis was performed using a Thermo Scientific (Quattro S) brand from CRAPC Laghouat and SEM Quanta 650 FEG, manufacturer: FEI (Thermo Fisher) (Hillsboro, USA) from Hamad bin Khalifa University.

CHAPTER III

Results and Discussions

Part 01: *The effect of quartz on natural fluorapatite decomposition during the preparation of calcium sulfoaluminate-based multiphase composites*

This section of the chapter examines the effect of quartz on the decomposition of natural fluorapatite during the preparation of calcium sulfoaluminate-based multiphase composites. The study investigates how quartz influences key aspects of the sintering process, including densification, phase formation, and structural evolution. By analyzing the role of quartz as an additive, this research provides insights into its impact on the physicochemical properties of the final composites. The findings contribute to a better understanding of the sintering mechanisms and offer guidance for optimizing the production and potential applications of ye'elimite-based materials.

III.1. Physicochemical analyses of the initial materials

III.1.1. XRF Analysis of starting materials

In this study, we used natural phosphate (fluorapatite), bauxite, gypsum, and quartz as starting powder. The chemical compositions of these powders, determined by XRF, are given in Table (III. 1). The natural phosphate used was mainly composed of calcium oxide (CaO) and phosphorus pentoxide (P_2O_5). On the other hand, bauxite, gypsum and sand are mainly composed of alumina (Al_2O_3), calcium oxide (CaO) and sulfur trioxide (SO_3), and silica (SiO_2), respectively.

Table III. 1: Chemical composition (wt%) of the fluorapatite, bauxite, gypsum and quartz used in this study.

	SiO_2	Al_2O_3	Fe_2O_3	CaO	MgO	SO_3	K_2O	Na_2O	P_2O_5	TiO_2	F	LOI
Fluorapatite	2.49	0.34	0.28	49.03	1.29	2.22	0.088	0.93	28.7	0.034	3.63	10.73
Bauxite	4.96	87.6	1.90	0.30	0.30	0.18	0.70	0.03	0.07	3.96	0.00	-
Gypsum	0.075	0.037	0.055	33.05	0.05	45.11	0.00	0.00	0.092	0.011	0.00	21.01
Quartz	98.73	0.50	0.10	0.40	0.00	0.00	0.20	0.00	0.018	0.06	0.00	-

III.1.2. XRD Analysis of starting materials

The XRD patterns of the raw materials used in this study are shown in Fig (III.1). Fig (III.1-a), shows that the natural phosphate powder consists mainly of fluorapatite and carbonate fluorapatite (francolite, $Ca_{10}(PO_4, CO_3)_6F_2$) as the major phase. It also contains very little amounts of dolomite and quartz. Fig (III.1-b) presents the XRD spectrum of bauxite, revealing that alumina as the major phase. On the other hand, a very small proportion of aluminum titanite and quartz. The XRD spectra related to quartz and gypsum contain a single phase of quartz and gypsum, as shown in Fig (III.1-c) and Fig (III. 1-d), respectively.

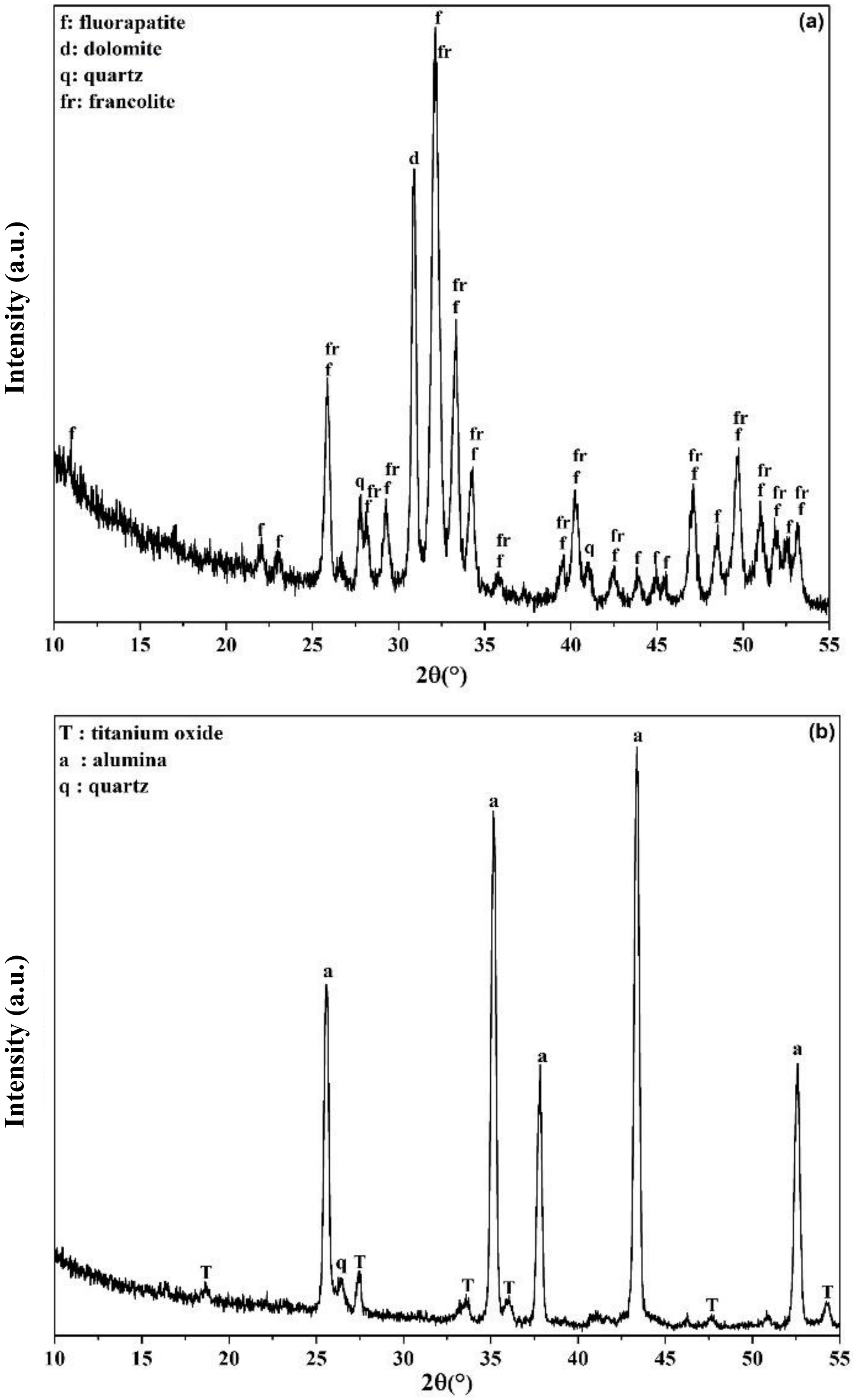
f: fluorapatite
d: dolomite
q: quartz
fr: francolite
(a)
Intensity (a.u.)
2θ(°)
10
15
20
25
30
35
40
45
50
55
T : titanium oxide
a : alumina
q : quartz
(b)

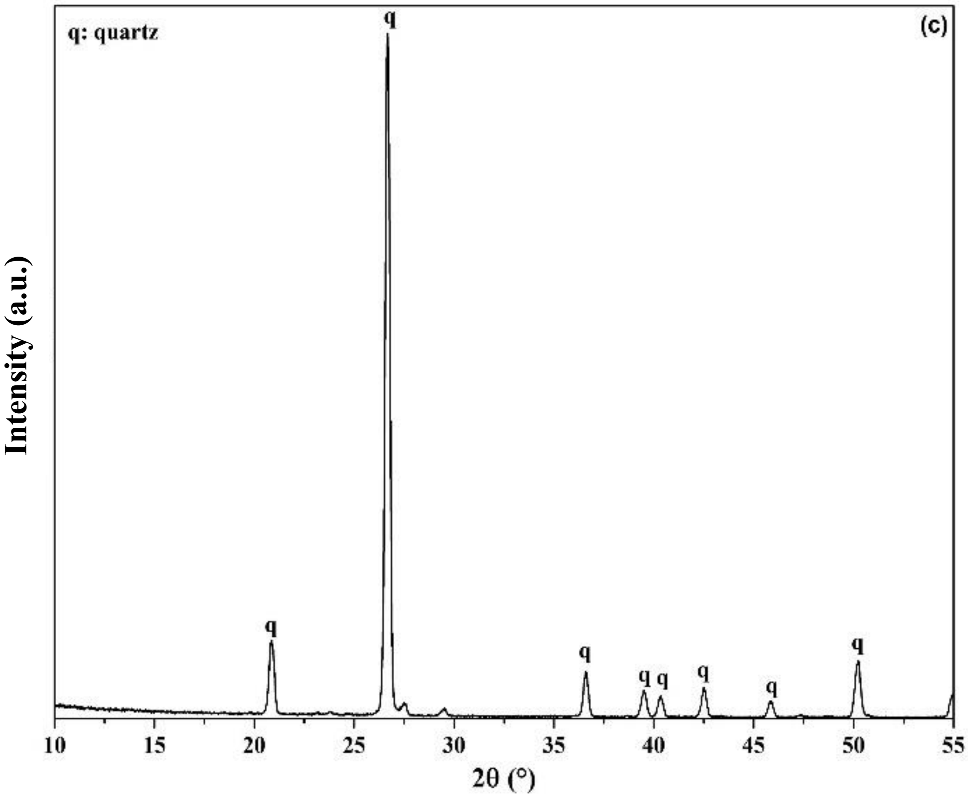

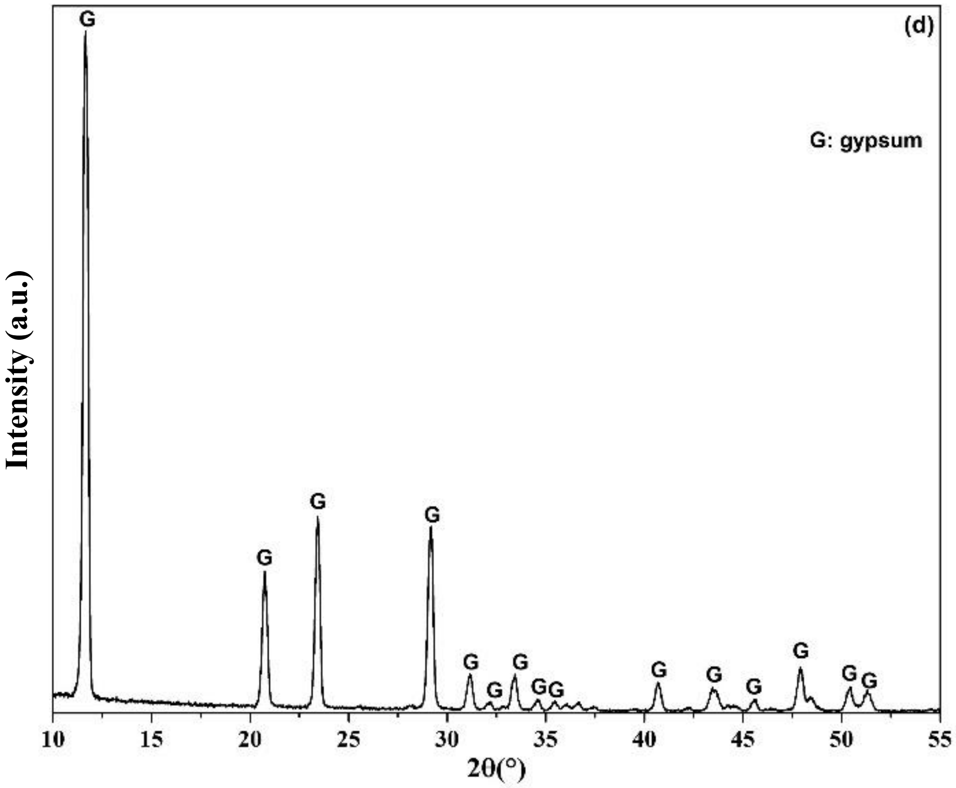

Fig.III.1. XRD patterns of raw materials: (a): natural fluorapatite, (b): bauxite, (c): quartz, and (d): gypsum used in this study.

III. 2. XRD analysis of milled powders after drying at 120 °C

Fig.III.2 presents the XRD patterns of the milled powders, which predominantly exhibit phases similar to those of the raw materials. However, certain mixtures reveal the emergence of a minor bassanite phase ($CaSO_4.1/2H_2O$), likely resulting from the drying temperature's effect on gypsum [98].

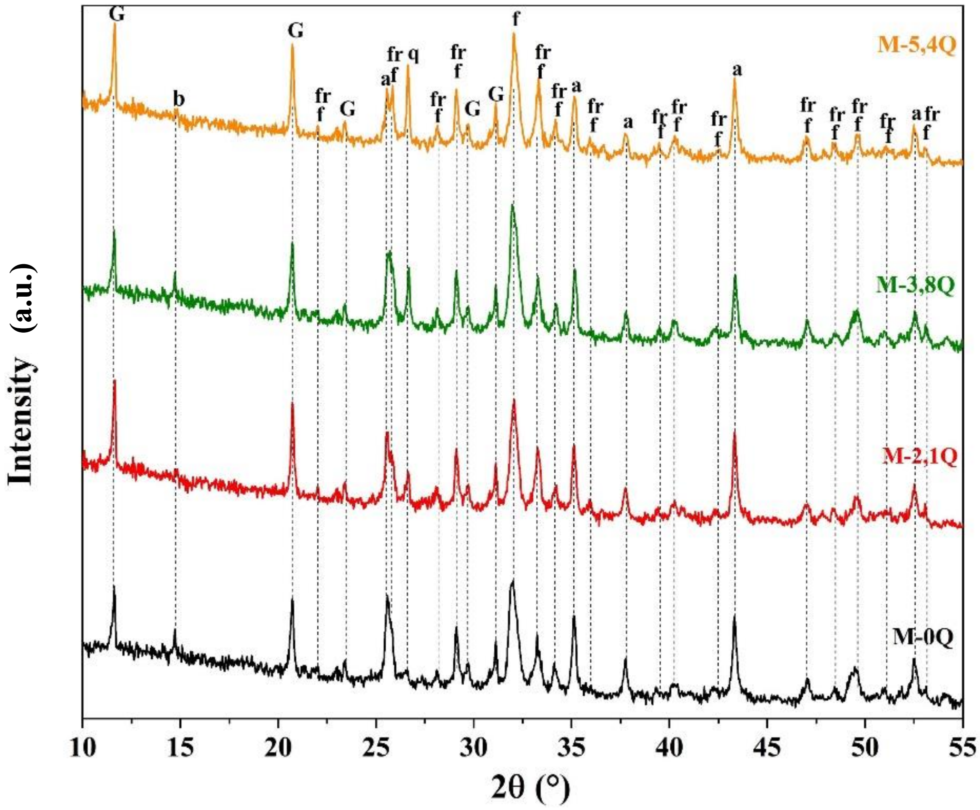

Fig.III.2. XRD patterns of composite powders after drying at 120 °C (G: gypsum, b: basanite, a: alumina f: fluorapatite, fr: francolite, q: quartz)

Fig.III.3 displays the particle size distribution of the milled composite powders, indicating a bimodal distribution. Most particles are concentrated in the smaller size range, with a primary peak between 1–10 µm. However, a secondary peak above 100 µm suggests the presence of larger particles or agglomerates in some samples.

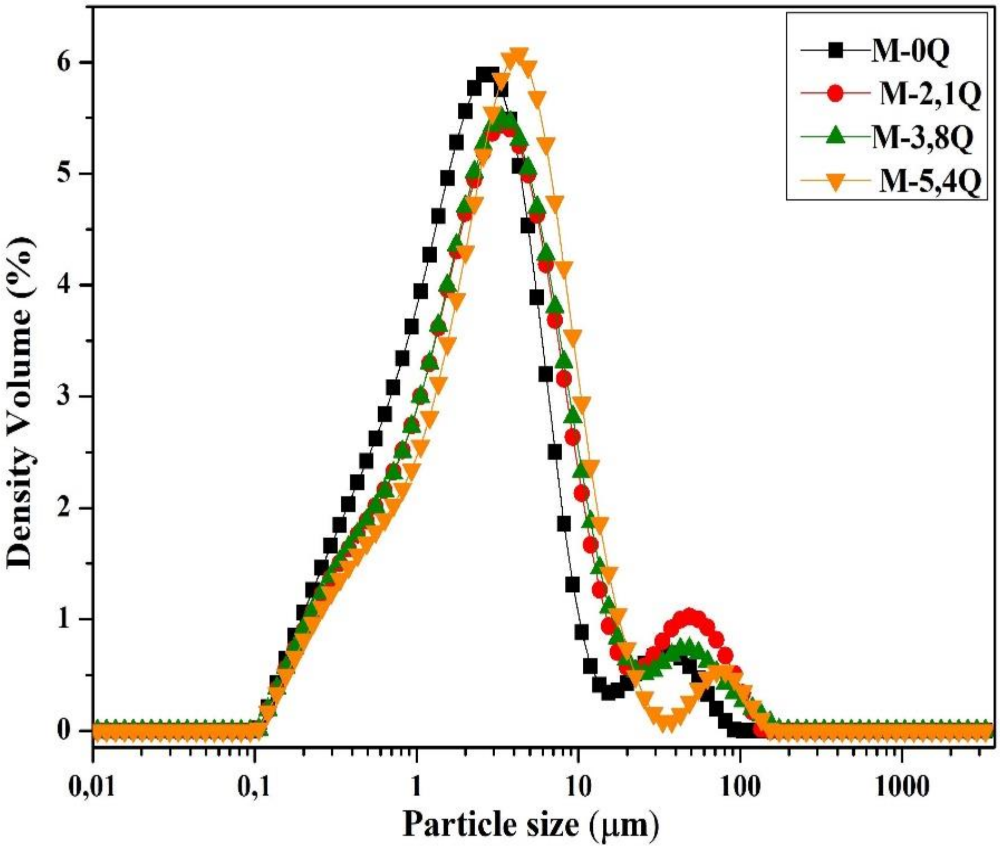

Fig.III.3. Particle size distribution of milled powders.

III.3. Differential Thermal Analysis of mixtures

Differential Thermal Analysis (DTA) was performed on the samples to investigate the thermal events occurring during the heating process. The resulting DTA curves are presented in Fig (III. 4). The first endothermic peak, located in zone 1 at approximately 135 °C, corresponds to the dehydration of gypsum, leading to water (H_2O) loss, as described by reactions (III. 1) and (III. 2) [119,120].

In zone 2, an endothermic peak around 850 °C is associated with the decarbonization of francolite ($Ca_{10}(PO_4, CO_3)_6F_2$) [121,122]. Zone 3 exhibits endothermic peaks between 1100 and 1200 °C, accompanied by the release of gases such as SO_2 and O_2, attributed to the decomposition of $CaSO_4$ [4] as per reaction (III. 3). In zone 4, an exothermic peak between 1250 and 1350 °C signifies the formation of $C_4A_3\$$, influenced by the presence of Al_2O_3 and SiO_2 [100–102]. These compounds reduce the decomposition temperature of $CaSO_4$, impacting calcium-based desulfurization [44].

Moreover, two exothermic peaks were observed in mixtures M-2.1Q and M-3.8Q, attributed to interactions among SiO_2, CaO, and Al_2O_3 occurring between 1250 and 1350 °C

[103], as confirmed by XRD analysis of samples treated at 1300-1350 °C [123-125]. The formation of ye'elimite can be explained by solid-state reactions between CaO, Al_2O_3, and $CaSO_4$, as represented by Eqs (III. 4) and (III. 5) [23].

$$CaSO_4.2H_2O \rightarrow CaSO_4.1/2\ H_2O + 3/2\ H_2O\uparrow \qquad \text{(III. 1)}$$

$$CaCO_4.1/2H_2O \rightarrow CaSO_4 + 1/2\ H_2O\uparrow \qquad \text{(III. 2)}$$

$$CaSO_4 \rightarrow CaO + 1/2\ O_2\uparrow + SO_2\uparrow \qquad \text{(III. 3)}$$

$$4\ CaO + 3\ Al_2O_3 + SO_3 \rightarrow Ca_4(AlO_2)_6SO_4 \qquad \text{(III. 4)}$$

$$3\ CaO + 3\ Al_2O_3 + CaSO_4 \rightarrow Ca_4(AlO_2)_6SO_4 \qquad \text{(III. 5)}$$

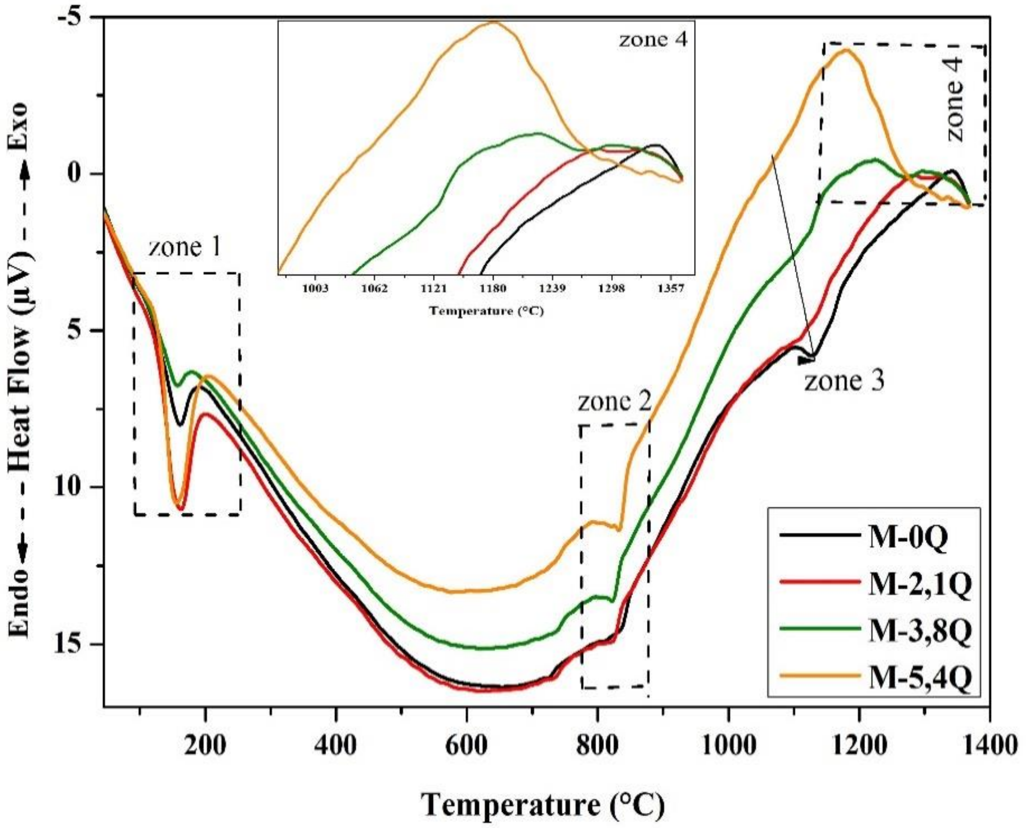

Fig.III.4. DTA curves of the raw mixture during heating process.

III.4. Analysis of shaped and sintered samples

III.4.1. X-ray analysis of samples after sintering

The XRD patterns of samples sintered at different temperatures are presented in Fig.III.5. At 1200 °C, the dominant phases observed in all samples are fluorapatite, alumina, and ye'elimite. Additionally, a minor amount of wollastonite ($CaSiO_3$) is detected in mixtures containing quartz, resulting from the reaction between free calcium oxide and silicon dioxide, as described by Eq (III. 6) [104]:

$$CaO + SiO_2 \rightarrow CaSiO_3 \qquad \text{(III. 6)}$$

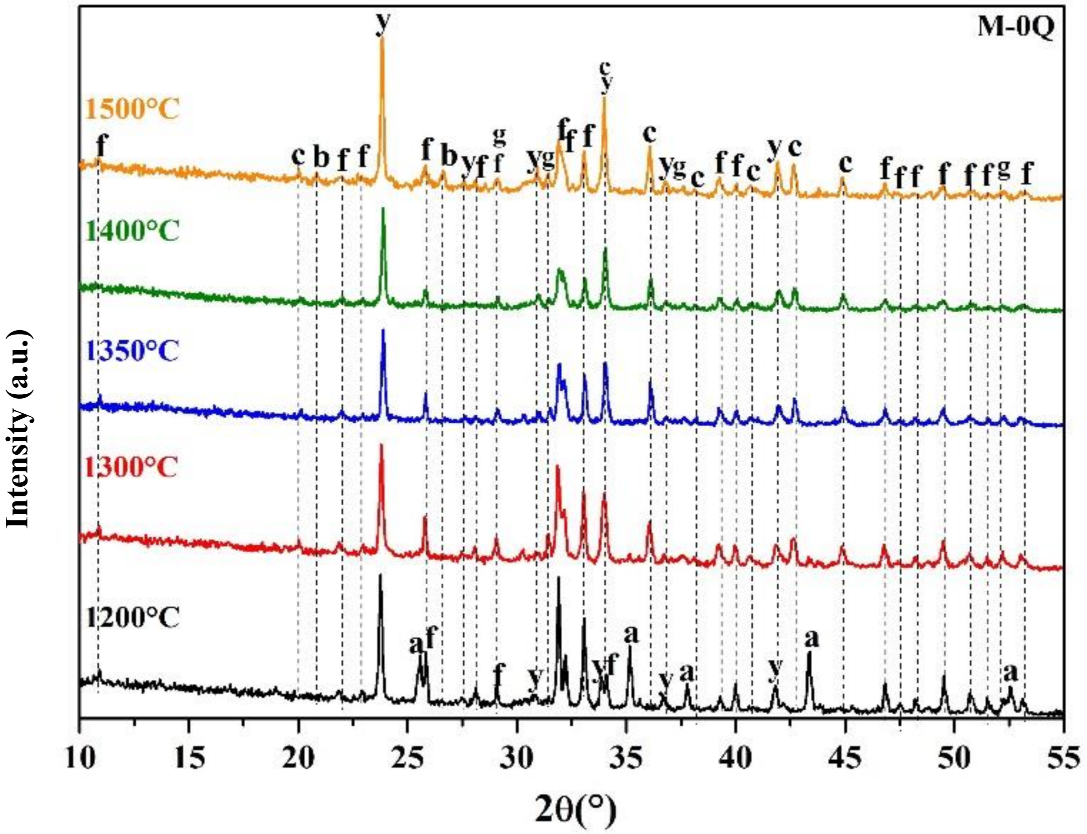
M-0Q
1500°C
1400°C
1350°C
1300°C
1200°C
Intensity (a.u.)
2θ(°)
10
15
20
25
30
35
40
45
50
55
y
c
f
b
g
a

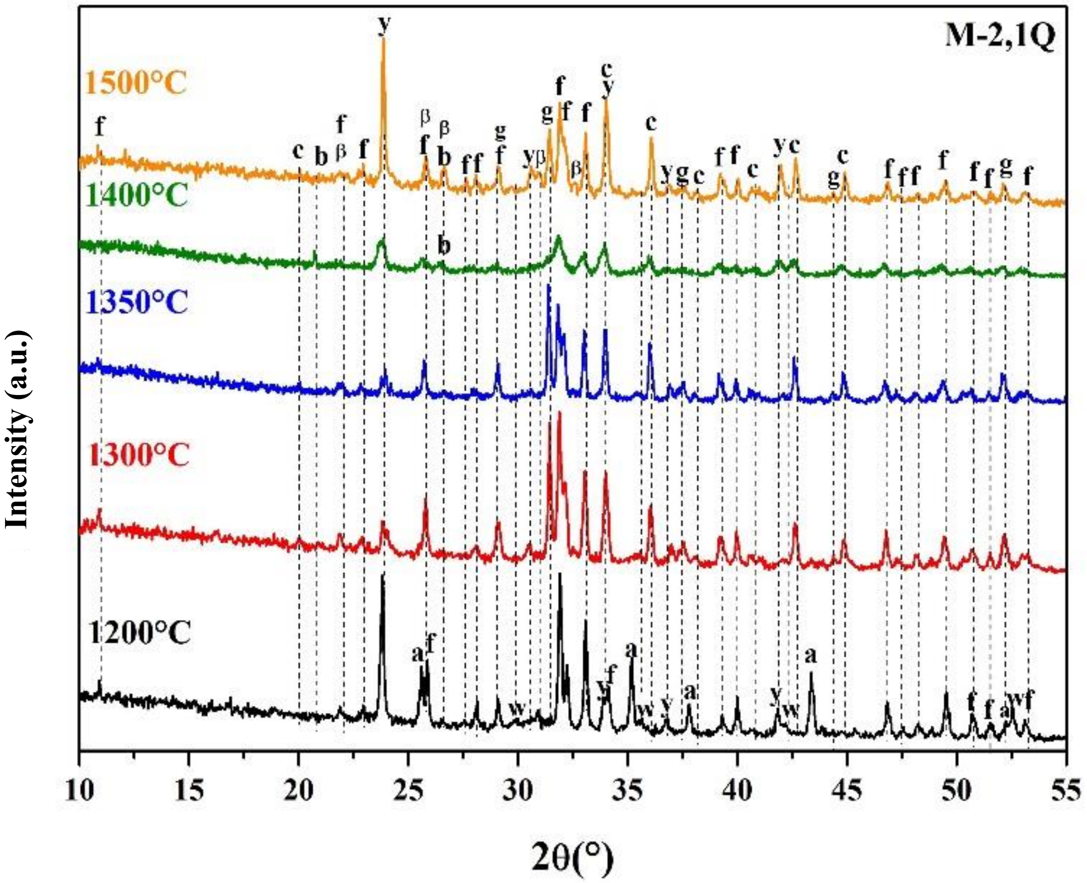
M-2,1Q
1500°C
1400°C
1350°C
1300°C
1200°C
Intensity (a.u.)
2θ(°)
10
15
20
25
30
35
40
45
50
55
y
c
f
b
β
g
a
w

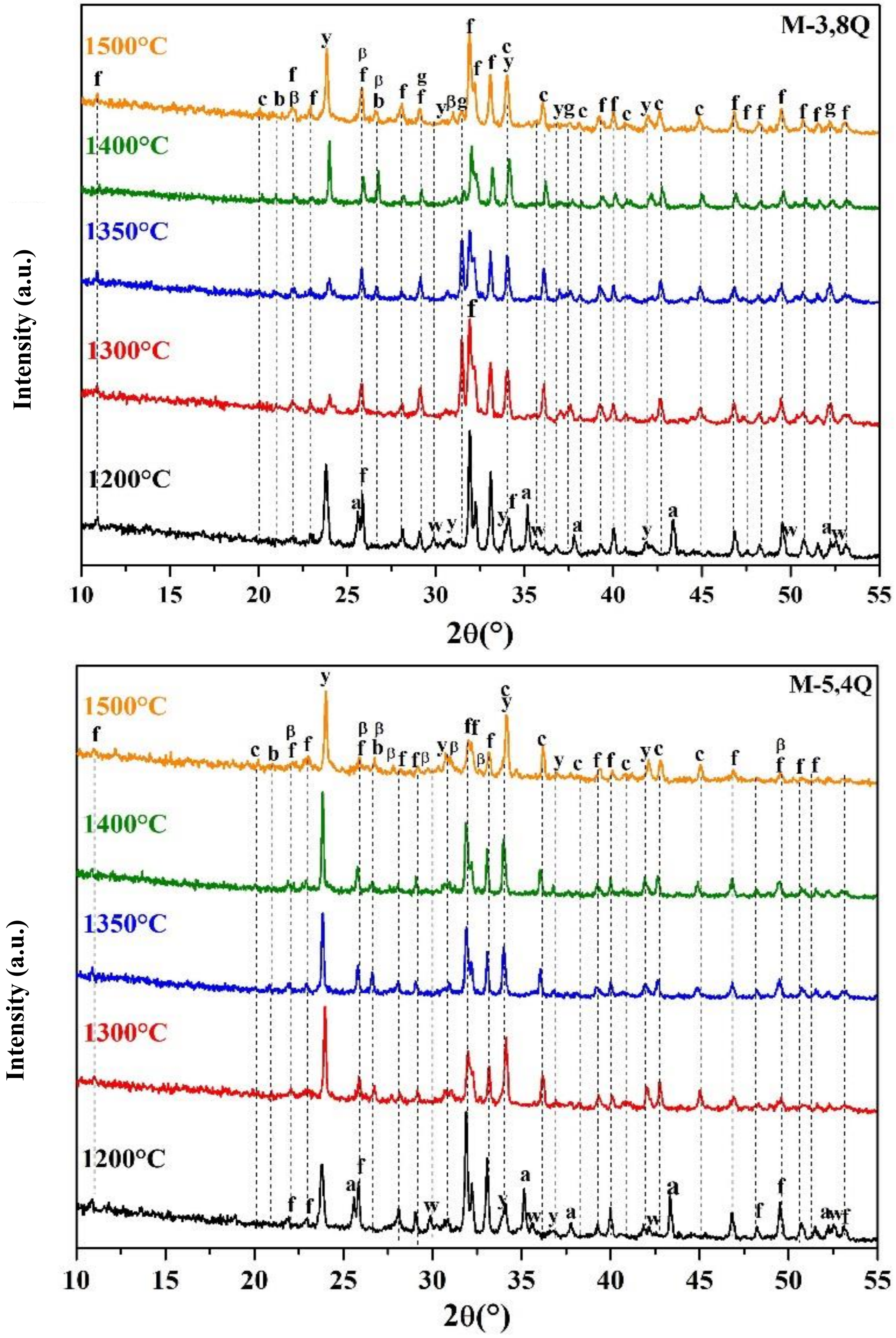

Fig.III.5. XRD analysis of sintered samples at different temperatures: a: alumina f: fluorapatite, c: calcium hexaluminate, y: ye'elimite, g: gehlenite, b: berlinite, β: β-TCP and w: wollastonite.

The notable reduction in the intensity of diffraction peaks corresponding to the ye'elimite phase in the M-2.1Q and M-3.8Q samples at 1300–1350 °C is attributed to the interaction between the SiO_2 and Al_2O_3 ratios, which influences the initial decomposition temperature of $CaSO_4$. This ratio significantly impacts the desulfurization process. The reaction between quartz and ye'elimite during sintering resulted in the formation of intermediate phases or solid solutions [40]. These phases alter the nucleation and growth behavior of ye'elimite crystals by modifying the chemical composition and diffusion pathways within the material.

The competition between gehlenite ($Ca_2Al_2SiO_7$, CA_2S) and ye'elimite is determined by the availability of aluminum (Al) and calcium (Ca) ions, as both phases depend on these ions for their formation. In mixtures with a high quartz content, quartz can consume these ions, reducing their availability for ye'elimite formation and potentially promoting the development of other phases [125,127]. During sintering at 1300–1350 °C, gehlenite competes with ye'elimite for Al and Ca ions, limiting their availability and leading to a reduced concentration of ye'elimite in the final product. This competition is a key factor explaining the varying observations reported in different studies [25,128,129]. The reduced availability of ions may suppress or delay ye'elimite crystallization, ultimately affecting the phase composition and microstructure of the material, as demonstrated by Eqs (7) and (8) [105].

$$2CaO + Al_2O_3 + SiO_2 \rightarrow Ca_2Al_2SiO_7 \qquad \text{(III. 7)}$$

$$4SiO_2 + 2Ca_4Al_6O_{12}(SO_4) \rightarrow 2Al_2O_3 + 4Ca_2Al_2SiO_7 + O_2\uparrow + 2SO_2\uparrow \qquad \text{(III. 8)}$$

We observed a contrasting relationship between C_2AS and $C_4A_3\$$, as illustrated in Fig.III.4. Depending on the specific reaction pathways, C_2AS can either facilitate or hinder the formation of $C_4A_3\$$. In some instances, C_2AS supports the nucleation and growth of $C_4A_3\$$ crystals by offering suitable nucleation sites or enhancing the transport of reactants. Conversely, under certain conditions, such as specific sintering temperatures and quartz ratios, C_2AS may compete with $C_4A_3\$$ for available aluminum and calcium ions, thereby inhibiting its formation [123,127,130]. Additionally, we noted the formation of calcium hexaluminate ($CaAl_{12}O_{19}$, CA_6), which emerges through a series of intermediate phases in the CaO-Al_2O_3 system. Key phases within this system, such as $CaAl_2O_4$, $CaAl_4O_7$, and $CaAl_{12}O_{19}$, were observed in all samples due to interactions between Al_2O_3 and CaO [29]:

$$CaO + Al_2O_3\ (s) \rightarrow CaAl_2O_4 \qquad \text{(III. 9)}$$

$$CaAl_2O_4 + Al_2O_3\ (s) \rightarrow CaAl_4O_7 \qquad \text{(III. 10)}$$

$$CaAl_4O_7 + 4\ Al_2O_3 \rightarrow CaAl_{12}O_{19} \qquad \text{(III. 11)}$$

Reactions between Al_2O_3 and $Ca_4Al_6O_{12}(SO_4)$ can also occur, leading to the formation of calcium hexaluminate ($CaAl_{12}O_{19}$) [7]:

$$21Al_2O_3 + Ca_4Al_6O_{12}(SO_4) \rightarrow 4CaAl_{12}O_{19} + SO_3 \qquad \text{(III. 12)}$$

When the sintering temperature increased to 1400–1500 °C, the ye'elimite phase peaks became more distinct. This sharpening was attributed to the dissociation of the fluorapatite phase, influenced by the availability of free CaO and P_2O_5. Additionally, part of the dissociated fluorapatite converted into beta-tricalcium phosphate (β-TCP) and contributed to the formation of berlinite ($AlPO_4$) phases [106]:

$$Ca_{10}(PO_4)_6F_2 + 3Al_2O_3 \rightarrow 6AlPO_4 + 9CaO + CaF_2 \qquad \text{(III. 13)}$$

$$P_2O_5 + Al_2O_3 \rightarrow 2AlPO_4 \qquad \text{(III. 14)}$$

The possible reactions associated with the dissociation of fluorapatite are outlined as follows [107]:

$$Ca_{10}(PO_4)_6F_2 \rightarrow 3Ca_3(PO_4)_2 + CaF_2 \qquad \text{(III. 15)}$$

$$Ca_{10}(PO_4)_6F_2 + H_2O \rightarrow 3Ca_3(PO_4)_2 + Ca_4(PO_4)_2O + 2HF \qquad \text{(III. 16)}$$

$$3Ca_{10}(PO_4)_6F_2 \rightarrow 2Ca_3(PO_4)_2 + 6Ca_4(PO_4)_2O + 2\,POF_3 \qquad \text{(III. 17)}$$

III.4.2. FTIR analysis of samples after sintering

Fig.III.6 presents the FT-IR spectra of samples sintered at different temperatures. Regardless of the quartz content, absorption peaks at 1093 and 1036 cm^{-1} were consistently observed, corresponding to the asymmetric stretching vibration (v_3) mode of the PO_4^{3-} group in fluorapatite [133,134]. Additionally, peaks at 602 and 562 cm^{-1} were attributed to the bending vibration modes (v_4) of PO_4^{3-} [135-137], while the symmetric stretching vibration (v_1) of PO_4^{3-} appeared at 960 cm^{-1} [60]. The intensity of the v_3 peaks decreased as quartz content and sintering temperature increased, aligning with XRD results that indicate the partial decomposition of fluorapatite, as evidenced by reactions (14), (15), and (16) [66,68,133,138,139].

Furthermore, peaks associated with Al-O bonds at 640 cm^{-1} [110], Ca-O-Al or Al-O-Al groups at 840, 890, and 919 cm^{-1} [140,141], and Si-O-Al or Si-O-Si groups at 491, 698, 767, and 1147 cm^{-1} [112] were identified. These observations align with XRD detection of alumina, calcium aluminate compounds, and silicate phases such as gehlenite. In samples M-2.1Q and M-3.8Q sintered at 1200 °C, symmetric Si-O-Si stretching modes of the SiO_4 tetrahedron were detected around 804 cm^{-1}, suggesting the formation of calcium silicate phases such as wollastonite, as confirmed by XRD [113].

Both analyses revealed structural and compositional changes influenced by increased sintering temperature and quartz content. FT-IR analysis provided detailed information on chemical bonds and functional groups, complementing the crystalline phase identification from XRD.

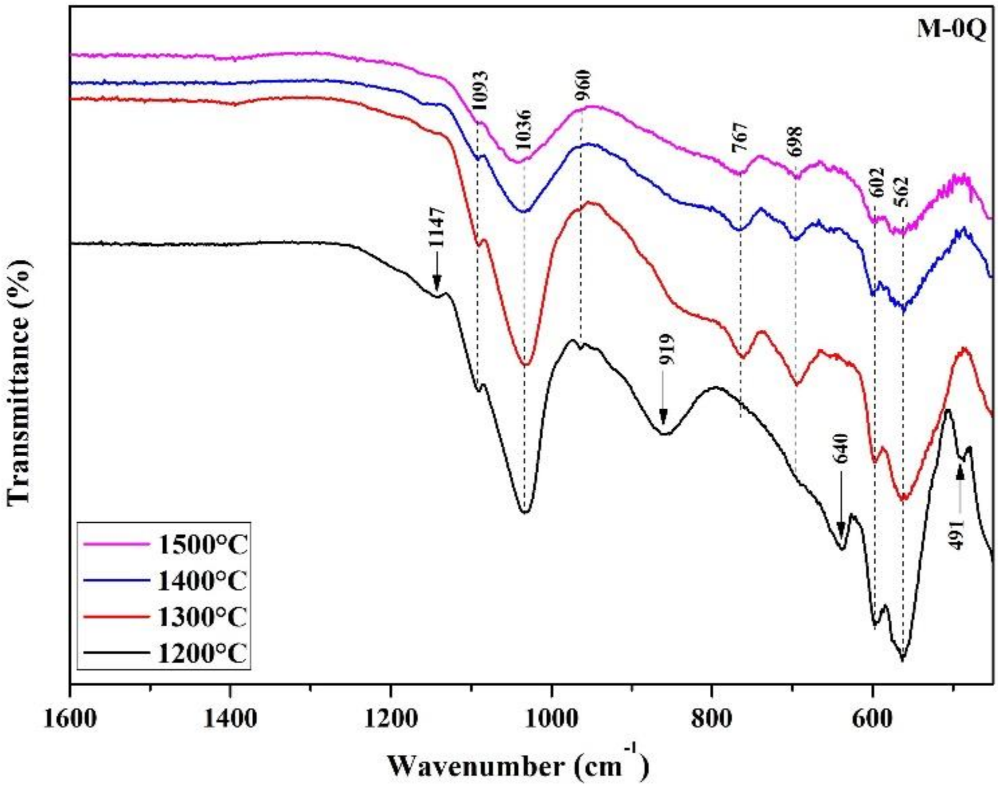

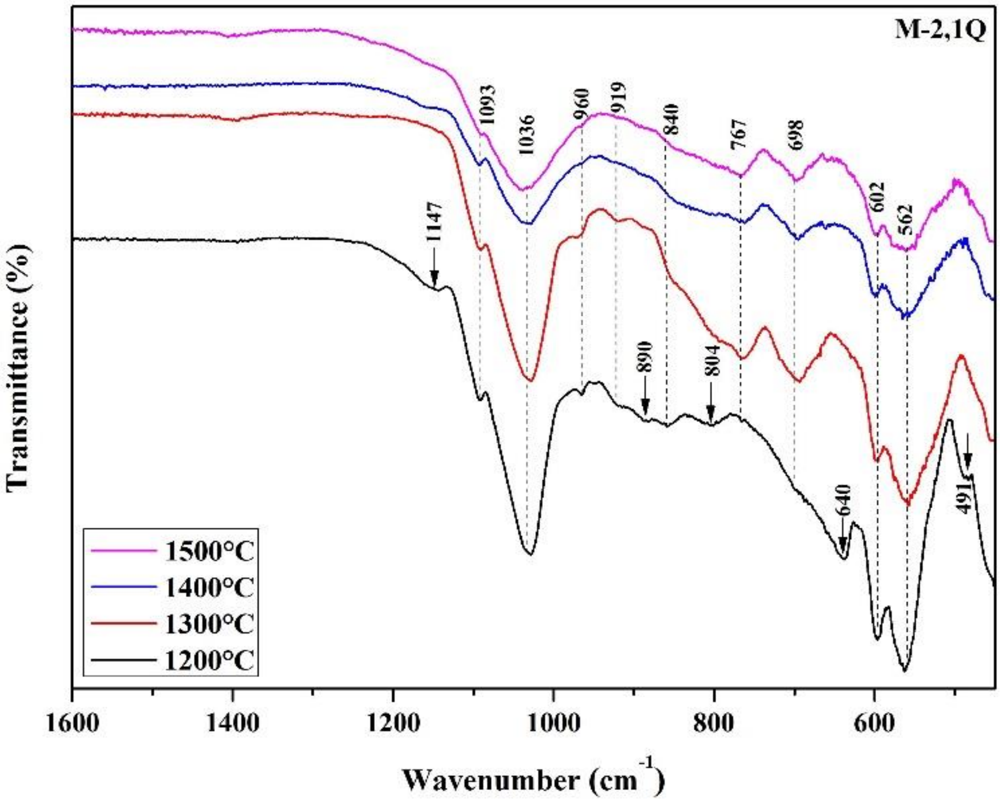

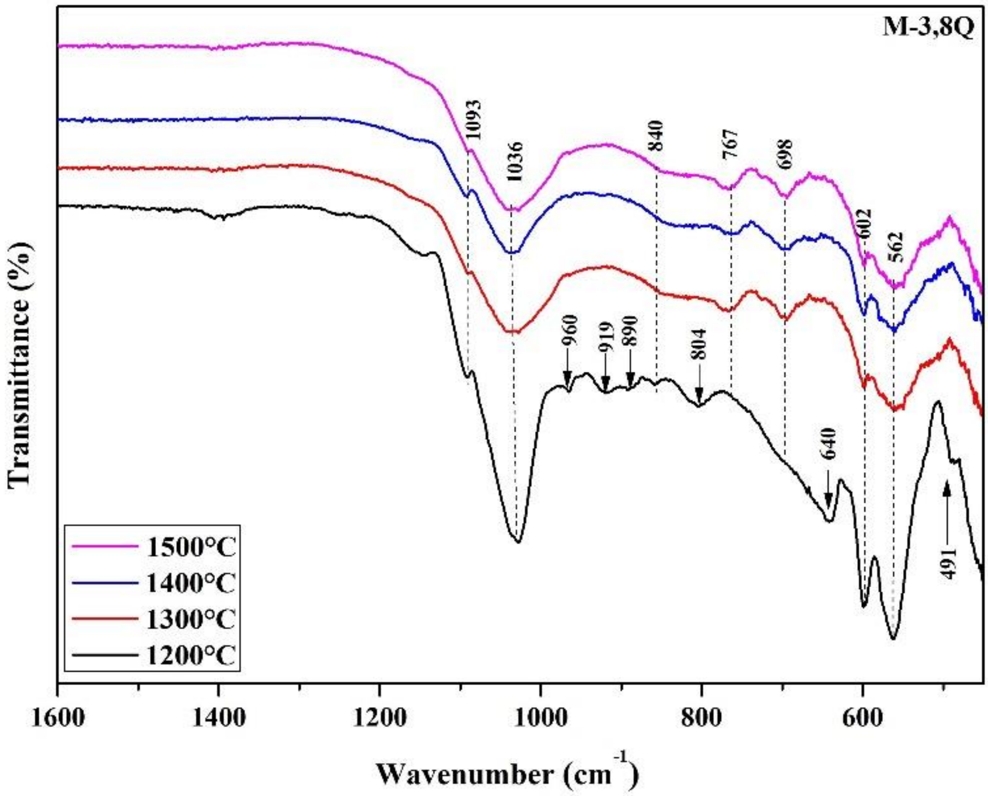

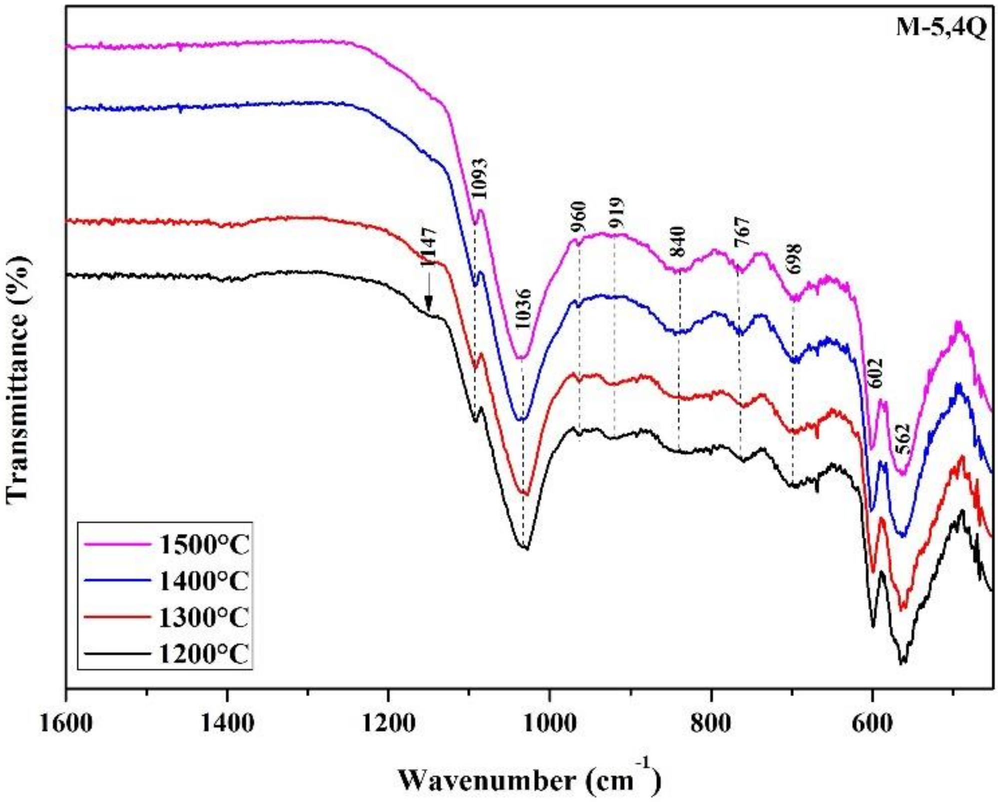

Fig.III.6. FT-IR spectrum of sintered samples sintered at various temperatures.

III.4.3. Quantitative phase analysis of the sintered samples performed using the Rietveld refinement method.

The data represents quantitative phase analysis results obtained using the Rietveld refinement method with Profex software, as illustrated in Fig.III.7 [111,112]. This quantitative analysis complements the qualitative observations, providing a robust validation and deeper understanding of the complex phase transformations that occurring during sintering at different temperatures and quartz contents.

At 1200 °C, the primary phases identified are fluorapatite (43.94–51.01 wt%), alumina (22.25–34.16 wt%), and ye'elimite (15.66–21.9 wt%), with wollastonite detected exclusively in quartz-containing samples (2.1, 3.8, and 5.4 wt% SiO_2), consistent with the reaction described in Eq (III. 6). At 1300–1350 °C, a significant reduction in ye'elimite content (to 0.36–2.85 wt%) and a corresponding increase in gehlenite content (up to 19.83–20.44 wt%) are observed in quartz-rich samples, as shown in Fig.III.7-b and Fig.III.7-c. This aligns with the XRD findings, demonstrating competition between these phases for Al and Ca ions [115]. The inverse relationship between ye'elimite and gehlenite contents corroborates the reactions in Eq (III.8) and (III.9) [29]. Additionally, the formation of calcium hexaluminate (34–41.06 wt%) throughout this temperature range supports the XRD identification of CaO-Al_2O_3 system phases, consistent with the reactions in Eqs (9-11) [128,145].

At 1400–1500 °C, quantitative data confirm the XRD results, highlighting sharper ye'elimite peaks (increasing to 13.51–28.63 wt%), fluorapatite dissociation (decreasing to 22.1 wt% at 1500 °C, as shown in Fig.III.7-d), and the formation of β-TCP and berlinite (0–6.01 wt%) [53,66,146]. The complete decomposition of gehlenite at 1500 °C, as shown in Fig.III.7-d, along with increases in ye'elimite (16.83 wt%) and calcium hexaluminate (34.19 wt%), further confirms the XRD observations of phase transformations at elevated temperatures [118]. These findings highlight the significant influence of quartz content and temperature on phase formation and stability, particularly for ye'elimite and gehlenite, which play a crucial role in determining the material's properties and performance [126,148].

The quantitative analysis underscores the importance of maintaining specific Al_2O_3 and SiO_2 ratios (2–4 wt% SiO_2) and sintering temperatures (1300–1350 °C) to optimize ye'elimite content. Excessive formation of gehlenite can adversely affect hydraulic activity and overall performance, as noted in prior studies [123,130].

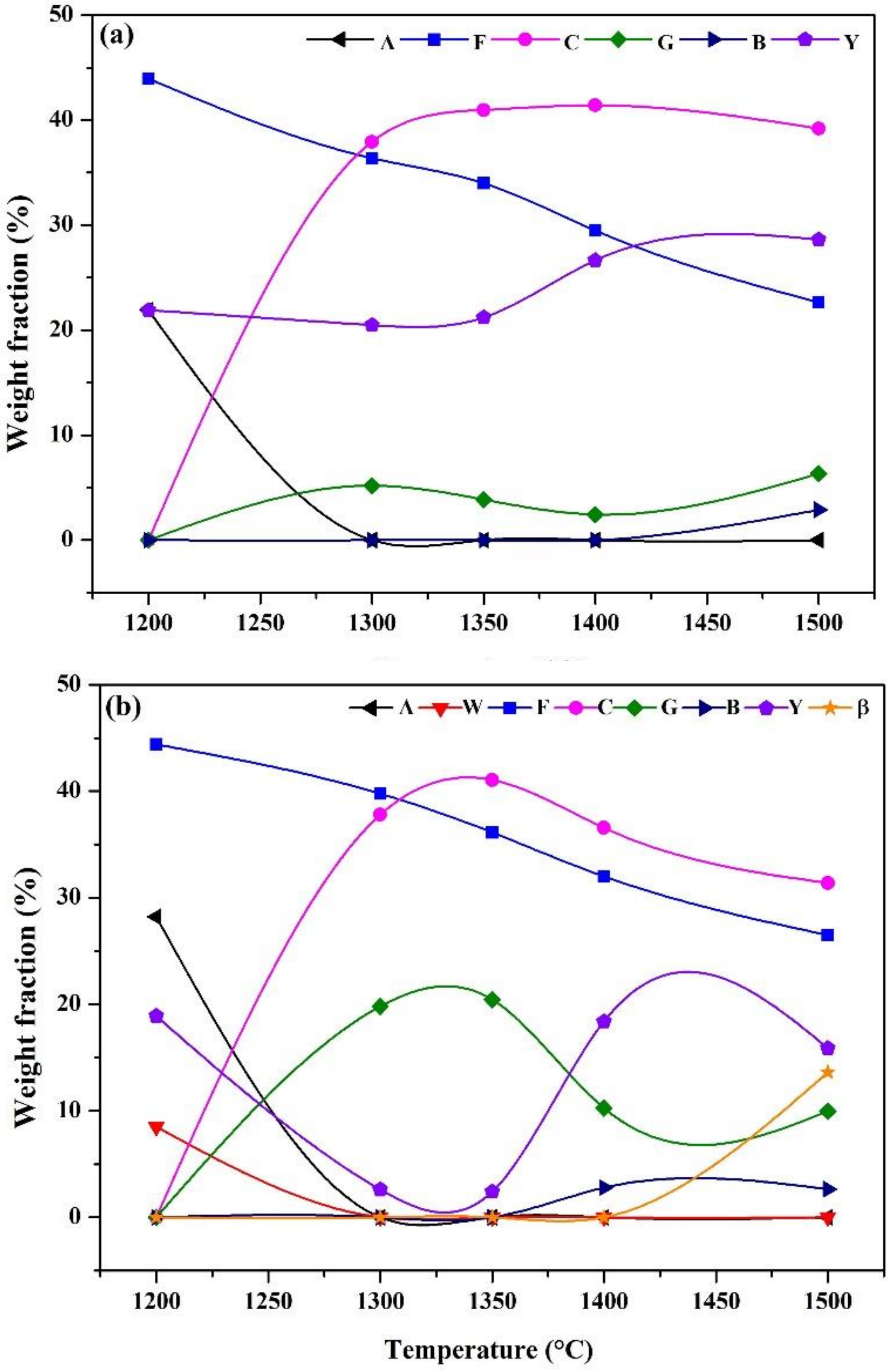
(a)
A
F
C
G
B
Y
Weight fraction (%)
50
40
30
20
10
0
1200
1250
1300
1350
1400
1450
1500
(b)
A
W
F
C
G
B
Y
β
Weight fraction (%)
50
40
30
20
10
0
1200
1250
1300
1350
1400
1450
1500
Temperature (°C)

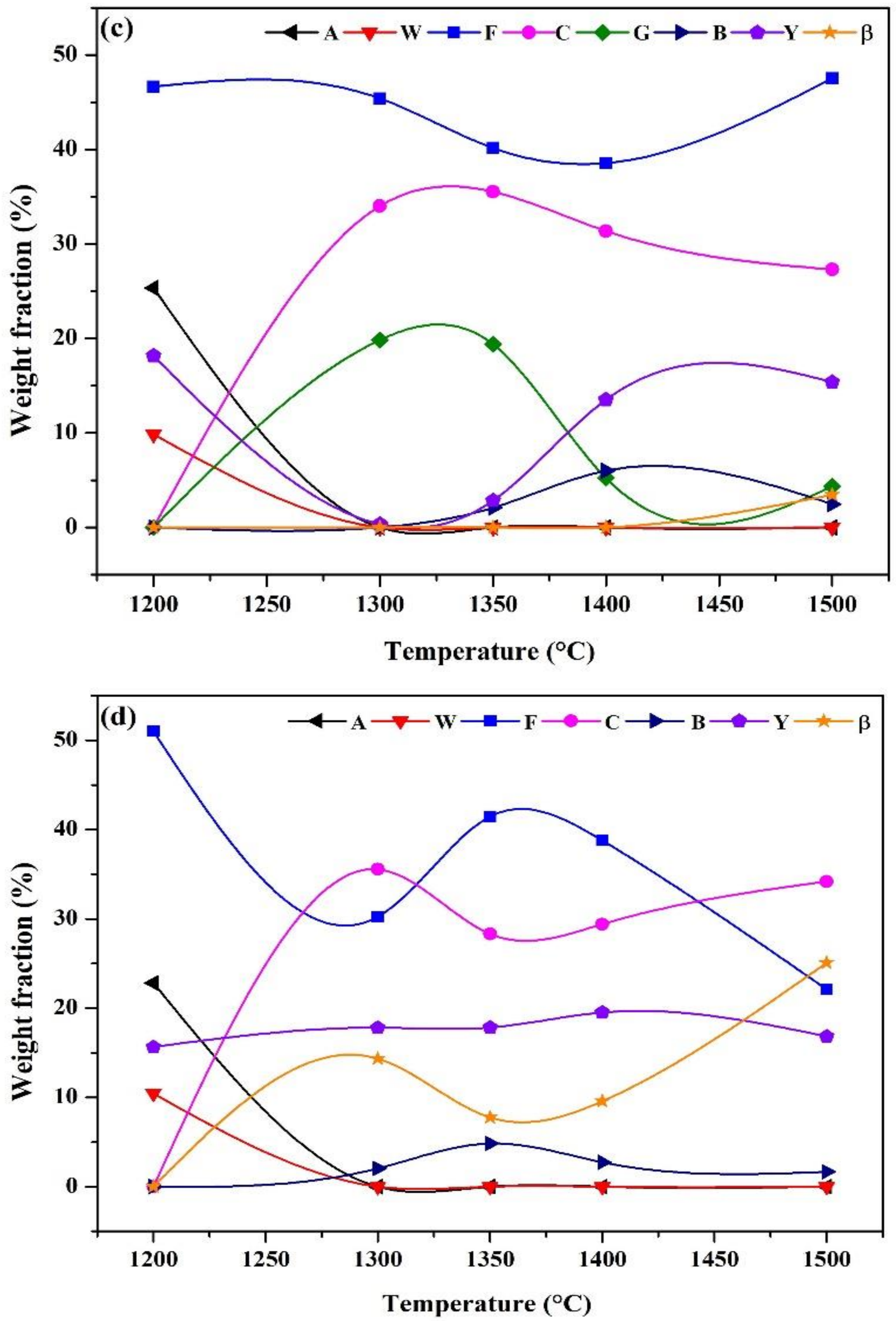

Fig.III.7. Weight fraction of phases content as a function of quartz addition and sintering temperature: (a): M-0Q, (b): M-2.1Q, (c): M-3.8Q and (d): M-5.4Q (A: alumina, F: fluorapatite, C: calcium hexaluminate, Y: ye'elimite, (G): gehlenite, B: berlinite, β: β-TCP, W: wollastonite).

Table III. 2: Index of Rietveld refinements for samples sintered at different temperatures.

M-0Q	**1200°C**	**1300°C**	**1350°C**	**1400°C**	**1500°C**
Rwp	9.91	9.83	14.4	13.49	9.62
Rexp	8.86	8.92	12.36	12.13	8.72
GoF	1.12	1.1	1.16	1.11	1.1
M-2.1Q	1200°C	1300°C	1350°C	1400°C	1500°C
Rwp	9.97	9.81	13.72	14.56	8.86
Rexp	9.08	9.09	12.01	12.99	8.94
GoF	1.09	1.07	1.14	1.12	0.99
M-3.8Q	**1200°C**	**1300°C**	**1350°C**	**1400°C**	**1500°C**
Rwp	10.33	9.74	13.86	14.12	9.81
Rexp	9.05	9.15	12.08	12.45	9.15
GoF	1.14	1.06	1.14	1.14	1.07
M-5.4Q	**1200°C**	**1300°C**	**1350°C**	**1400°C**	**1500°C**
Rwp	10.64	9.35	13.44	13.19	9.35
Rexp	9.08	9.2	11.96	11.92	9.21
GoF	1.17	1.01	1.12	1.1	1.01

III.4.4. Evaluating the impact of porosity on sintered sample properties

The variations in open porosity and bulk density of the samples with sintering temperature were evaluated using Archimedes' principle, with the results presented in Fig.III.8. Generally, as the sintering temperature increased to 1400 °C, the bulk density of the samples increased, while open porosity decreased across all samples. For samples M-0Q, M-2.1Q, and M-3.8Q, the bulk density remained relatively stable between 1200 and 1300 °C. However, for sample M-5.4Q, a linear increase in bulk density was observed, reaching 2.85 ± 0.11 g/cm³ at 1300 °C (Fig.III 8-a). A significant rise in bulk density was noted between 1300 and 1400 °C for all samples. At 1400 °C, the bulk densities ranged from 1.65 to 2.8 g/cm³ for samples M-0Q, M-2.1Q, M-3.8Q, and M-5.4Q.

The density increase is due to the formation of calcium hexaluminate and gehlenite phases, which have relatively high theoretical densities of 3.79 g/cm³ and 2.98 g/cm³, respectively [119,120], as supported by the XRD results [116]. However, the reduced bulk density of 2.62 g/cm³ for sample M-5.4Q at 1500 °C is likely due to the combined effects of increased trapped pores (resulting from gas evolution during sintering) and thermal expansion, both of which are influenced by the higher quartz content at this temperature [7].

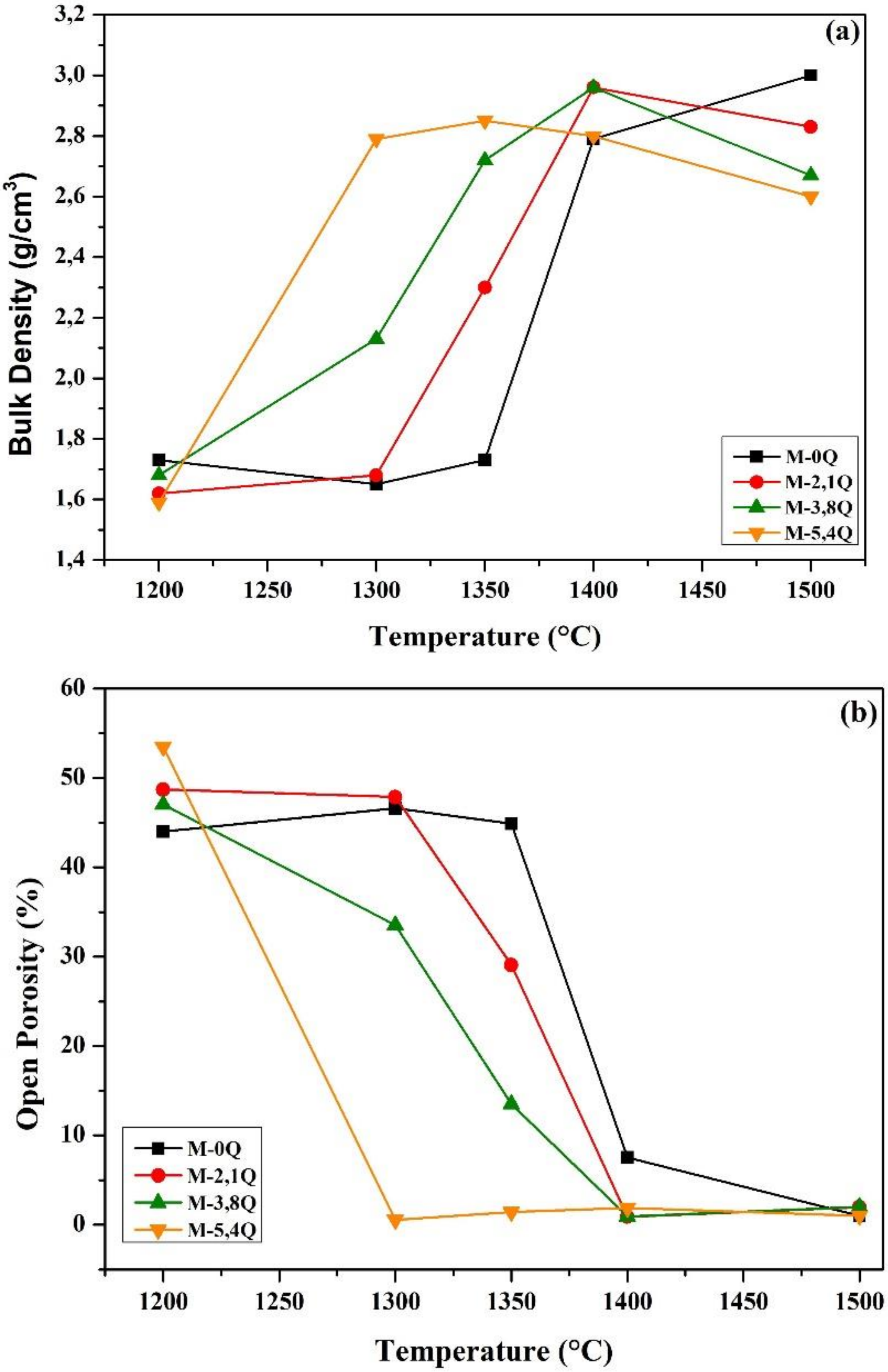

Fig.III.8. Effect of sintering temperatures on the (a) bulk density and (b) open porosity of heated samples.

Open porosity is a crucial parameter in the cement industry, as it allows for easier grinding of clinker into cement for manufacturers. Within the temperature range from 1200 to

1300 °C, the open porosity remained relatively constant, ranging from 33.5% to 48.7%, except for sample M-5.4Q (Fig.III.8-b). For M-5.4Q, a linear decrease in open porosity was observed, dropping from 53.5% to 0.5%. At higher temperatures (1300-1400 °C), there was a gradual and consistent decline in open porosity values was observed. Above 1400 °C, the open porosity remained relatively stable, maintaining near-constant values within the 1400 to 1500 °C range.

Vickers hardness measurements were performed on the dense samples sintered at 1400 °C, as shown in Table (III. 3). Despite the addition of quartz, the hardness values ranged from 3.54 to 6.13 GPa, indicating no clear correlation between the hardness of the samples and their density [121].

Table III. 3: The bulk density and Vickers hardness of samples sintered at 1400 °C.

Samples	**M-0Q**	**M-2.1Q**	**M-3.8Q**	**M-5.4Q**
Bulk density (g/cm^3)	2.79±0.11	2.96±0.12	2.96 ± 0.12	2.66 ±0.10
Vickers Hardness (GPa)	3.54±0.14	5.63±0.22	5.78±0.23	6.13±0.24

III.4.5. Microstructural analysis of sintered samples.

Fig.III.9 presents SEM micrographs of the multi-phase composite samples, illustrating the microstructural evolution of samples sintered at 1400 °C for 2 hours. Distinct microstructural changes were observed with increasing quartz content, consistent with the quantitative phase analysis and XRD results.

In Fig.III.9-a, the microstructure shows a dense arrangement of small, rounded particles, likely representing ye'elimite grains [117]. In Fig.III.9-b, the structure becomes more porous, featuring larger, irregular particles indicative of the onset of liquid phase formation [7]. Fig.III.9-c and 9-d depict a significant transformation, with the emergence of prominent hexagonal sheet-like structures characteristic of calcium hexaluminate crystals. This change aligns with the effects of increasing quartz content and elevated sintering temperatures [122]. Notably, the hexagonal sheet-like structures in Fig.III.9-d appear more defined and thicker compared to those in Fig.III.9-c, corresponding to the high calcium hexaluminate content (34–41.06 wt%) detected in the XRD data at this temperature [66,152].

The detailed correlation between SEM observations and XRD results at 1400 °C highlights the intricate relationships between composition, phase evolution, and microstructural development in this complex ceramic system. It underscores how sintering conditions and quartz content at this specific temperature influence the final material properties [123].

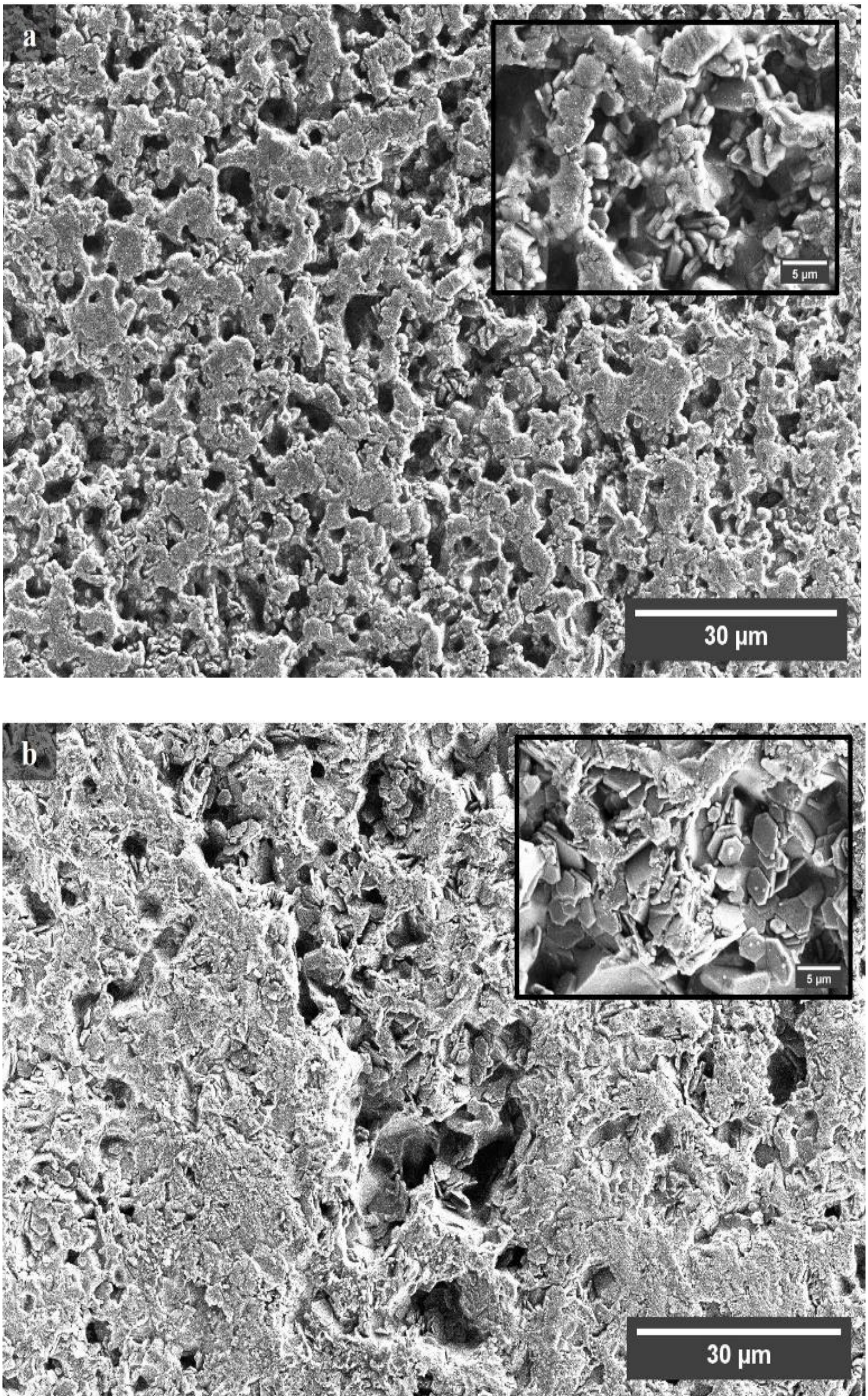

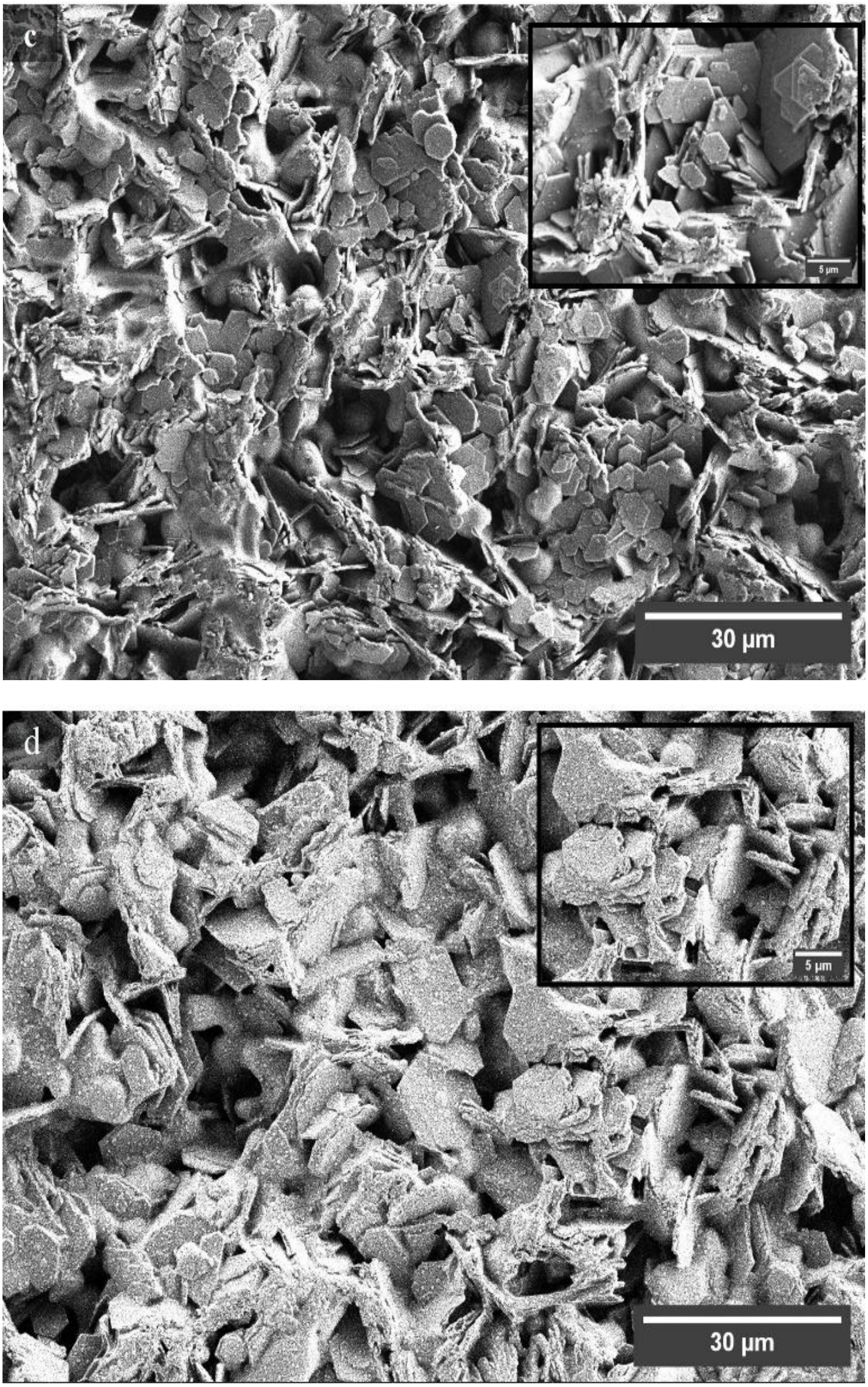

Fig.III.9. SEM micrographs of fracture surface of sample: (a): M-0Q, (b): M-2.1Q, (c): M-3.8Q and (d): M-5.4Q sintered at 1400 °C.

Part 02: *The influence of magnesium oxide on natural fluorapatite decomposition during the preparation of spinel-ye'elimite based multi-phase composites.*

In the following section part of the chapter, we investigate the effect of incorporating magnesium oxide (MgO) on the sintering characteristics of ye'elimite composites synthesized using natural phosphate as a raw material. This study focuses on understanding MgO's role throughout the sintering process, particularly its influence on material densification, phase's development, and structural transformations occurring during heat treatment. Through detailed analysis of these parameters, we aim to elucidate the fundamental mechanisms by which MgO functions as an additive and comprehend its effects on the final properties of the ye'elimite composite. The findings presented in this research enhance our knowledge of sintering dynamics and may contribute to future improvements in the manufacturing process of these phosphate-derived composites.

III.1. Physicochemical analysis of milled powders after calcination

XRD analysis was performed on the powder samples after the calcination process, with the resulting diffraction patterns displayed in Fig.III.10. Upon examination, all powder samples exhibited remarkably consistent phase compositions, retaining the characteristic phases inherent of their starting raw materials.

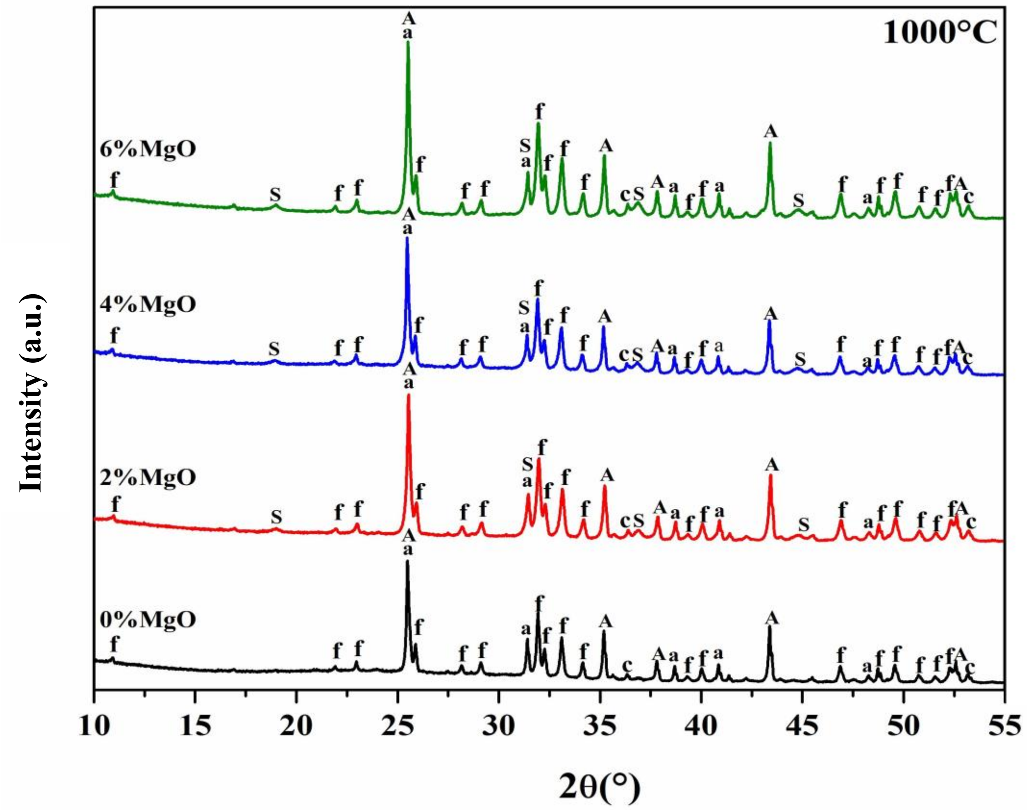

Fig.III.10. XRD analysis of the powder mixture calcined at 1000 °C, revealing the presence of the following phases: alumina (A), fluorapatite (f), spinel (S), CaO (c), and anhydrite (a).

These phases were systematically identified and documented in Table (III. 4). To further validate the phase composition, XRF spectroscopy was conducted specifically on the samples calcined at 1000 °C, providing quantitative chemical composition data. A particularly significant observation from this analysis is that, despite the intensive mechanical forces applied during the grinding process, the composite powders maintained their original phase integrity. This indicates that mechanical processing did not induce any phase transformations or chemical alterations in the material structure. The preservation of the initial phases throughout the grinding suggests that the material system remains stable under mechanical stress conditions.

Table III. 4: Chemical composition (wt%) of the calcined powders at 1000 °C.

Samples name	SiO_2	Al_2O_3	Fe_2O_3	CaO	MgO	SO_3	K_2O	Na_2O	P_2O_5	TiO_2
0%MgO	3.28	36.43	0.70	29.43	0.93	11.24	0.27	0.45	8.87	1.84
2%MgO	3.17	35.8	0.68	28.80	2.76	10.97	0.24	0.42	8.70	1.81
4%MgO	3.12	34.89	0.64	28.34	4.81	11.23	0.21	0.38	8.54	1.80
6%MgO	3.04	33.28	0.60	27.74	7.31	11.16	0.21	0.37	8.34	1.76

III.2. TGA and DTG analysis of mixtures

The thermal characteristics of the samples during sintering were examined using TGA and DTG analysis, with the results shown in Fig.III.11. The data indicated that thermal decomposition occurred in four separate phases, providing detailed insights into the step-by-step decomposition process during heating. Each phase corresponds to specific chemical changes in various components:

The first two endothermic peaks in steps 1 and 2, between 100-350 °C, accompanied with a weight loss of 2.85% (H_2O). This weight loss is due to the partial dehydration of gypsum, as described by reaction (III. 1) [119,120]. Further heating of 200 to 400 °C in step 2 leads to the formation of soluble anhydrite ($CaSO_4$ anhydrous phase I), which is metastable and can easily rehydrate, as following by reaction (III. 2) [124]:

$$CaSO_4.2H_2O \rightarrow CaSO_4.1/2\ H_2O + 3/2\ H_2O\uparrow \qquad (III.\ 1)$$

$$CaCO_4.1/2H_2O \rightarrow CaSO_4 + 1/2\ H_2O\uparrow \qquad (III.\ 2)$$

The third stage, occurring around 740 °C, showed an endothermic peak accompanied by a 2.43% weight loss. This phenomenon is attributed to francolite decarbonation, where carbonate (CO_3^{2}) groups are expelled from the crystal structure, as described in reaction (III. 18) and supported by [125]:

$Ca_5(PO_4)_3(CO_3)_3\,F \rightarrow Ca_5(PO_4)_3F + 3CO_2\uparrow + 3/2\ O_2\uparrow$ (III. 18)

The final thermal event (step 4) occurred between 940–1200 °C, during which multiple endothermic peaks were observed. This stage was marked by significant gas release and a substantial weight loss of approximately 9.02%. The mass reduction in this temperature range is attributed to the decomposition of residual calcium sulfate ($CaSO_4$), accompanied by the release of large amounts of sulfur dioxide and oxygen gases during the heating process, as described by reaction (III. 3) as noted in [102]:

$CaSO_4 \rightarrow CaO + 1/2\ O_2\uparrow + SO_2\uparrow$ (III. 3)

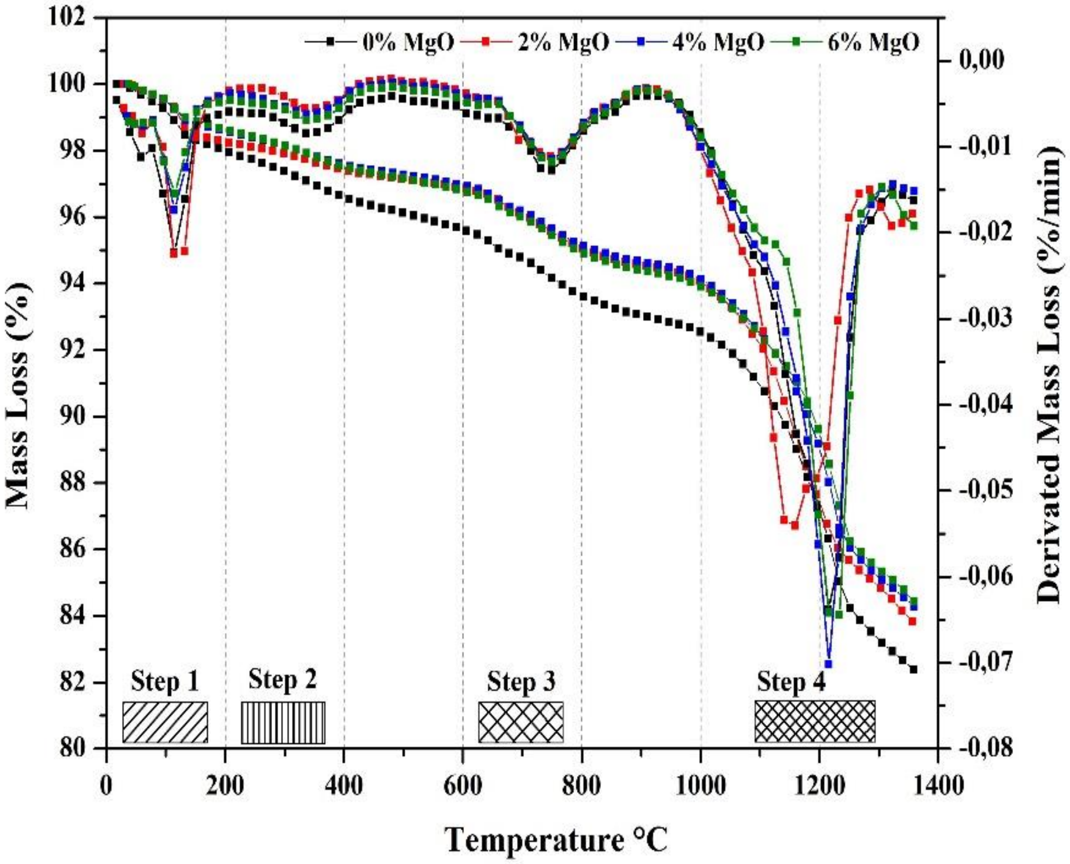

Fig.III.11. TG and DTG curves of the raw mixture during the heating process.

III.3. Analysis of shaped and sintered samples

III.3.1. X-ray analysis of samples after sintering

The XRD patterns in Fig.III.12 reveal multiple phase transformations in the ceramic system, potentially relevant to specialized cements [84,155,156] or refractories [157,158]. These transformations are influenced by temperature variations (1100 °C to 1500 °C) and MgO content (0% to 6%). At lower temperatures (1100 °C and 1200 °C), a diverse phase composition is observed, including fluorapatite, anhydrite, alpha alumina (α-Al_2O_3), and ye'elimite [4]. The ye'elimite phase is particularly evident in samples containing 0% and 2% MgO, as described by Eq (III. 5). With increasing MgO content, $MgAl_2O_4$ peaks begin to appear and intensify [127]. Conversely, the formation of the ye'elimite phase diminishes in samples containing 4% and 6% MgO, attributed to the interaction between MgO and Al_2O_3, as explained by Eq (III. 19):

$$3CaO + 3Al_2O_3 + CaSO_4 \rightarrow Ca_4Al_6O_{12}(SO_4) \qquad \text{(III. 5)}$$

$$MgO + Al_2O_3 \rightarrow MgAl_2O_4 \qquad \text{(III. 19)}$$

As the temperature increases from 1300 °C to 1400 °C, ye'elimite becomes the dominant phase across all MgO concentrations, highlighting its high thermal stability [49,160,161]. The phase assemblage simplifies significantly, with fewer but more thermodynamically stable phases emerging [47]. The influence of increasing MgO content (from 0% to 6%) is evident through the progressive growth of spinel peaks, which is particularly pronounced at 1400 °C [128]. Fluorapatite peaks persist at 1300 °C in samples with low MgO content but diminish at 1400 °C, suggesting partial decomposition or reaction [163,164]. Additionally, new diffraction peaks emerge, corresponding to the formation of grossite (CA_2, $CaAl_4O_7$) and hibonite (CA_6, $CaAl_{12}O_{19}$). Simultaneously, the intensity of peaks associated with CaO and Al_2O_3 decreases [35,36].

These changes in the diffraction patterns indicate a solid-state reaction between CaO and Al_2O_3, leading to the formation of CA_2 and CA_6, as described by chemical Eqs (III. 10) and (III.11):

$$CaO + 2Al_2O_3 \rightarrow CaAl_4O_7 \qquad \text{(III. 10)}$$

$$CaO + 2Al_2O_3 \rightarrow CaAl_{12}O_{19} \qquad \text{(III. 11)}$$

At 1500 °C, the influence of increasing MgO content (from 0% to 6%) becomes particularly pronounced as spinel peaks grow progressively stronger and, at 6% MgO, nearly rival the intensity of ye'elimite. In the 0% MgO sample, ye'elimite peaks remain prominent alongside residual phases of CA_6 and CA_2 [28][4]. Meanwhile, fluorapatite undergoes partial decomposition, forming beta-tricalcium phosphate (β-TCP, $Ca_3(PO_4)_2$). During heating, fluorapatite may release fluoride ions (F^-), triggering its transformation into β-TCP, as illustrated in Eq (III. 15) [66,68,76,165]. MgO stabilizes β-TCP formation by reducing the temperature required for fluorapatite decomposition and influencing the crystal structure and phase purity of the resulting β-TCP [166-168].

$$Ca_{10}(PO_4)_6F_2 \rightarrow 3Ca_3(PO_4)_2 + CaF_2\uparrow \qquad (III.\ 15)$$

The solid-state diffusion mechanism responsible for Al^{3+} incorporation into the fluorapatite structure occurs due to the high-temperature sintering process, which enhances ionic mobility. At elevated temperatures, the fluorapatite structure begins to decompose, increasing the availability of $Ca^{2+}$and PO_4^{3-} ions, creating lattice vacancies that facilitate the diffusion of Al^{3+} ions. The presence of alumina (Al_2O_3) in the composite serves as a thermodynamically favorable source of Al^{3+}, which can substitute for Ca^{2+} in the Fap lattice due to its similar charge and comparable ionic radius. Additionally, Al^{3+} may also interact with phosphate groups, leading to the formation of new phases such as $CaAl_4O_7$ and $CaAl_{12}O_{19}$. The driving force behind this diffusion process is the reduction in free energy associated with phase transformations and the formation of stable calcium aluminate compounds. The partial decomposition of fluorapatite in the presence of Al_2O_3 at elevated temperatures can be explained by Eqs (III. 20) and (III. 21) [66,134]:

$$Ca_{10}(PO_4)_6F_2 + 2\ Al_2O_3 + H_2O \rightarrow 3\ Ca_3(PO_4)_2 + CaAl_4O_7 + 2\ HF\uparrow \qquad (III.\ 20)$$

$$Ca_{10}(PO_4)_6F_2 + 6\ Al_2O_3 + H_2O \rightarrow 3\ Ca_3(PO_4)_2 + CaAl_{12}O_{19} + 2\ HF\uparrow \qquad (III.\ 21)$$

As the concentration of magnesium oxide increases, the system transitions predominantly toward a mixture of spinel and ye'elimite phases. During this transition, other phases, including CA_6 (calcium hexaluminate), undergo complete decomposition, particularly in samples containing 4% and 6% MgO. The X-ray diffraction patterns display distinct and well-defined peaks, suggesting that the remaining phases have high crystallinity. At the extreme temperature conditions, the impact of compositional variations becomes more pronounced, resulting in an almost binary phase system consisting of ye'elimite and spinel at the highest MgO content. These findings at 1500 °C demonstrate the crucial relationship between temperature and composition in determining the final phase distribution. This understanding provides valuable insights for optimizing the material's performance in high-temperature applications where both ye'elimite stability and spinel formation play essential roles.

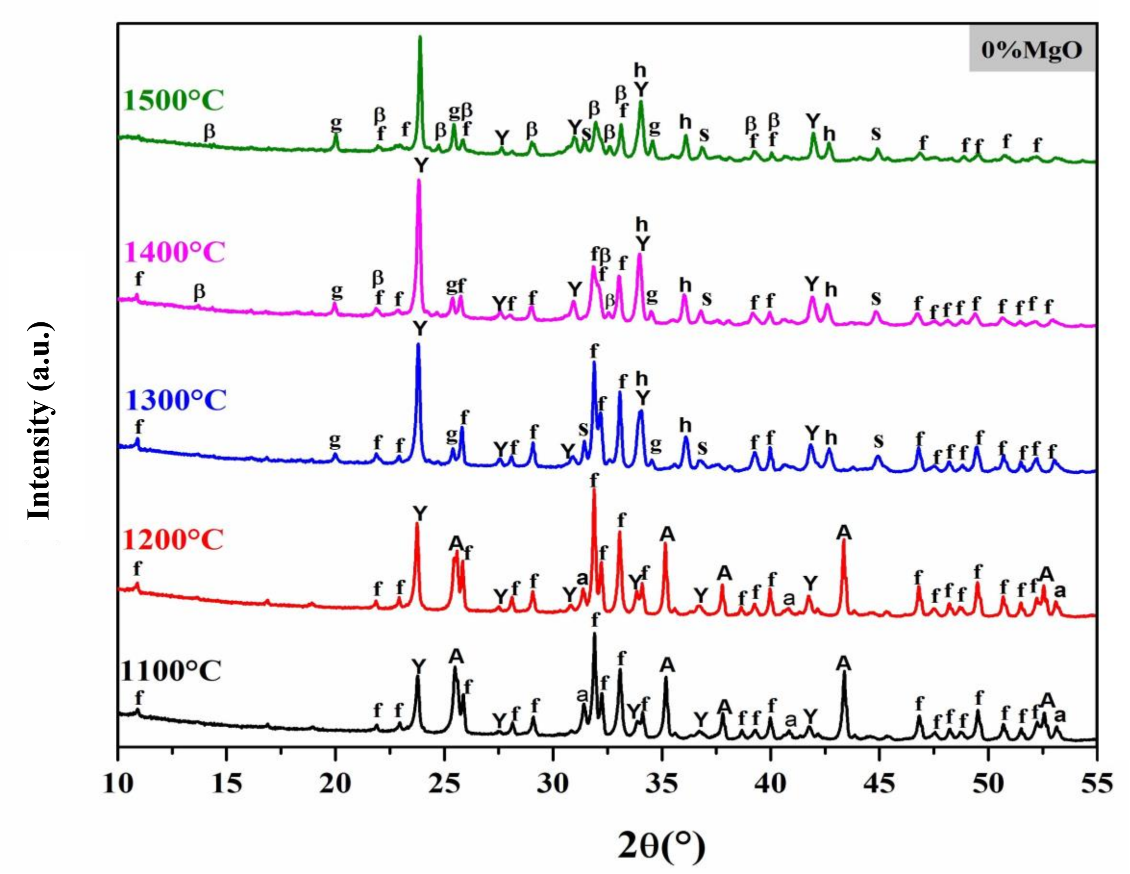
0%MgO
1500°C
1400°C
1300°C
1200°C
1100°C
Intensity (a.u.)
2θ(°)
10
15
20
25
30
35
40
45
50
55
Y
A
f
a
h
g
s
β

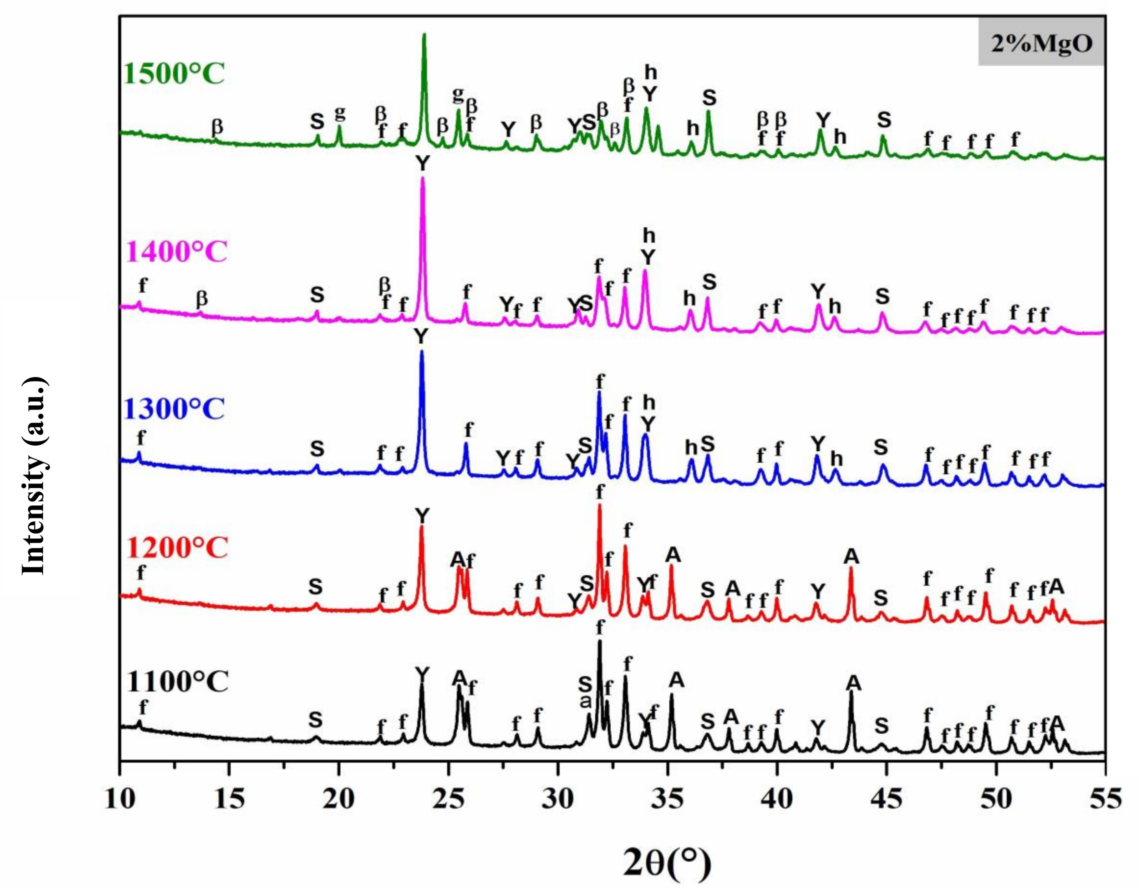
2%MgO
1500°C
1400°C
1300°C
1200°C
1100°C
Intensity (a.u.)
2θ(°)
10
15
20
25
30
35
40
45
50
55
Y
A
f
a
h
g
S
β

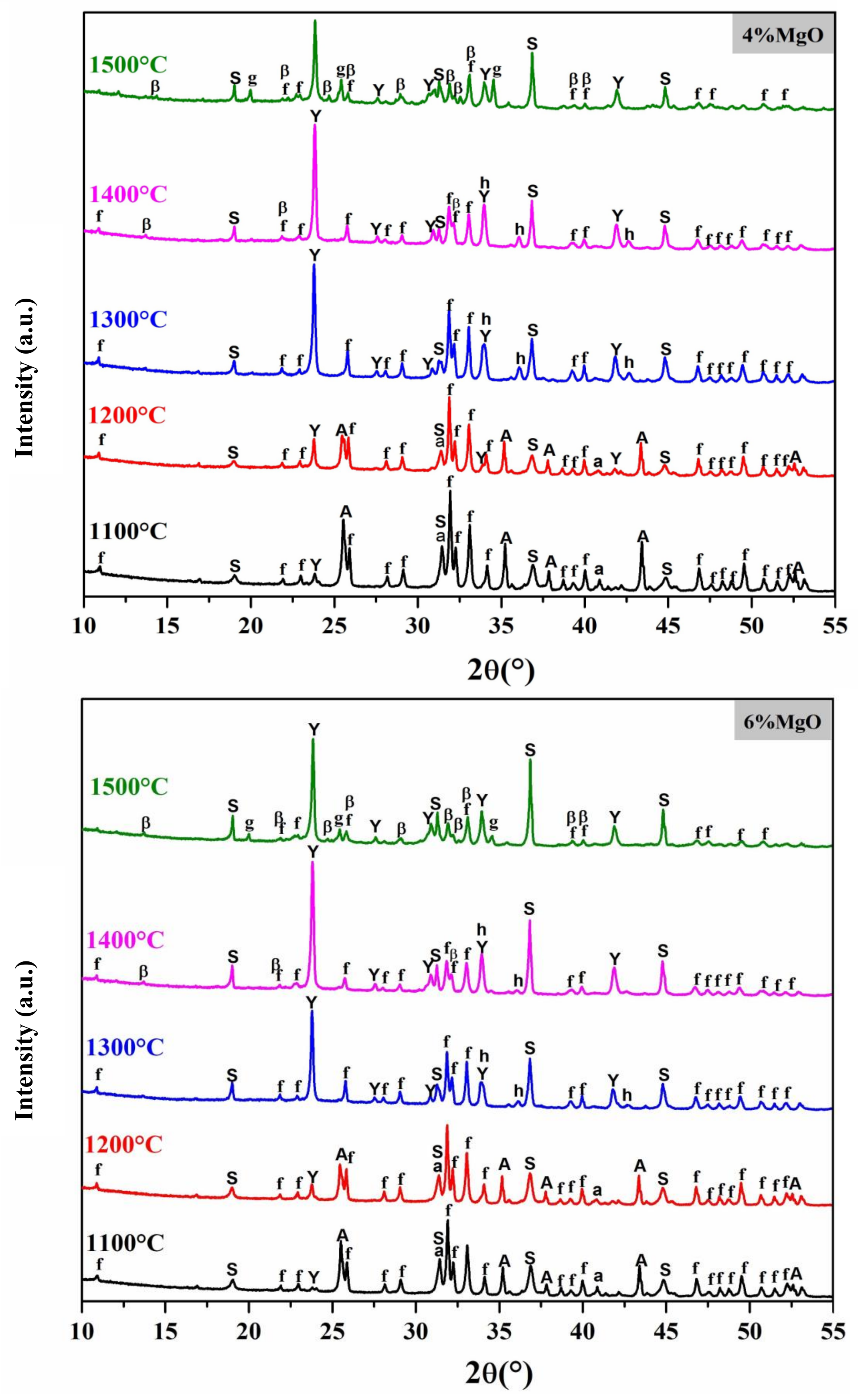

Fig.III.12. XRD analysis of samples sintered at different temperatures, showing the presence of α-Al_2O_3 (A), fluorapatite (f), anhydrite (a), ye'elimite (Y), spinel (S), grossite (g), hibonite (h) and β -TCP (β).

III.3.2. FTIR analysis of samples after sintering

The FTIR and XRD analyses provide complementary insights into the phase transformations and structural changes of the ceramic systems under varying temperature and MgO content. XRD patterns reveal multiple phases, such as fluorapatite, ye'elimite, anhydrite, α-Al_2O_3, and spinel, with their relative proportions shifting based on temperature and MgO concentration. These findings are supported by the FTIR spectra, as shown in Fig.III.13, where a characteristic absorption peak at 1039 cm^{-1} corresponds to the asymmetric vibrational mode (ν_3) of the PO_4^{3-} group in fluorapatite [7].

The intensity of the ν_3 peaks for the PO_4^{3-} group decreases with increasing MgO content and higher sintering temperatures, suggesting that MgO disrupts the fluorapatite lattice. This observation aligns with the XRD results, which indicate the decomposition of fluorapatite into alpha-TCP [133,139,169,170]. Additional peaks associated with the (ν_4) vibrational modes of PO_4^{3-} were identified between 549 and 598 cm^{-1}, while the (ν_1) vibrational mode of PO_4^{3-} appeared at 967 cm^{-1} [68,171]. The FTIR spectra also revealed S-O stretching vibrations at 652, 1095, and 1145 cm^{-1}, corresponding to sulfate-containing phases such as ye'elimite and anhydrite, as detected in the XRD analysis [172-174].

Peaks observed at 530 cm^{-1} and 690 cm^{-1} were attributed to Mg-O-Al vibrations, indicating the formation of $MgAl_2O_4$ spinel, which becomes more prominent in XRD patterns at higher MgO concentrations and temperatures [132]. Vibrational bands associated with Mg-O-Al or Ca-O-Al were also detected in the 789–900 cm^{-1} [141,176-178]. Additionally, bands at 630, 652, and 670 cm^{-1} were linked to Al-O stretching vibrations in tetrahedral structures (AlO_4), while bands at 669 and 679 cm^{-1} corresponded to octahedral structures (AlO_6).

These observations align with previous studies [140,165,179] and corroborate the XRD identification of calcium aluminate phases, such as ye'elimite, grossite, and hibonite. The strong agreement between FTIR and XRD results provides a detailed understanding of phase transformations and structural evolution, highlighting the role of MgO content and temperature in shaping the stability and formation of phases like ye'elimite, fluorapatite, and spinel.

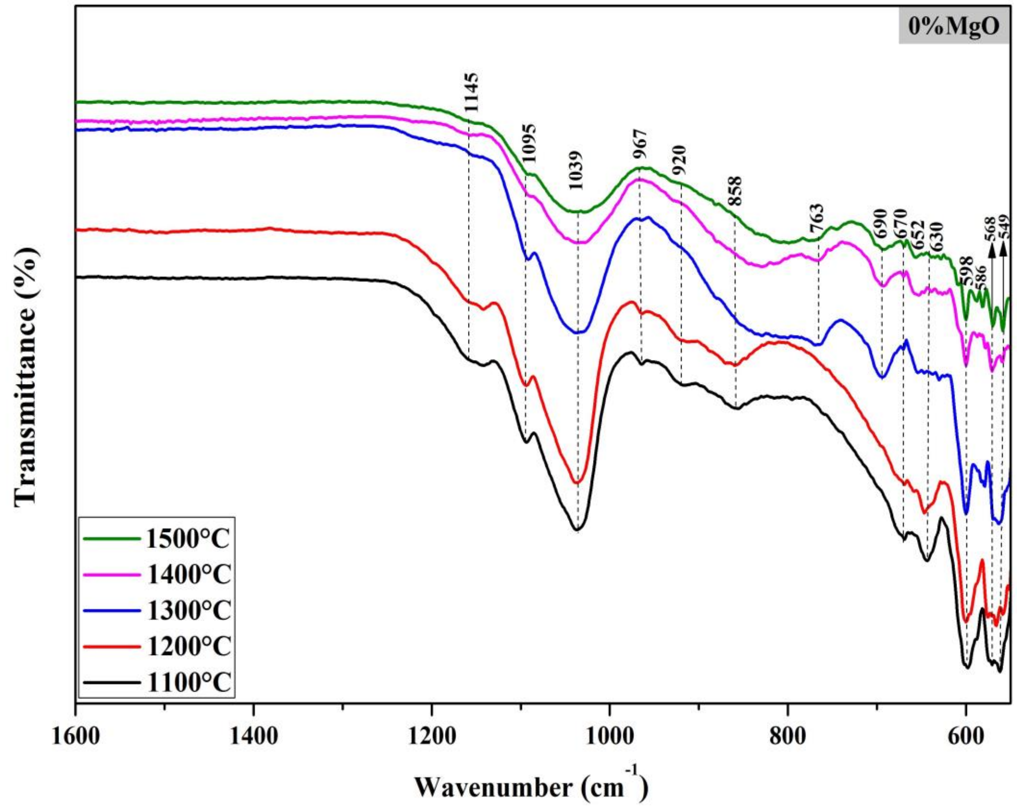
0%MgO
1145
1095
1039
967
920
858
763
690
670
652
630
598
586
568
549
1500°C
1400°C
1300°C
1200°C
1100°C
Transmittance (%)
1600
1400
1200
1000
800
600
Wavenumber (cm^{-1})

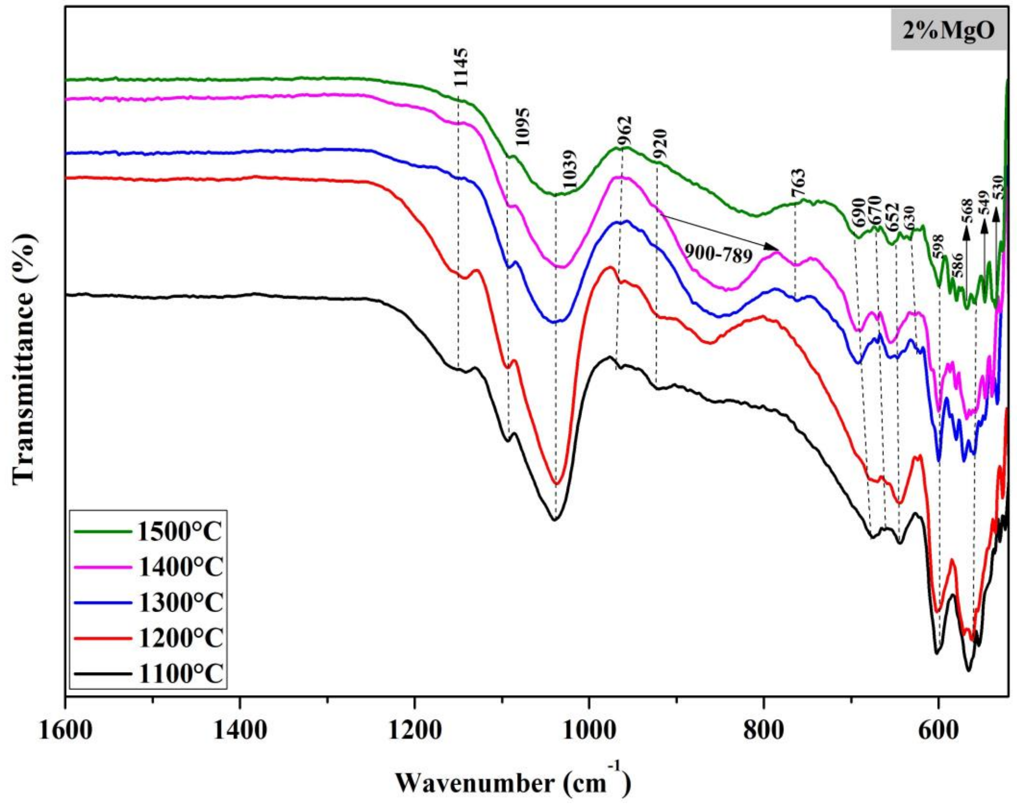
2%MgO
1145
1095
1039
962
920
900-789
763
690
670
652
630
598
586
568
549
530
1500°C
1400°C
1300°C
1200°C
1100°C
Transmittance (%)
1600
1400
1200
1000
800
600
Wavenumber (cm^{-1})

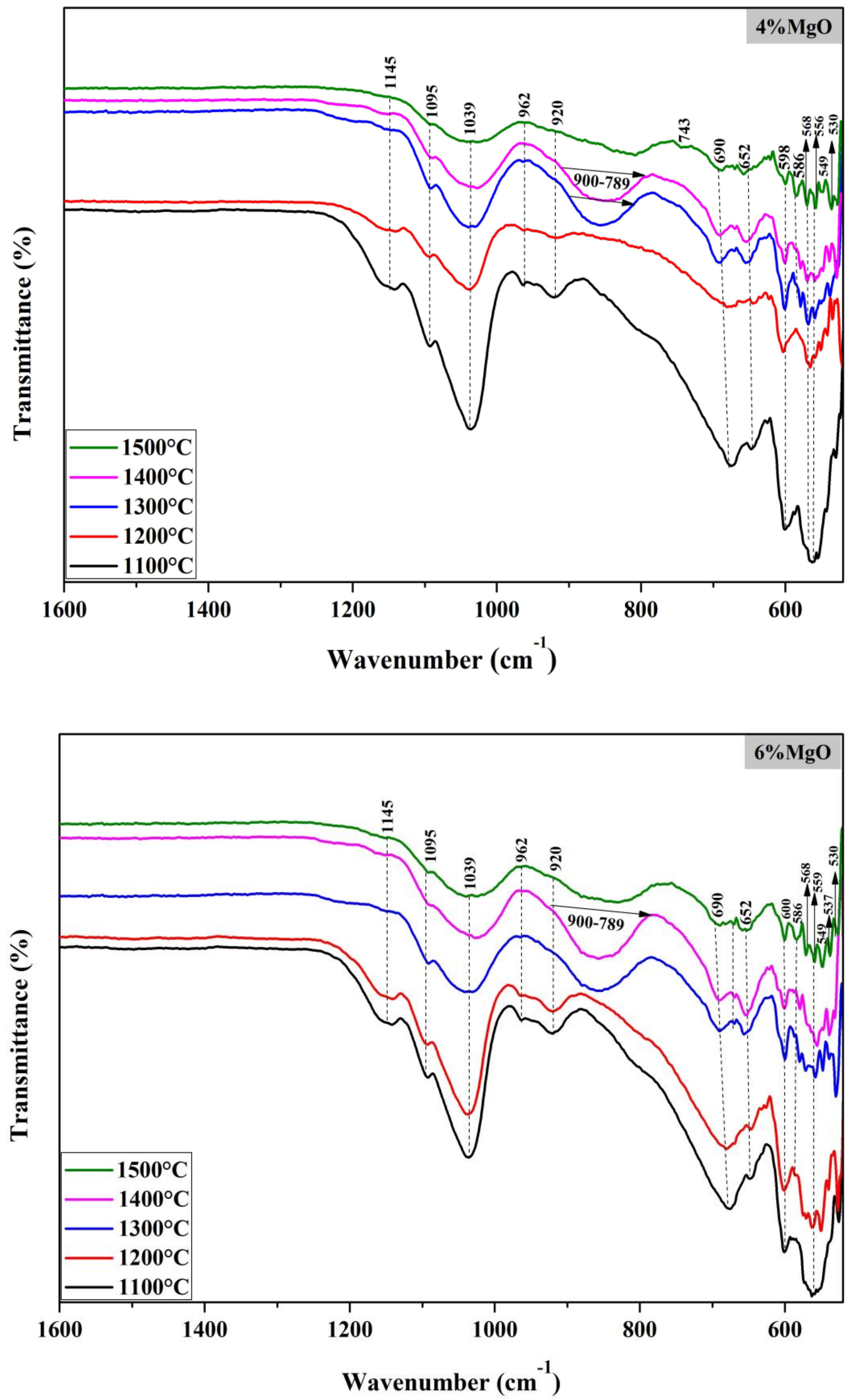

Fig.III.13. FT-IR spectrum of samples sintered at various temperatures.

III.3.3. Quantitative phase analysis of the sintered samples performed using the Rietveld refinement method.

Quantitative phase analysis was performed using the Rietveld method with the Profex software package [111,112]. The refinement process was iterated until convergence, and the quality of the fit was assessed using statistical indicators [108,180]. Fig.III.14 illustrates the composition of various mineral phases in the samples across a temperature range of 1100 °C to 1500 °C with varying MgO concentrations. At lower temperatures (1100 °C and 1200 °C), α-Al_2O_3 and anhydrite are present in all samples but show a decreasing trend with both increasing temperature and MgO content. For example, α-Al_2O_3 accounts for 37.29% at 1100 °C with 0% MgO but decreases to 21.18% at 1100 °C with 6% MgO. These phases react completely at temperatures of 1300 °C and higher.

Fluorapatite is observed in all samples, comprising approximately 40% at lower temperatures for all MgO concentrations. However, its content decreases with increasing temperatures, reaching its lowest levels at 1500 °C, ranging from 13.21% to 17.77%, depending on the MgO content [168,169]. This non-linear trend suggests interactions between MgO, fluorapatite [163,169], and other phases in the system, leading to the partial decomposition of fluorapatite into the β-TCP phase. Despite this decomposition, the β-TCP content remains relatively stable, ranging from 15.41% to 16.03%, as indicated by the XRD results in Fig.III.12 [135].

The XRD patterns closely align with the quantitative phase analysis with increasing temperatures. Notably, ye'elimite shows a clear trend: its content increases with temperature up to 1400 °C before declining. At 0% MgO, ye'elimite rises from 12.47% at 1100 °C to 30.47% at 1400 °C, then decreases to 18.58% at 1500 °C [136]. This trend is amplified with higher MgO content, reaching 40.76% at 1400 °C with 6% MgO [40,83]. Additionally, higher MgO content significantly promotes the formation of spinel. At 6% MgO, spinel starts at 25.18% at 1100 °C and increases to 31.30% at 1500 °C, exhibiting relative stability across the temperature range. MgO also stabilizes ye'elimite at elevated temperatures and influences the formation of other phases, such as hibonite and grossite [159,181].

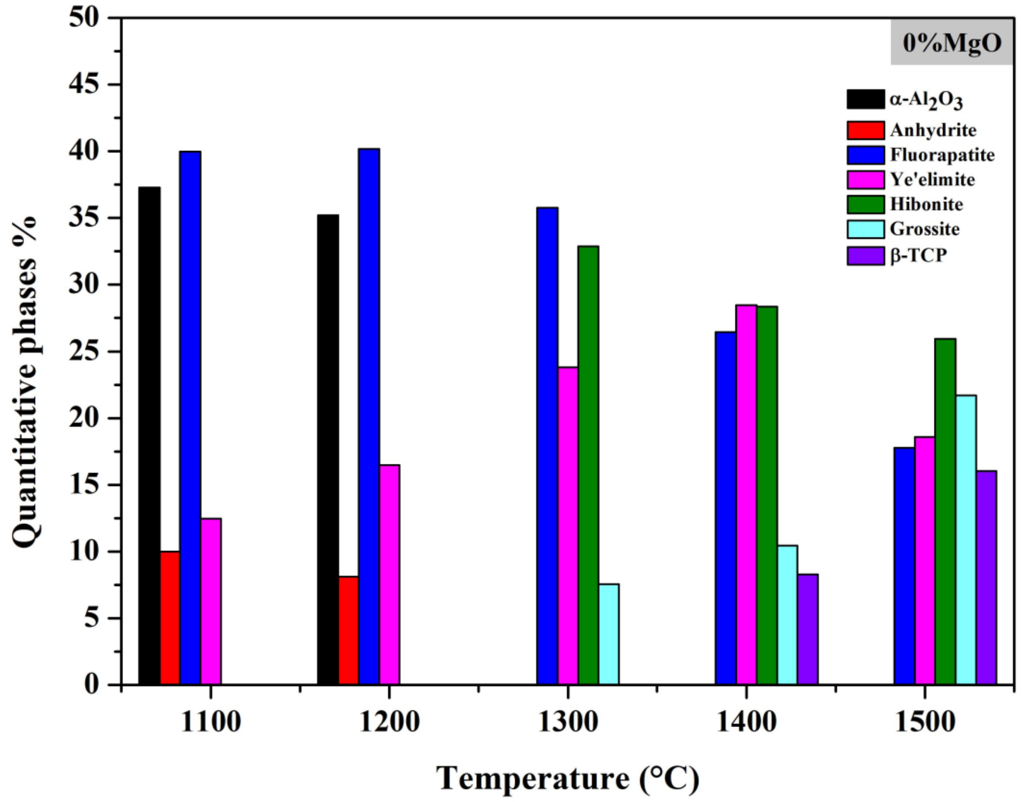
0%MgO
α-Al_2O_3
Anhydrite
Fluorapatite
Ye'elimite
Hibonite
Grossite
β-TCP
Quantitative phases %
0
5
10
15
20
25
30
35
40
45
50
1100
1200
1300
1400
1500
Temperature (°C)

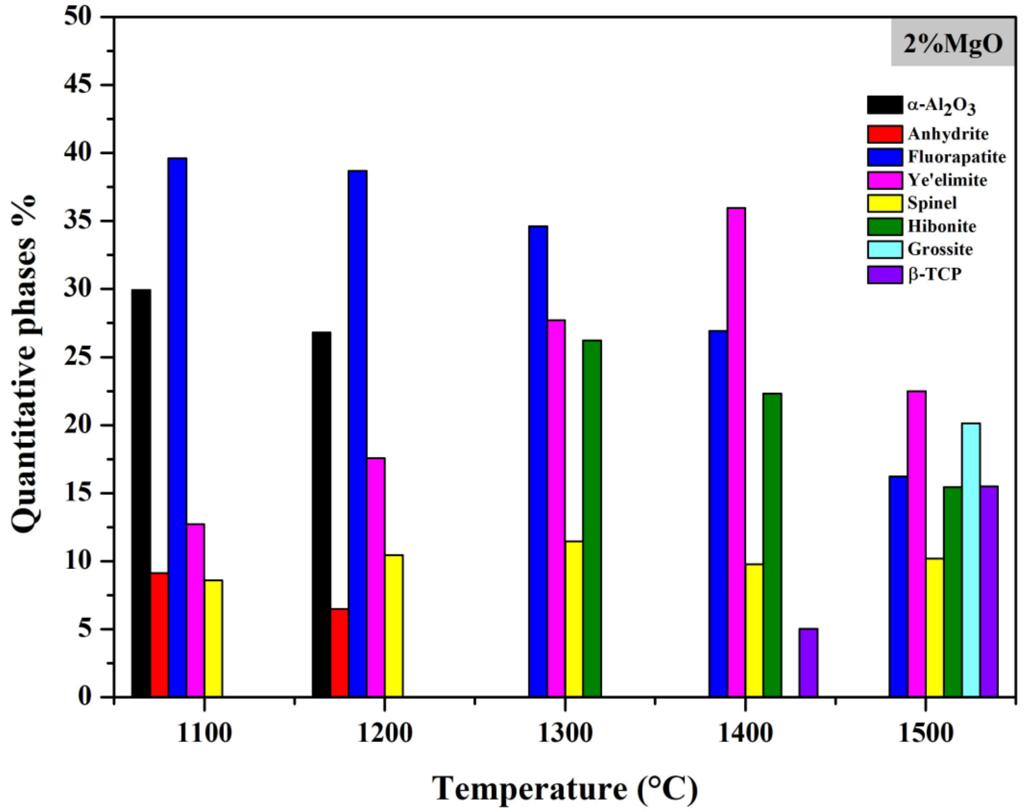
2%MgO
α-Al_2O_3
Anhydrite
Fluorapatite
Ye'elimite
Spinel
Hibonite
Grossite
β-TCP
Quantitative phases %
0
5
10
15
20
25
30
35
40
45
50
1100
1200
1300
1400
1500
Temperature (°C)

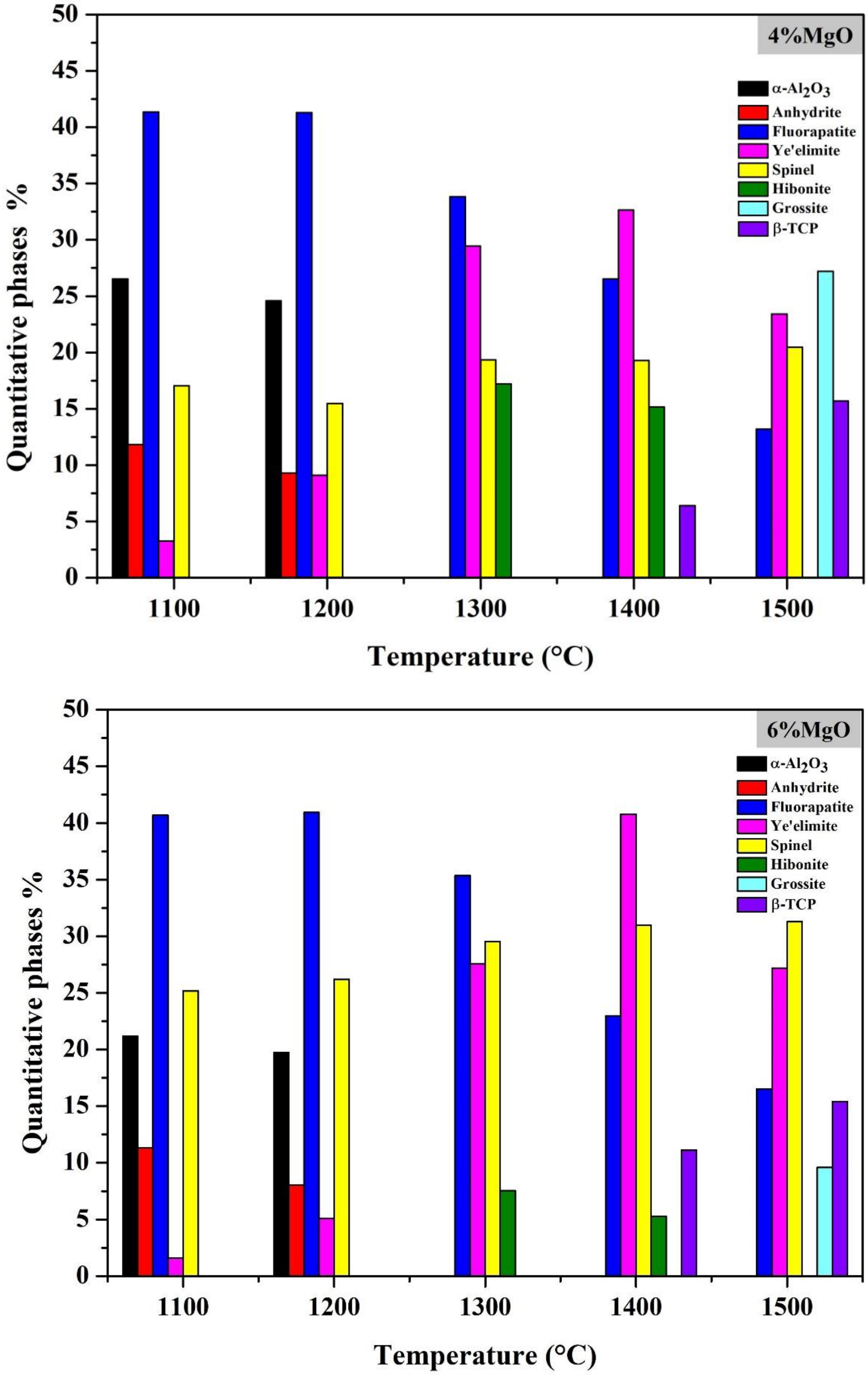

Fig.III.14. Quantitative phase composition (%) of the samples sintered at different temperatures with varying MgO additions.

The addition of MgO significantly impacts phase evolution, particularly with the emergence of high-temperature phases like hibonite, which appears at 1300 °C and above in samples with lower MgO concentrations. Hibonite is most prominent in samples with 0% MgO, reaching 32.87% at 1300 °C, but its presence decreases with increasing temperature and MgO content. At 6% MgO, hibonite is present only in small amounts, with 7.54% at 1300 °C and 5.28% at 1400 °C. Grossite primarily forms at 1500 °C, showing its highest concentration (27.21%) at 4% MgO, but its content decreases as MgO content increases at this temperature. These quantitative findings align with XRD observations, which confirm the simplification of the phase assemblage at higher temperatures, the dominance of ye'elimite and spinel in high-MgO samples, and the partial decomposition of fluorapatite into β-TCP at 1500 °C.

This comprehensive phase analysis offers valuable insights into the complex interactions between composition, temperature, and phase development in this ceramic system [31,134,145,168,182].

Table III. 5: Index of Rietveld refinements for samples sintered at different temperatures.

0%MgO	**1100°C**	**1200°C**	**1300°C**	**1400°C**	**1500°C**
Rwp	8.30	6.66	7.26	6.51	5.11
Rexp	2.98	2.92	2.82	2.80	2.78
GOF	2.79	2.28	2.57	2.33	1.84
2%MgO	1200°C	1300°C	1350°C	1400°C	1500°C
Rwp	7	6.66	6.07	6.09	5.58
Rexp	2.89	2.89	2.72	2.85	2.74
GOF	2.42	2.30	2.23	2.14	2.04
4%MgO	**1200°C**	**1300°C**	**1350°C**	**1400°C**	**1500°C**
Rwp	7.97	6.42	7.03	6.13	5.94
Rexp	2.87	2.85	2.80	2.77	2.75
GOF	2.78	2.25	2.51	2.21	2.16
6%MgO	**1200°C**	**1300°C**	**1350°C**	**1400°C**	**1500°C**
Rwp	7.19	6.66	6.49	7.87	7.55
Rexp	2.93	2.92	2.71	2.80	2.89
GOF	2.45	2.28	2.39	2.81	2.61

III.3.4. Microstructural analysis of sintered samples

A detailed analysis was performed to examine the microstructural changes in the samples. Fig.III.15 illustrates the morphology of powders with 0% and 6% MgO sintered for 2 hours at 1200 °C, highlighting clear differences depending on the presence of magnesium. The structure reveals a complex multi-phase composition, consisting of a matrix phase and various dispersed phases. The matrix forms a relatively continuous background, while the dispersed phases appear as aggregates ranging from 5 to 30 µm with a granular texture. In the 0% MgO sample, the grain boundaries are well-defined at 1200 °C, representing ye'elimite [156,160,183], while rod-like rectangular structures indicate the presence of fluorapatite crystals [66,134]. In contrast, the 6% MgO sample shows grain growth and the formation of dense clusters interspersed with larger, smoother regions, suggesting partial melting or enhanced sintering, as shown in Fig.III.15-b.

The EDS spectra for both samples confirm the presence of Ca, P, Al, and S, aligning with the expected composition of fluorapatite and ye'elimite [137]. A distinct magnesium peak is observed in the 6% MgO sample, verifying the incorporation of MgO. This addition appears to promote spinel formation, enhance the development of more defined crystals, and possibly contribute to the appearance of new phases, as suggested by the smoother regions visible in Fig.III.15-b. Variations in the relative intensities of the Ca, Al, S, and P peaks between the two samples indicate that MgO addition influences the phase composition and the relative abundances of fluorapatite, ye'elimite, and spinel in the composite [70].

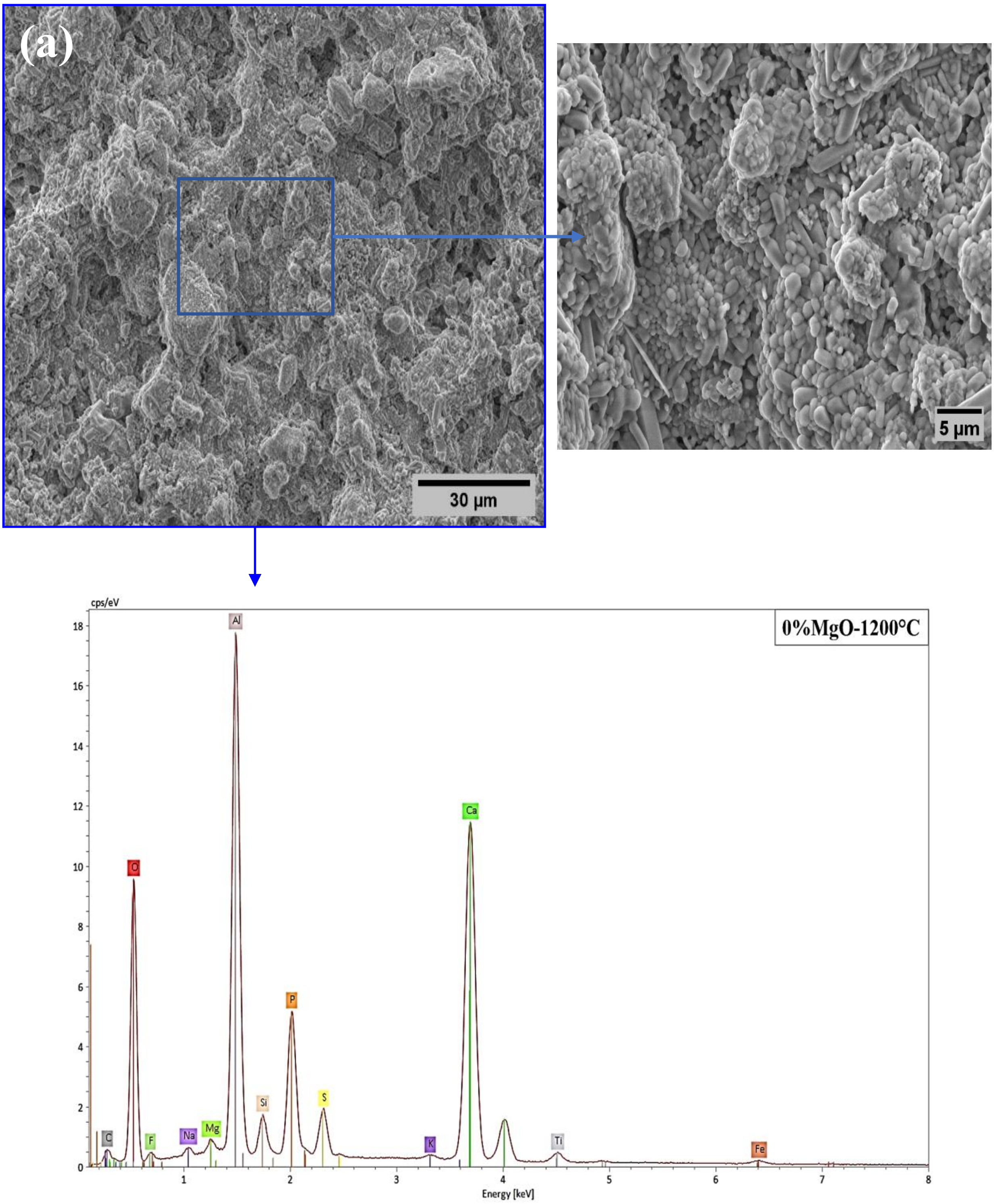
(a)
30 µm
5 µm
cps/eV
18
16
14
12
10
8
6
4
2
0
0%MgO-1200°C
Al
Ca
O
P
S
Si
C
F
Na
Mg
K
Ti
Fe
1
2
3
4
5
6
7
8
Energy [keV]

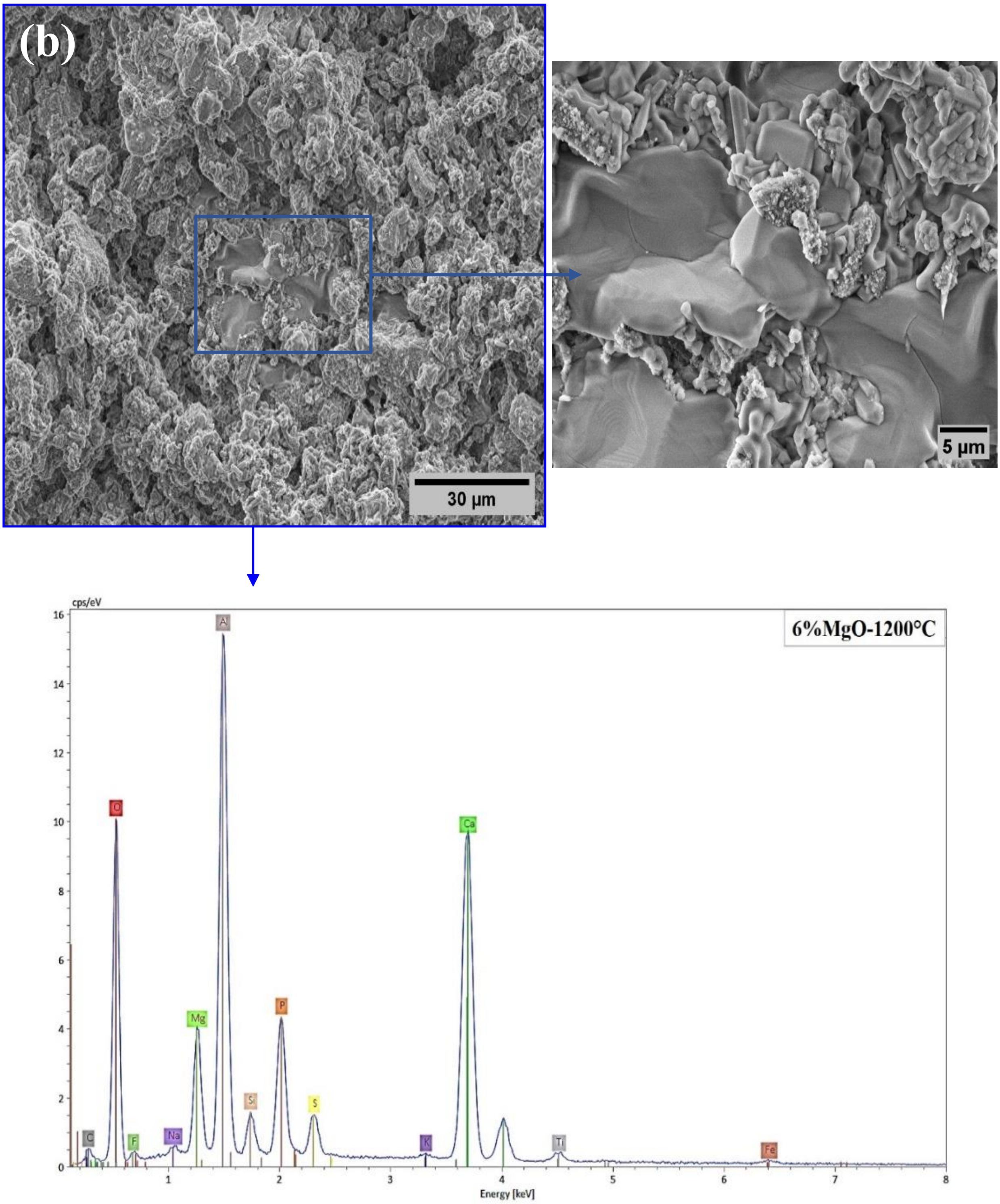

Fig.III.15. SEM-EDS analysis of the fracture surfaces for samples with 0% MgO (a) and 6% MgO (b), sintered at 1200 °C.

The SEM image in Fig.III.16 reveals notable microstructural differences between the samples with varying MgO contents. The sample containing 0 wt% MgO displayed diverse crystal structures, such as elongated rods, rounded grains, and small hexagonal grains, as shown in Fig.III.16-a. On the other hand, the 6 wt% MgO sample exhibited characteristics that suggest enhanced grain growth, densification, and the formation of a liquid phase during processing. This liquid phase appears to contribute to the formation of a dense interlocking microstructure and a range of grain shapes, as it facilitates particle rearrangement and solution-reprecipitation processes [129].

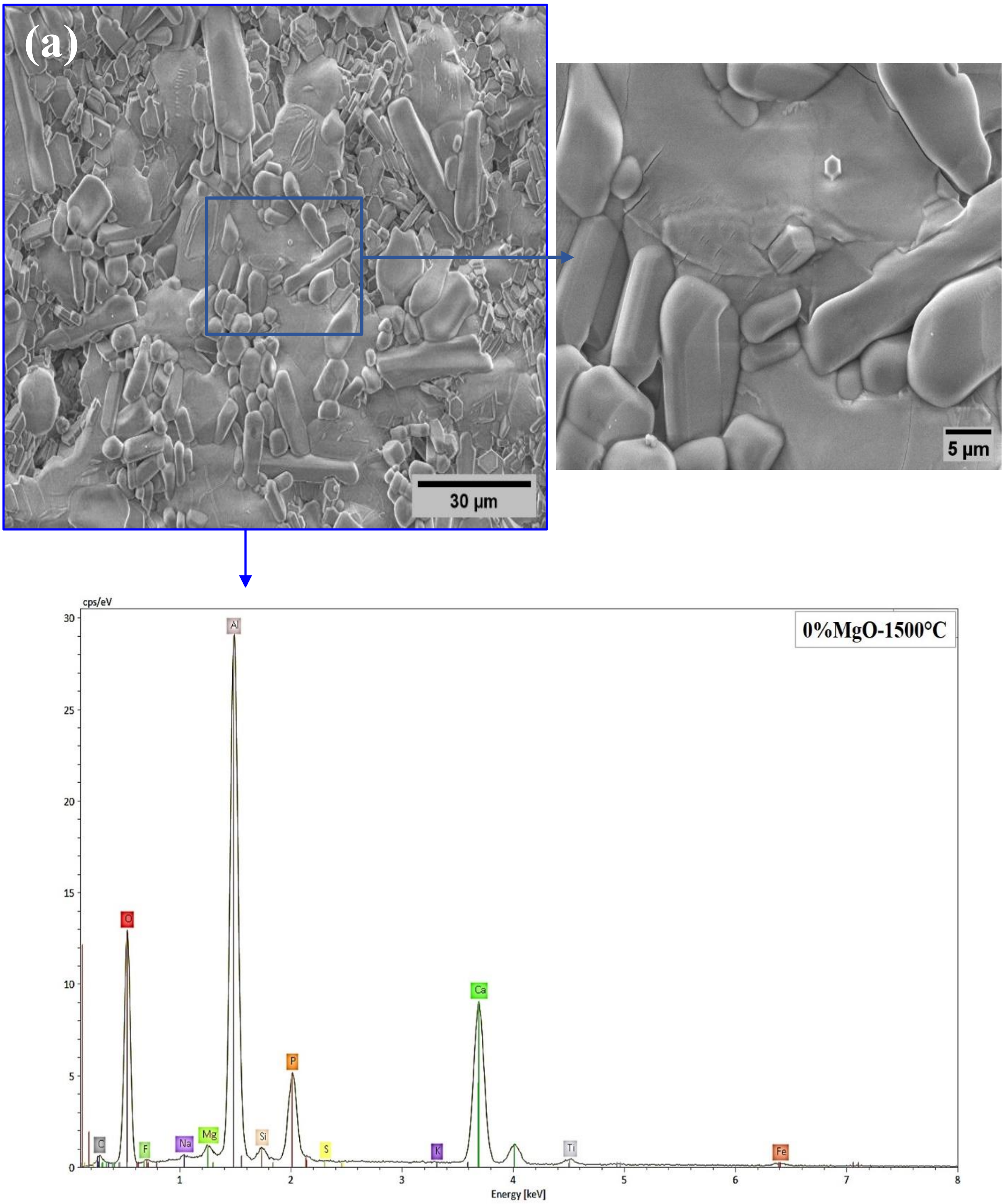

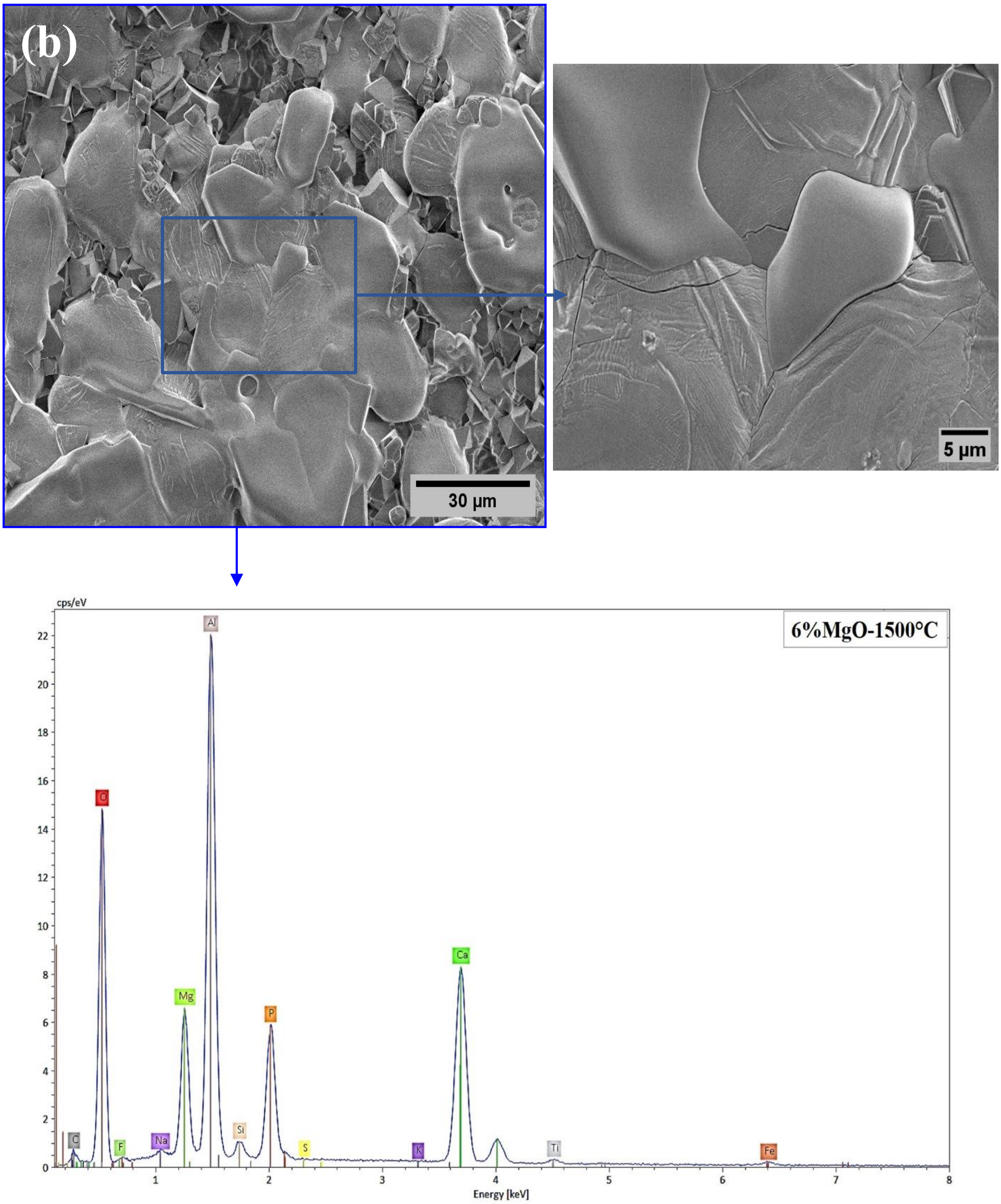

Fig.III.16. SEM-EDS analysis of the fracture surfaces for samples with 0% MgO (a) and 6% MgO (b), sintered at 1500 °C.

During cooling, the liquid phase may dissolve some initial phases and reprecipitate them, leading to the emergence of new phases or compositional gradients within the grains, as shown in Fig.III.16-b. The EDS results confirm the incorporation of Mg in the 6 wt% MgO sample, along with changes in the relative intensities of the Al, O, P, and Ca peaks, indicating that the presence of MgO alters the overall composition [138]. Additionally, at higher magnification (5 µm inset), the 6 wt% MgO at 1500 °C sample shows fine cracks across the larger grains, as shown in Fig.III.16-b. These cracks may arise from thermal stresses, phase transformations, or structural changes induced by MgO addition.

The presence of these cracks can affect the material properties, potentially reducing the mechanical strength while improving the thermal shock resistance. This observation highlights the intricate relationship between composition, processing conditions, and microstructure in determining the performance of these composites[167,169].

Conclusion

General Conclusion

This study successfully synthesized ye’elimite-based multiphase composites using natural phosphate (as alternative to limestone) and Algerian raw materials, developing fluorapatite-ye’elimite-calcium hexaluminate and fluorapatite-ye’elimite-spinel systems and analyzing their mineralogy and microstructure through the solid-state reaction method.

1. Effect of Quartz Addition

- ✓ Successfully manufactured diverse composites using natural fluorapatite (instead of limestone), bauxite, and gypsum, creating calcium hexaluminate-fluorapatite-ye'elimite-gehlenite composites.
- ✓ As the temperature increased from 1200 °C to 1500 °C, a series of complex phase transformations occurred, leading to the formation of ye'elimite, calcium hexaluminate, gehlenite, and eventually β-TCP and berlinite.
- ✓ Quartz addition accelerated fluorapatite partial decomposition at higher sintering temperatures, evidenced by FT-IR showing reduced phosphate group peak intensity.
- ✓ Rietveld analysis confirms that at high temperatures, ye’elimite and calcium hexaluminate contents increase significantly, fluorapatite partially decomposes into β-TCP, and gehlenite fully decomposes by 1500 °C.

2. Impact of Magnesium Oxide

- ✓ Lower temperatures (1100–1200 °C) led to the formation of various phases, including fluorapatite and ye'elimite, while higher temperatures (1300–1500 °C) resulted in ye'elimite becoming the dominant phase, highlighting its exceptional thermal stability.
- ✓ MgO content significantly altered the system by promoting $MgAl_2O_4$ (spinel) formation, stabilizing ye'elimite at higher temperatures, and influencing secondary phases like hibonite and grossite.
- ✓ At extreme conditions (1500°C with 6% MgO), the system approached a nearly two-phase composition of ye'elimite and spinel.
- ✓ Fluorapatite generally decreased with temperature, partially decomposing to β-TCP at 1500°C, with this decomposition accelerated in the presence of MgO.
- ✓ Rietveld quantitative analysis reveals that increasing sintering temperature and MgO content, enhance ye'elimite formation (maximum 40.76% at 1400°C with 6% MgO) and spinel development (up to 31%) while significantly reducing fluorapatite content to as low as 17%.

Final Remarks

This study provides a substantial contribution to the scientific understanding of ye’elimite-based materials synthesized from natural resources. Through the systematic investigation of quartz and MgO as functional additives, it elucidates their critical influence on phase evolution, microstructural development, and the overall performance of the resulting composites. The research highlights the necessity of precise compositional tuning and controlled processing parameters to achieve optimal material characteristics. Looking forward, these insights lay a solid foundation for future advancements in the design of sustainable, high-performance cementitious systems, offering promising avenues for the development of environmentally friendly construction materials that align with global sustainability objectives.

References

[1] S. Barbhuiya, F. Kanavaris, B.B. Das, M. Idrees, Decarbonising cement and concrete production: Strategies, challenges and pathways for sustainable development, J. Build. Eng. 86 (2024) 108861. https://doi.org/10.1016/j.jobe.2024.108861.

[2] N. Mohamad, K. Muthusamy, R. Embong, A. Kusbiantoro, M.H. Hashim, Environmental impact of cement production and Solutions: A review, Mater. Today Proc. 48 (2021) 741–746. https://doi.org/10.1016/j.matpr.2021.02.212.

[3] A. Rungchet, C.S. Poon, P. Chindaprasirt, K. Pimraksa, Synthesis of low-temperature calcium sulfoaluminate-belite cements from industrial wastes and their hydration: Comparative studies between lignite fly ash and bottom ash, Cem. Concr. Compos. 83 (2017) 10–19. https://doi.org/10.1016/j.cemconcomp.2017.06.013.

[4] Y. El Khessaimi, Y. El Hafiane, A. Smith, R. Trauchessec, C. Diliberto, A. Lecomte, Solid-state synthesis of pure ye’elimite, J. Eur. Ceram. Soc. 38 (2018) 3401–3411. https://doi.org/10.1016/j.jeurceramsoc.2018.03.018.

[5] S. Park, Y. Jeong, J. Moon, N. Lee, Hydration characteristics of calcium sulfoaluminate (CSA) cement/portland cement blended pastes, J. Build. Eng. 34 (2021) 101880. https://doi.org/10.1016/j.jobe.2020.101880.

[6] J. Péra, J. Ambroise, New applications of calcium sulfoaluminate cement, Cem. Concr. Res. 34 (2004) 671–676. https://doi.org/10.1016/j.cemconres.2003.10.019.

[7] S. Djouallah, H. Belhouchet, A. Kenzour, D. Kherifi, Sintering behavior of fluorapatite-based composites produced from natural phosphate and alumina, Ceram. Int. 47 (2021) 3553–3564. https://doi.org/10.1016/j.ceramint.2020.09.202.

[8] A. Mokhtari, H. Belhouchet, A. Guermat, In situ high-temperature X-ray diffraction, FT-IR and thermal analysis studies of the reaction between natural hydroxyapatite and aluminum powder, J. Therm. Anal. Calorim. 136 (2019) 1515–1526. https://doi.org/10.1007/s10973-018-7812-8.

[9] W. Kurdowski, Cement and concrete chemistry, Cem. Concr. Chem. 9789400779 (2014) 1–700. https://doi.org/10.1007/978-94-007-7945-7.

[10] M. Schneider, M. Romer, M. Tschudin, H. Bolio, Sustainable cement production-present and future, Cem. Concr. Res. 41 (2011) 642–650.

https://doi.org/10.1016/j.cemconres.2011.03.019.

[11] A. Adesina, Recent advances in the concrete industry to reduce its carbon dioxide emissions, Environ. Challenges 1 (2020) 100004. https://doi.org/10.1016/j.envc.2020.100004.

[12] G. Schumacher, L. Juniper, Coal utilisation in the cement and concrete industries, Coal Handb. Towar. Clean. Prod. 2 (2013) 387–426. https://doi.org/10.1533/9781782421177.3.387.

[13] S. Chandra, J. Björnström, Influence of superplasticizer type and dosage on the slump loss of Portland cement mortars - Part II, Cem. Concr. Res. 32 (2002) 1613–1619. https://doi.org/10.1016/S0008-8846(02)00838-4.

[14] M.Y.A. Mollah, M. Kesmez, D.L. Cocke, An X-ray diffraction (XRD) and Fourier transform infrared spectroscopic (FT-IR) investigation of the long-term effect on the solidification/ stabilization (S/S) of arsenic(V) in Portland cement type-V, Sci. Total Environ. 325 (2004) 255–262. https://doi.org/10.1016/j.scitotenv.2003.09.012.

[15] B.A. Silva, A.P. Ferreira Pinto, A. Gomes, Natural hydraulic lime versus cement for blended lime mortars for restoration works, Constr. Build. Mater. 94 (2015) 346–360. https://doi.org/10.1016/j.conbuildmat.2015.06.058.

[16] V. Afroughsabet, G. Geng, A. Lin, L. Biolzi, C.P. Ostertag, P.J.M. Monteiro, The influence of expansive cement on the mechanical, physical, and microstructural properties of hybrid-fiber-reinforced concrete, Cem. Concr. Compos. 96 (2019) 21–32. https://doi.org/10.1016/j.cemconcomp.2018.11.012.

[17] H. Yang, L. Wang, C. Yang, J. Zhao, G. Huang, Y. Guo, W.V. Liu, Mechanical performance of oil-well cement slurries cured and tested under high-temperatures and high-pressures for deep-well applications, Cem. Concr. Res. 175 (2024) 107355. https://doi.org/10.1016/j.cemconres.2023.107355.

[18] J. Mahadevan, N.M. Kuriakose, G.A. Kannan, N.D. Suryaa, D. Sathyan, K.M. Mini, Rheological and strength properties of fly ash incorporated rapid hardening cement mix, Mater. Today Proc. 46 (2019) 4795–4799. https://doi.org/10.1016/j.matpr.2020.10.315.

[19] S. Jian, W. Gao, Y. Lv, H. Tan, X. Li, B. Li, W. Huang, Potential utilization of copper

tailings in the preparation of low heat cement clinker, Constr. Build. Mater. 252 (2020) 119130. https://doi.org/10.1016/j.conbuildmat.2020.119130.

[20] S. Martinovic, M. Vlahovic, M. Dojcinovic, T. Volkov-Husovic, J. Majstorovic, Thermomechanical properties and cavitation resistance of a high-alumina low-cement castable, Int. J. Appl. Ceram. Technol. 8 (2011) 1115–1124. https://doi.org/10.1111/j.1744-7402.2010.02545.x.

[21] I. Soroka, Portland Cement Paste and Concrete, Int. J. Cem. Compos. Light. Concr. 1 (1979) 97–98. https://doi.org/10.1016/0262-5075(79)90018-6.

[22] T.F. Yen, Cement Chemistry, Chem. Eng. (2008) 387–433. https://doi.org/10.1142/9781860949982_0010.

[23] K. Pimraksa, P. Chindaprasirt, Sulfoaluminate cement-based concrete, Eco-Efficient Repair Rehabil. Concr. Infrastructures (2018) 355–385. https://doi.org/10.1016/B978-0-08-102181-1.00014-9.

[24] K.L. Scrivener, V.M. John, E.M. Gartner, Eco-efficient cements: Potential economically viable solutions for a low-CO2 cement-based materials industry, Cem. Concr. Res. 114 (2018) 2–26. https://doi.org/10.1016/j.cemconres.2018.03.015.

[25] J. Mokrá, K. Kulísek, D. Gazdič, M. Fridrichová, Long-term Observation of Yeelimite Clinker Hydration in Environment of Saturated Water Vapour, Procedia Eng. 151 (2016) 94–99. https://doi.org/10.1016/j.proeng.2016.07.385.

[26] G. Álvarez-Pinazo, A. Cuesta, M. García-Maté, I. Santacruz, E.R. Losilla, A.G.D. La Torre, L. León-Reina, M.A.G. Aranda, Rietveld quantitative phase analysis of Yeelimite-containing cements, Cem. Concr. Res. 42 (2012) 960–971. https://doi.org/10.1016/j.cemconres.2012.03.018.

[27] M.A.G. Aranda, A.G. De la Torre, Sulfoaluminate cement, Eco-Efficient Concr. (2013) 488–522. https://doi.org/10.1533/9780857098993.4.488.

[28] Y. El Khessaimi, Y. El Hafiane, A. Smith, Examination of ye'elimite formation mechanisms, J. Eur. Ceram. Soc. 39 (2019) 5086–5095. https://doi.org/10.1016/j.jeurceramsoc.2019.07.042.

[29] S. Sahu, J. Majling, Phase compatibility in the system CaOSiO2Al2O3Fe2O3SO3 referred to sulphoaluminate belite cement clinker, Cem. Concr. Res. 23 (1993) 1331–

1339. https://doi.org/10.1016/0008-8846(93)90070-P.

[30] R.I. Iacobescu, Y. Pontikes, D. Koumpouri, G.N. Angelopoulos, Synthesis, characterization and properties of calcium ferroaluminate belite cements produced with electric arc furnace steel slag as raw material, Cem. Concr. Compos. 44 (2013) 1–8. https://doi.org/10.1016/j.cemconcomp.2013.08.002.

[31] L.H.J. Martin, F. Winnefeld, C.J. Müller, B. Lothenbach, Contribution of limestone to the hydration of calcium sulfoaluminate cement, Cem. Concr. Compos. 62 (2015) 204–211. https://doi.org/10.1016/j.cemconcomp.2015.07.005.

[32] Q. Zhou, N.B. Milestone, M. Hayes, An alternative to Portland Cement for waste encapsulation-The calcium sulfoaluminate cement system, J. Hazard. Mater. 136 (2006) 120–129. https://doi.org/10.1016/j.jhazmat.2005.11.038.

[33] F. Winnefeld, B. Lothenbach, Hydration of calcium sulfoaluminate cements - Experimental findings and thermodynamic modelling, Cem. Concr. Res. 40 (2010) 1239–1247. https://doi.org/10.1016/j.cemconres.2009.08.014.

[34] J. Bizzozero, C. Gosselin, K.L. Scrivener, Expansion mechanisms in calcium aluminate and sulfoaluminate systems with calcium sulfate, Cem. Concr. Res. 56 (2014) 190–202. https://doi.org/10.1016/j.cemconres.2013.11.011.

[35] S. Berger, Etude des potentialités des ciments sulfo-alumineux bélitique pour le conditionnement du zinc : de l’hydratation à la durabilité, Dr. Thesis. Univ. Sci. Technol. Lille-Lille I. (2009) 324. https://doi.org/https://theses.hal.science/tel-00595609v1.

[36] A. Cuesta, Á.G. De La Torre, E.R. Losilla, I. Santacruz, M.A.G. Aranda, Pseudocubic crystal structure and phase transition in doped ye’elimite, Cryst. Growth Des. 14 (2014) 5158–5163. https://doi.org/10.1021/cg501290q.

[37] M.T. Pedersen, F. Jensen, J. Skibsted, Structural Investigation of Ye’elimite, Ca4Al6O12SO4, by 27Al MAS and MQMAS NMR at Different Magnetic Fields, J. Phys. Chem. C 122 (2018) 12077–12089. https://doi.org/10.1021/acs.jpcc.8b02497.

[38] A. Cuesta, A.G. De La Torre, E.R. Losilla, V.K. Peterson, P. Rejmak, A. Ayuela, C. Frontera, M.A.G. Aranda, Structure, atomistic simulations, and phase transition of stoichiometric yeelimite, Chem. Mater. 25 (2013) 1680–1687.

https://doi.org/10.1021/cm400129z.

[39] S. Liu, X. Lu, J. Chen, S. Wang, Z. Ye, X. Cheng, Modulation of two ye'elimite phases via Ga3+ cation substitution, CrystEngComm 20 (2018) 3755–3764. https://doi.org/10.1039/c8ce00405f.

[40] M. Ben Haha, F. Winnefeld, A. Pisch, Advances in understanding ye'elimite-rich cements, Cem. Concr. Res. 123 (2019) 105778. https://doi.org/10.1016/j.cemconres.2019.105778.

[41] Y. Tao, A. V Rahul, M.K. Mohan, G. De Schutter, K. Van Tittelboom, Recent progress and technical challenges in using calcium sulfoaluminate (CSA) cement, Cem. Concr. Compos. 137 (2023). https://doi.org/https://doi.org/10.1016/j.cemconcomp.2022.104908.

[42] X. Li, Y. Zhang, X. Shen, Q. Wang, Z. Pan, Kinetics of calcium sulfoaluminate formation from tricalcium aluminate, calcium sulfate and calcium oxide, Cem. Concr. Res. 55 (2014) 79–87. https://doi.org/10.1016/j.cemconres.2013.10.006.

[43] F. Nabila Bouha, L. Kacimi, A.G. De la Torre, Manufacture of rich-sulfoaluminate belite cement at low temperature from waste mixture by dry and hydrothermal processes, Constr. Build. Mater. 314 (2022) 125641. https://doi.org/10.1016/j.conbuildmat.2021.125641.

[44] Y. El Khessaimi, Synthesis and hydration of ye ' elimite, Dr. Thesis. Univ. Limoges (2019). https://doi.org/https://theses.hal.science/tel-02464853/document.

[45] Z. Sha, X. Long, J. Feng, H. Jiang, T. Wang, Development of a fast-hardening retarding high-early-strength concrete with low-alkalinity sulphoaluminate cement and practical application, Adv. Bridg. Eng. 1 (2020) 1–22. https://doi.org/10.1186/s43251-020-00024-5.

[46] J. Zhang, C. Ye, H. Tan, X. Liu, Potential application of Portland cement-sulfoaluminate cement system in precast concrete cured under ambient temperature, Constr. Build. Mater. 251 (2020) 118869. https://doi.org/10.1016/j.conbuildmat.2020.118869.

[47] J.J. Kouadjo Tchekwagep, F. Yang, S. Wang, P. Zhao, S. Huang, C. Yang, X. Cheng, Chinese raw vermiculite: A potential additive for improving the thermal properties of

calcium sulfoaluminate cement-blended mortars for applications in hot regions, J. Build. Eng. 92 (2024) 109723. https://doi.org/10.1016/j.jobe.2024.109723.

[48] J. Liu, Y. Li, C. Jin, Y. Li, H. Lin, J. Shen, Mechanism study on the effect of diammonium hydrogen phosphate on the setting time and micro-nanostructure of ordinary Portland cement paste, Constr. Build. Mater. 407 (2023) 133616. https://doi.org/10.1016/j.conbuildmat.2023.133616.

[49] S. V. Dorozhkin, P.R. Young, Calcium phosphates in geological, biological, and industrial systems, Water-Formed Depos. Fundam. Mitig. Strateg. (2022) 141–165. https://doi.org/10.1016/B978-0-12-822896-8.00011-X.

[50] B. Wopenka, J.D. Pasteris, A mineralogical perspective on the apatite in bone, Mater. Sci. Eng. C 25 (2005) 131–143. https://doi.org/10.1016/j.msec.2005.01.008.

[51] I. Uysal, F. Severcan, Z. Evis, Characterization by Fourier transform infrared spectroscopy of hydroxyapatite co-doped with zinc and fluoride, Ceram. Int. 39 (2013) 7727–7733. https://doi.org/10.1016/j.ceramint.2013.03.029.

[52] K. Tõnsuaadu, K.A. Gross, L. Pluduma, M. Veiderma, A review on the thermal stability of calcium apatites, J. Therm. Anal. Calorim. 110 (2012) 647–659. https://doi.org/10.1007/s10973-011-1877-y.

[53] A. Kenzour, laboration et caractérisation d’un phosphate tricalcique à partir du kaolin et de phosphate nature, Dr. Thesis, Univ. Setif. (2021).

[54] B.I. Bogdanov, P.S. Pashev, J.H. Hristov, I.G. Markovska, Bioactive fluorapatite-containing glass ceramics, Ceram. Int. 35 (2009) 1651–1655. https://doi.org/10.1016/j.ceramint.2008.07.021.

[55] S. Naray-Szabo, 27. The structure of apatite (CaF)Ca4(PO4)3, Zeitschrift Fur Krist. - Cryst. Mater. 75 (1930) 387–398. https://doi.org/10.1515/zkri-1930-0129.

[56] C.A. Beevers, D.B. McIntyre, The atomic structure of fluor-apatite and its relation to that of tooth and bone material. (With Plates XVI-XVIII.), Mineral. Mag. J. Mineral. Soc. 27 (1946) 254–257. https://doi.org/10.1180/minmag.1946.027.194.05.

[57] R.A. Young, Biological apatite vs hydroxyapatite at the atomic level, Clin. Orthop. Relat. Res. 113 (1975) 249–262. https://doi.org/10.1097/00003086-197511000-00036.

[58] K. Sudarsanan, P.E. Mackie, R.A. Young, Comparison of synthetic and mineral fluorapatite, Ca5 (PO4)3F, in crystallographic detail, Mater. Res. Bull. 7 (1972) 1331–1337. https://doi.org/10.1016/0025-5408(72)90113-4.

[59] I.A. Karampas, C.G. Kontoyannis, Characterization of calcium phosphates mixtures, Vib. Spectrosc. 64 (2013) 126–133. https://doi.org/10.1016/j.vibspec.2012.11.003.

[60] A. Kenzour, H. Belhouchet, M. Kolli, S. Djouallah, D. Kherifi, S. Ramesh, Sintering behavior of anorthite-based composite ceramics produced from natural phosphate and kaolin, Ceram. Int. 45 (2019) 20258–20265. https://doi.org/10.1016/j.ceramint.2019.06.299.

[61] S. Brahimi, A. Ressler, K. Boumchedda, M. Hamidouche, A. Kenzour, R. Djafar, M. Antunović, L. Bauer, P. Hvizdoš, H. Ivanković, Preparation and characterization of biocomposites based on chitosan and biomimetic hydroxyapatite derived from natural phosphate rocks, Mater. Chem. Phys. 276 (2022). https://doi.org/10.1016/j.matchemphys.2021.125421.

[62] M. Gao, W. Wang, H. Yang, B.C. Ye, Hydrothermal synthesis of hierarchical hollow hydroxyapatite microspheres with excellent fluoride adsorption property, Microporous Mesoporous Mater. 289 (2019) 109620. https://doi.org/10.1016/j.micromeso.2019.109620.

[63] T. Sahraoui, F. Chouia, Y.I. Bourezg, A. Guelil, Effect of natural phosphate content on the growth kinetics of hydroxyapatite crystals grown from kaolin clay, Mater. Chem. Phys. 292 (2022) 126865. https://doi.org/10.1016/j.matchemphys.2022.126865.

[64] P. Sikder, Y. Ren, S.B. Bhaduri, Microwave processing of calcium phosphate and magnesium phosphate based orthopedic bioceramics: A state-of-the-art review, Acta Biomater. 111 (2020) 29–53. https://doi.org/10.1016/j.actbio.2020.05.018.

[65] E. Champion, Sintering of calcium phosphate bioceramics, Acta Biomater. 9 (2013) 5855–5875. https://doi.org/10.1016/j.actbio.2012.11.029.

[66] L. Xie, M. Deng, J. Tang, K. Liu, The effect of fluorapatite in limestones on the mineral compositions of Portland cement clinkers, Constr. Build. Mater. 273 (2021) 122042. https://doi.org/10.1016/j.conbuildmat.2020.122042.

[67] T. Staněk, P. Sulovský, The influence of phosphorous pentoxide on the phase

composition and formation of Portland clinker, Mater. Charact. 60 (2009) 749–755. https://doi.org/10.1016/j.matchar.2008.11.013.

[68] S. Boughanmi, I. Labidi, A. Megriche, M. El Maaoui, A. Nonat, Natural fluorapatite as a raw material for Portland clinker, Cem. Concr. Res. 105 (2018) 72–80. https://doi.org/10.1016/j.cemconres.2018.01.006.

[69] M.N. De Noirfontaine, S. Tusseau-Nenez, M. Signes-Frehel, G. Gasecki, C. Girod-Labianca, Effect of phosphorus impurity on tricalcium silicate T1: From synthesis to structural characterization, J. Am. Ceram. Soc. 92 (2009) 2337–2344. https://doi.org/10.1111/j.1551-2916.2009.03092.x.

[70] J. Yu, J. Qian, H. Chen, Y. Ou, D. Kuang, X. Jia, H. Qiu, The influence of calcium sulphoaluminate on the properties of low-cost magnesium phosphate cement mortars, J. Build. Eng. 76 (2023) 107146. https://doi.org/10.1016/j.jobe.2023.107146.

[71] C. Ren, W. Wang, S. Wu, Y. Yao, Preparation of sulphoaluminate-magnesium potassium phosphate cementitious composite material under low-temperature, Constr. Build. Mater. 202 (2019) 246–253. https://doi.org/10.1016/j.conbuildmat.2018.12.180.

[72] B. Boumaza, R. Kechiched, T.V. Chekushina, Trace metal elements in phosphate rock wastes from the Djebel Onk mining area (Tébessa, eastern Algeria): A geochemical study and environmental implications, Appl. Geochemistry 127 (2021) 104910. https://doi.org/10.1016/j.apgeochem.2021.104910.

[73] D. Donaldson, B.E. Raahauge, Essential Readings in Light Metals: Alumina and Bauxite, Volume 1, Essent. Readings Light Met. Alumina Bauxite, Vol. 1 1 (2013). https://doi.org/10.1002/9781118647868.

[74] A. Benkhelif, M. Kolli, Synthesis of Pure Magnesium Aluminate Spinel (MgAl2O4) from Waste Aluminum Dross, Waste and Biomass Valorization 13 (2022) 2637–2649. https://doi.org/10.1007/s12649-022-01677-1.

[75] K. Salim, D. Youcef, Characterization and Origin of Gypsum Rhizoliths of Ziban Oases Soil-Algeria, World Appl. Sci. J. 34 (7) (2016) 948–955. https://doi.org/10.5829/idosi.wasj.2016.34.7.108.

[76] S. Mohammed, O. Safiullah, Optimization of the SO3 content of an Algerian Portland cement: Study on the effect of various amounts of gypsum on cement properties,

Constr. Build. Mater. 164 (2018) 362–370. https://doi.org/10.1016/j.conbuildmat.2017.12.218.

[77] N. Meftah, M.S. Mahboub, Spectroscopic Characterizations of Sand Dunes Minerals of El-Oued (Northeast Algerian Sahara) by FTIR, XRF and XRD Analyses, Silicon 12 (2020) 147–153. https://doi.org/10.1007/s12633-019-00109-5.

[78] F. Fernandes, S. Manari, M. Aguayo, K. Santos, T. Oey, Z. Wei, G. Falzone, N. Neithalath, G. Sant, On the feasibility of using phase change materials (PCMs) to mitigate thermal cracking in cementitious materials, Cem. Concr. Compos. 51 (2014) 14–26. https://doi.org/10.1016/j.cemconcomp.2014.03.003.

[79] C. Torney, A.M. Forster, P.F.G. Banfill, E.M. Szadurski, The effects of site practice on the physical properties of proprietary stone restoration mortar, Constr. Build. Mater. 75 (2015) 359–367. https://doi.org/10.1016/j.conbuildmat.2014.11.040.

[80] W. Zhou, Q. Ye, Z. Zhou, Z. liu, J.T. Aladejana, J. Cao, J. Li, A high-strength bonding, water-resistance, flame-retardant magnesium oxychloride cement based inorganic adhesive via the construction of supramolecular system, J. Clean. Prod. 419 (2023) 138239. https://doi.org/10.1016/j.jclepro.2023.138239.

[81] E. Rodríguez, G.A. Castillo, J. Contreras, R. Puente-Ornelas, J.A. Aguilar-Martínez, L. García, C. Gómez, Hercynite and magnesium aluminate spinels acting as a ceramic bonding in an electrofused MgO-CaZrO 3 refractory brick for the cement industry, Ceram. Int. 38 (2012) 6769–6775. https://doi.org/10.1016/j.ceramint.2012.05.071.

[82] C. Wu, C. Chen, H. Zhang, Y. Tan, H. Yu, Preparation of magnesium oxysulfate cement using magnesium-rich byproducts from the production of lithium carbonate from salt lakes, Constr. Build. Mater. 172 (2018) 597–607. https://doi.org/10.1016/j.conbuildmat.2018.04.005.

[83] V. Revilla-Cuesta, L. Evangelista, J. de Brito, M. Skaf, V. Ortega-López, Mechanical performance and autogenous and drying shrinkage of MgO-based recycled aggregate high-performance concrete, Constr. Build. Mater. 314 (2022). https://doi.org/10.1016/j.conbuildmat.2021.125726.

[84] P. Zhang, A. Chen, D. Ding, S. Gao, X. Liu, G. Ye, G. Liao, Trace nanoscale Al2O3 in Al2O3-MgAl2O4 castable for improved thermal shock performance, Ceram. Int. 45 (2019) 23029–23036. https://doi.org/10.1016/j.ceramint.2019.07.350.

[85] M.S. El-Eskandarany, Mechanical Alloying: Nanotechnology, Materials Science and Powder Metallurgy, William Andrew-an Impr. Elsevier (2015) 1–350.

[86] K. Stepney, E. Martin, G. Montague, Multivariate Analysis of API Particle Size Distribution Variation in a Manufacturing Environment, Comput. Aided Chem. Eng. 31 (2012) 1140–1144. https://doi.org/10.1016/B978-0-444-59506-5.50059-6.

[87] S. Nasrazadani, S. Hassani, Chapter 2 - Modern analytical techniques in failure analysis of aerospace, chemical, and oil and gas industries, Handb. Mater. Fail. Anal. with Case Stud. from Oil Gas Ind. (2016) 39–54. https://doi.org/10.1016/B978-0-08-100117-2.00010-8.

[88] S.N. Kabekkodu, A. Dosen, T.N. Blanton, PDF-5+: A comprehensive powder diffraction file^{TM} for materials characterization, Powder Diffr. 39 (2024) 47–59. https://doi.org/10.1017/S0885715624000150.

[89] A.A. Bunaciu, E. gabriela Udriştioiu, H.Y. Aboul-Enein, X-Ray Diffraction: Instrumentation and Applications, Crit. Rev. Anal. Chem. 45 (2015) 289–299. https://doi.org/10.1080/10408347.2014.949616.

[90] W. Clegg, X-ray Diffraction, Compr. Coord. Chem. II (2003) 57–64. https://doi.org/10.1016/B0-08-043748-6/01115-4.

[91] G. Will, Powder Diffraction: The Rietveld Method and the Two Stage Method to Determine and Refine Crystal Structures from Powder Diffraction Data, Springer (2006) 1–224. https://doi.org/https://doi.org/10.1007/3-540-27986-5.

[92] G. Le Saoût, V. Kocaba, K. Scrivener, Application of the Rietveld method to the analysis of anhydrous cement, Cem. Concr. Res. 41 (2011) 133–148. https://doi.org/10.1016/j.cemconres.2010.10.003.

[93] N. Döbelin, R. Archer, V. Tu, A free and open-source solution for Rietveld refinement of XRD data from the CheMin instrument onboard the Mars rover Curiosity, Planet. Space Sci. 224 (2022). https://doi.org/10.1016/j.pss.2022.105596.

[94] J. Abraham, A.P. Mohammed, M.P.A. Kumar, S.C. George, S. Thomas, Thermoanalytical techniques of nanomaterials, Charact. Nanomater. Adv. Key Technol. (2018) 213–236. https://doi.org/10.1016/B978-0-08-101973-3.00008-0.

[95] E. Broitman, Indentation Hardness Measurements at Macro-, Micro-, and Nanoscale: A

Critical Overview, Tribol. Lett. 65 (2017) 1–18. https://doi.org/10.1007/s11249-016-0805-5.

[96] S.A. Shahdad, J.F. McCabe, S. Bull, S. Rusby, R.W. Wassell, Hardness measured with traditional Vickers and Martens hardness methods, Dent. Mater. 23 (2007) 1079–1085. https://doi.org/10.1016/j.dental.2006.10.001.

[97] A.K. Singh, Experimental Methodologies for the Characterization of Nanoparticles, Eng. Nanoparticles (2016) 125–170. https://doi.org/10.1016/b978-0-12-801406-6.00004-2.

[98] J. Krejsová, R. Kužel, M. Keppert, L. Scheinherrová, A. Vimmrová, New insight into the phase changes of gypsum, Mater. Struct. Constr. 57 (2024) 1–17. https://doi.org/10.1617/s11527-024-02404-z.

[99] E. Tkalčec, J. Popović, S. Orlić, S. Milardović, H. Ivanković, Hydrothermal synthesis and thermal evolution of carbonate- fluorhydroxyapatite scaffold from cuttlefish bones, Mater. Sci. Eng. C 42 (2014) 578–586. https://doi.org/10.1016/j.msec.2014.05.079.

[100] A. Berrio, J.I. Tobón, A.G. De la Torre, Kinetic model for ye'elimite polymorphs formation during clinkering production of CSA cement, Constr. Build. Mater. 321 (2022). https://doi.org/10.1016/j.conbuildmat.2022.126336.

[101] P. Ptáček, T. Opravil, F. Šoukal, J. Havlica, R. Holešinský, Kinetics and mechanism of formation of gehlenite, Al-Si spinel and anorthite from the mixture of kaolinite and calcite, Solid State Sci. 26 (2013) 53–58. https://doi.org/10.1016/j.solidstatesciences.2013.09.014.

[102] Z. Yan, Z. Wang, H. Liu, Y. Tu, W. Yang, H. Zeng, J. Qiu, Decomposition and solid reactions of calcium sulfate doped with SiO2, Fe2O3 and Al2O3, J. Anal. Appl. Pyrolysis 113 (2015) 491–498. https://doi.org/10.1016/j.jaap.2015.03.019.

[103] A. Berrio, C. Rodriguez, J.I. Tobón, Effect of Al2O3/SiO2 ratio on ye'elimite production on CSA cement, Constr. Build. Mater. 168 (2018) 512–521. https://doi.org/10.1016/j.conbuildmat.2018.02.153.

[104] N. Böhme, K. Hauke, M. Neuroth, T. Geisler, In situ Raman imaging of high-temperature solid-state reactions in the CaSO4–SiO2 system, Int. J. Coal Sci. Technol. 6 (2019) 247–259. https://doi.org/10.1007/s40789-019-0252-7.

[105] P. Arjunan, M.R. Silsbee, D.M. Roy, Sulfoaluminate-belite cement from low-calcium fly ash and sulfur-rich and other industrial by-products, Cem. Concr. Res. 29 (1999) 1305–1311. https://doi.org/10.1016/S0008-8846(99)00072-1.

[106] J.C. Jumas, A. Goiffon, B. Capelle, A. Zarka, J.C. Doukhan, J. Schwartzel, J. Détaint, E. Philippot, Crystal growth of berlinite, AlPO4: Physical characterization and comparison with quartz, J. Cryst. Growth 80 (1987) 133–148. https://doi.org/10.1016/0022-0248(87)90533-1.

[107] B. Nasiri-Tabrizi, A. Fahami, Reaction mechanisms of synthesis and decomposition of fluorapatite-zirconia composite nanopowders, Ceram. Int. 39 (2013) 5125–5136. https://doi.org/10.1016/j.ceramint.2012.12.008.

[108] F.Z. Mezahi, H. Oudadesse, A. Harabi, A. Lucas-Girot, Y. Le Gal, H. Chaair, G. Cathelineau, Dissolution kinetic and structural behaviour of natural hydroxyapatite vs. thermal treatment : CComparison to synthetic hydroxyapatite, J. Therm. Anal. Calorim. 95 (2009) 21–29. https://doi.org/10.1007/s10973-008-9065-4.

[109] S. Agathopoulos, D.U. Tulyaganov, P.A.A.P. Marques, M.C. Ferro, M.H.V. Fernandes, R.N. Correia, The fluorapatite-anorthite system in biomedicine, Biomaterials 24 (2003) 1317–1331. https://doi.org/10.1016/S0142-9612(02)00468-4.

[110] A. Boumaza, L. Favaro, J. Lédion, G. Sattonnay, J.B. Brubach, P. Berthet, A.M. Huntz, P. Roy, R. Tétot, Transition alumina phases induced by heat treatment of boehmite: An X-ray diffraction and infrared spectroscopy study, J. Solid State Chem. 182 (2009) 1171–1176. https://doi.org/10.1016/j.jssc.2009.02.006.

[111] Y. Tian, X. Pan, H. Yu, G. Tu, Formation mechanism of calcium aluminate compounds based on high-temperature solid-state reaction, J. Alloys Compd. 670 (2016) 96–104. https://doi.org/10.1016/j.jallcom.2016.02.059.

[112] M. Rafienia, A. Bigham, A. Saudi, S. Rahmati, Gehlenite nanobioceramic: Sol-gel synthesis, characterization, and in vitro assessment of its bioactivity, Mater. Lett. 225 (2018) 89–92. https://doi.org/10.1016/j.matlet.2018.04.094.

[113] M.A. Mahdy, I.K. El Zawawi, S.H. Kenawy, E.M.A. Hamzawy, G.T. El-Bassyouni, Effect of zinc oxide on wollastonite: Structural, optical, and mechanical properties, Ceram. Int. 48 (2022) 7218–7231. https://doi.org/10.1016/j.ceramint.2021.11.282.

[114] N. Doebelin, R. Kleeberg, Profex: A graphical user interface for the Rietveld refinement program BGMN, J. Appl. Crystallogr. 48 (2015) 1573–1580. https://doi.org/10.1107/S1600576715014685.

[115] K. Belhouchet, A. Bayadi, H. Belhouchet, M. Romero, Improvement of mechanical and dielectric properties of porcelain insulators using economic raw materials, Bol. La Soc. Esp. Ceram. y Vidr. 58 (2019) 28–37. https://doi.org/10.1016/j.bsecv.2018.05.004.

[116] P. Bai, Y. Chai, Y. Qiu, C. Gong, Y. Tian, P. Bai, The effect of sintering temperature on prepared and properties of calcium hexaluminate/gehlenite composites, Sci. Sinter. 46 (2014) 315–321. https://doi.org/10.2298/SOS1403315B.

[117] R. Li, J. Zhang, W. He, D. Nie, Y. Zhang, Preparation of belite-sulfoaluminate cement with phosphate-rock acid-insoluble residue: Modification and influence of impurity ions on cement properties, Constr. Build. Mater. 365 (2023) 130077. https://doi.org/10.1016/j.conbuildmat.2022.130077.

[118] S. Wu, X. Yao, Y. Yao, C. Ren, C. Wu, C. Zhang, W. Wang, Recycling phosphogypsum as the sole calcium oxide source in calcium sulfoaluminate cement production and solidification of phosphorus, Sci. Total Environ. 808 (2022) 152118. https://doi.org/10.1016/j.scitotenv.2021.152118.

[119] C. Domínguez, J. Chevalier, R. Torrecillas, G. Fantozzi, Microstructure development in calcium hexaluminate, J. Eur. Ceram. Soc. 21 (2001) 381–387. https://doi.org/10.1016/S0955-2219(00)00143-6.

[120] A. Chithra, P. Wilson, S. Vijayan, R. Rajeev, K. Prabhakaran, Robust thermally insulating carbon-gehlenite composite foams from newspaper waste and sucrose by filter-pressing, Mater. Des. 160 (2018) 65–73. https://doi.org/10.1016/j.matdes.2018.09.005.

[121] H. Li, R. Wang, W. Zhao, H. Guo, B. Yan, P. Li, Sintered glass-ceramic foams from fluorite tailings and waste glass with calcium phosphate addition, Constr. Build. Mater. 359 (2022) 129528. https://doi.org/10.1016/j.conbuildmat.2022.129528.

[122] J. Khajornboon, K. Ota, K. Washijima, T. Shiono, Control of hexagonal plate-like microstructure of in-situ calcium hexaluminate in monolithic refractories, J. Asian Ceram. Soc. 6 (2018) 196–204. https://doi.org/10.1080/21870764.2018.1484621.

[123] F. Chouia, H. Belhouchet, F. Sahnoune, F. Bouzrara, Reaction sintering of kaolin-natural phosphate mixtures, Ceram. Int. 41 (2015) 8064–8069. https://doi.org/10.1016/j.ceramint.2015.03.003.

[124] P. Bakshi, A. Pappu, D. Kumar Bharti, Transformation of flue gas desulfurization (FGD) gypsum to β-CaSO4·0.5H2O whiskers using facile water treatment, Mater. Lett. 308 (2022). https://doi.org/10.1016/j.matlet.2021.131177.

[125] I. Birken, M. Bertucci, J. Chappelin, E. Jorda, Quantification of Impurities, Including Carbonates Speciation for Phosphates Beneficiation by Flotation, Procedia Eng. 138 (2016) 72–84. https://doi.org/10.1016/j.proeng.2016.02.059.

[126] V.A. Abyzov, Lightweight Refractory Concrete Based on Aluminum-Magnesium-Phosphate Binder, Procedia Eng. 150 (2016) 1440–1445. https://doi.org/10.1016/j.proeng.2016.07.077.

[127] C. Ren, S. Wu, W. Wang, L. Chen, Y. Bai, T. Zhang, H. Li, Y. Zhao, Recycling of hazardous and industrial solid waste as raw materials for preparing novel high-temperature-resistant sulfoaluminate-magnesia aluminum spinel cement, J. Build. Eng. 64 (2023) 105550. https://doi.org/10.1016/j.jobe.2022.105550.

[128] S. Sinhamahapatra, K. Dana, S. Mukhopadhyay, H.S. Tripathi, Role of different rare earth oxides on the reaction sintering of magnesium aluminate spinel, Ceram. Int. 45 (2019) 11413–11420. https://doi.org/10.1016/j.ceramint.2019.03.007.

[129] M. Hidouri, K. Bouzouita, F. Kooli, I. Khattech, Thermal behaviour of magnesium-containing fluorapatite, Mater. Chem. Phys. 80 (2003) 496–505. https://doi.org/10.1016/S0254-0584(02)00553-9.

[130] S. Kobayashi, T. Murakoshi, Effects of MgO addition on sintering of calcium phosphate ceramics and composites, Adv. Compos. Mater. 24 (2015) 137–146. https://doi.org/10.1080/09243046.2014.957373.

[131] R. Dabbebi, J.L.B. de Aguiar, B. Samet, S. Baklouti, Mineralogical and chemical investigation of Tunisian phosphate washing waste during calcination, J. Therm. Anal. Calorim. 137 (2019) 1827–1840. https://doi.org/10.1007/s10973-019-08057-3.

[132] S. Sanjabi, A. Obeydavi, Synthesis and characterization of nanocrystalline MgAl2O4 spinel via modified sol-gel method, J. Alloys Compd. 645 (2015) 535–540.

https://doi.org/10.1016/j.jallcom.2015.05.107.

[133] S.J. Kim, H.G. Bang, J.H. Song, S.Y. Park, Effect of fluoride additive on the mechanical properties of hydroxyapatite/alumina composites, Ceram. Int. 35 (2009) 1647–1650. https://doi.org/10.1016/j.ceramint.2008.07.016.

[134] A. Bandyopadhyay, S. Bernard, W. Xue, S. Böse, Calcium phosphate-based resorbable ceramics: Influence of MgO, ZnO, and SiO 2 dopants, J. Am. Ceram. Soc. 89 (2006) 2675–2688. https://doi.org/10.1111/j.1551-2916.2006.01207.x.

[135] M. Kheradmandfard, M.H. Fathi, Fabrication and characterization of nanocrystalline Mg-substituted fluorapatite by high energy ball milling, Ceram. Int. 39 (2013) 1651–1658. https://doi.org/10.1016/j.ceramint.2012.08.007.

[136] Y. Huang, J. Qian, X. Kang, J. Yu, Y. Fan, Y. Dang, W. Zhang, S. Wang, Belite-calcium sulfoaluminate cement prepared with phosphogypsum: Influence of P 2 O 5 and F on the clinker formation and cement performances, Constr. Build. Mater. 203 (2019) 432–442. https://doi.org/10.1016/j.conbuildmat.2019.01.112.

[137] J. Yu, J. Qian, H. Chen, Y. Ji, D. Kuang, X. Jia, B. Guan, Behavior of magnesium phosphate cement with addition of sulphoaluminate cement at elevated temperatures, Constr. Build. Mater. 401 (2023) 132932. https://doi.org/10.1016/j.conbuildmat.2023.132932.

[138] S.S. Milani, M.G. Kakroudi, M. Rezvani, The effects of processing technique on formation temperature of calcium aluminate magnesium (CaO.2MgO.8Al2O3), J. Cryst. Growth 643 (2024) 127797. https://doi.org/10.1016/j.jcrysgro.2024.127797.

[139] S. Kannan, A.F. Lemos, J.H.G. Rocha, J.M.F. Ferreira, Characterization and mechanical performance of the Mg-stabilized β-Ca3(PO4)2 prepared from Mg-substituted Ca-deficient apatite, J. Am. Ceram. Soc. 89 (2006) 2757–2761. https://doi.org/10.1111/j.1551-2916.2006.01158.x.

Materials and Structures (2024) 57:234
https://doi.org/10.1617/s11527-024-02511-x

ORIGINAL ARTICLE

The effect of quartz on natural fluorapatite decomposition during the preparation of calcium sulfoaluminate-based multiphase composites

Zeyneb Hammou · Hocine Belhouchet

Received: 21 August 2024 / Accepted: 2 November 2024 / Published online: 18 November 2024

Abstract In the research described in this paper, we prepared low-cost multiphase composites based on calcium sulfoaluminate (also known as ye'elimite) and fluorapatite. By utilizing the CaO originally present in fluorapatite, the sintering densification of these composites was enhanced. The influence of varying the SiO_2 content (0–5.4 wt.%) on the reactive sintering of fluorapatite, bauxite, and gypsum was investigated. Incorporating quartz led to the formation of various compositions, including calcium hexaluminate, fluorapatite, ye'elimite, and gehlenite. Quantitative phase analysis, conducted using the Rietveld method via Profex software at various sintering temperatures, demonstrated a relationship between quartz content and the preferential formation of gehlenite over ye'elimite within the 1300–1350 °C range. Additionally, the microstructure of the composites was significantly modified by quartz addition, leading to the development of hexagonal and circular grains after heat treatment at 1400 °C.

Z. Hammou (✉)
Laboratory of Physics and Chemistry of Materials, Faculty of Sciences, University of M'sila, University Pole, Road Bourdj Bou Arreiridj, 28000 M'sila, Algeria
e-mail: zeyneb.hammou@univ-msila.dz

Z. Hammou · H. Belhouchet
Physics Department, Faculty of Sciences, University of M'sila, University Pole, Road Bourdj Bou Arreiridj, 28000 M'sila, Algeria
e-mail: hocine.belhouchet@univ-msila.dz

Keywords Fluorapatite · Ye'elimite · Gehlenite · Calcium sulfoaluminate · Quartz

Abbreviations

C	CaO
A	Al_2O_3
$	SO_3
$\overline{C}$	CO_2
S	SiO_2
H	H_2O
P	P_2O_5

1 Introduction

The cement industry, particularly the production of Portland cement, is a major contributor to CO_2 emissions, which has led to increased research into more environmentally friendly alternatives [1, 2]. Calcium sulfoaluminate (CSA) cement ($Ca_4Al_6O_{12}(SO_4)$ or $C_4A_3\$$ in cement notation) is an alternative to traditional Portland cement and is produced by burning limestone, bauxite, and gypsum to form ye'elimite [3, 4]. Recent studies on ye'elimite formation have provided valuable insights into its synthesis and applications in high-performance cementitious materials for construction. Researchers have explored various phases and microstructures during different stages of formation, thereby enhancing the understanding of raw material interactions and potentially leading to more efficient calcium sulfoaluminate cement

ARTICLE IN PRESS

Ceramics International xxx (xxxx) xxx

Contents lists available at ScienceDirect

Ceramics International

journal homepage: www.elsevier.com/locate/ceramint

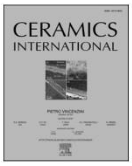

The influence of magnesium oxide on natural fluorapatite decomposition during the preparation of ye'elimite-spinel based multi-phase composites

Zeyneb Hammou [a,b], Hocine Belhouchet [b,*], Mohammad R. Irshidat [c], Mujaheed Pasha [d], Umar Amjad [c]

[a] *Laboratory of Physics and Chemistry of Materials, Faculty of Sciences, University Mohamed Boudiaf of M'sila, 28000, M'sila, Algeria*
[b] *Physics Department, Faculty of Sciences, University Mohamed Boudiaf of M'sila, 28000, M'sila, Algeria*
[c] *Center for Advanced Materials (CAM), Qatar University, P.O. Box 2713, Doha, Qatar*
[d] *Core Laboratories, Hamad Bin Khalifa University (HBKU), Qatar Foundation, Doha, Qatar*

ARTICLE INFO

Handling Editor: Dr P. Vincenzini

Keywords:
Natural fluorapatite
Ye'elimite
Spinel
Sintering behavior
Rietveld method
Refractories

ABSTRACT

This study investigates the development of compounds based on ye'elimite-spinel, which incorporates magnesium oxide (MgO) and fluorapatite. Utilizing natural fluorapatite as a raw material not only provides a cost-effective source of calcium oxide but also reduces the dependency on limestone, thereby decreasing CO_2 emissions linked to decarbonization. This research presents an in-depth analysis of the sintering behavior and phase transformations of ceramic materials. Techniques such as X-Ray diffraction (XRD), Rietveld method, SEM-EDS, FT-IR, and TG/DTG were employed to explore the effects of temperature (ranging from 1000 to 1500 °C) and varying MgO content (0–6 wt%) on phase formation, including fluorapatite, ye'elimite, spinel, and other high-temperature phases like hibonite, beta-tricalcium phosphate, and grossite. These findings indicate that increasing MgO content promotes the formation of spinel while stabilizing ye'elimite at higher temperatures. The results provide valuable insights for optimizing the composition and thermal properties of these composites for high-temperature applications, such as cements, refractories, and advanced ceramics.

1. Introduction

The cement industry is a leading source of global CO_2 emissions, mainly due to the production of Portland cement. This environmental impact has led to a global effort to develop alternative low-carbon binding materials to meet climate goals, comply with stricter regulations, and satisfy market demands for sustainable construction solutions. Researchers are now exploring various alternatives, including calcium sulfoaluminate (CSA) cements, belite-ye'elimite-based binders, and magnesium-based binders, each offering potential environmental benefits by lowering CO_2 emissions and improving resource efficiency [1–3]. However, while these alternatives promise significant reductions in carbon output, they face challenges in achieving the performance, durability, scalability, and cost-effectiveness required to match traditional Portland cement [4].

One promising alternative is ye'elimite-based cement, which has gained attention owing to its low carbon footprint and unique properties. Ye'elimite ($Ca_4Al_6O_{12}SO_4$) is a calcium sulfoaluminate mineral that forms the primary component of CSA cement. The production of ye'elimite clinker involves burning a mixture of limestone, bauxite, and gypsum at high temperatures [5,6]. Although this process still releases CO_2 owing to the decarbonation of limestone, it offers a lower overall carbon footprint compared to traditional clinker production [7,8]. To further reduce emissions, researchers have investigated the incorporation of noncarbonated calcium sources. A promising candidate for decarbonized raw materials is natural phosphate or phosphorite, a sedimentary rock rich in phosphate minerals [9]. Its primary constituent, fluorapatite ($Ca_{10}(PO_4)_6F_2$), is a valuable alternative to limestone in cement production. Fluorapatite incorporation into cement can significantly lower CO_2 emissions by reducing the need for limestone decomposition and optimizing the energy use during manufacturing [10,11]. The flexibility of the fluorapatite crystal structure allows for the incorporation of various ions, specifically K^{+}, Na^{+}, Zn^{2+}, Mg^{2+}, Sr^{2+}, Ba^{2+}, Fe^{2+}, Pb^{2+}, Zn^{2+}, Ce^{3+}, Al^{3+} for Ca^{2+} substitutions; As, Si, V, and CO_3^{2-} for PO_4^{3-} substitutions, and OH^{-}, Cl^{-}, and O^{2-} for F^{-} substitutions [12]. These substitutions can significantly affect fluorapatite decomposition and alter its mechanical properties. Understanding these substitutions through techniques such as FTIR analysis is crucial for optimizing and

---

* Corresponding author.
E-mail address: hocine.belhouchet@univ-msila.dz (H. Belhouchet).

https://doi.org/10.1016/j.ceramint.2025.03.332
Received 11 November 2024; Received in revised form 22 March 2025; Accepted 23 March 2025

Please cite this article as: Zeyneb Hammou et al., *Ceramics International*, https://doi.org/10.1016/j.ceramint.2025.03.332

Abstract

Cement production is considered a fundamental element in the construction industry, but it contributes significantly to environmental pollution, as it emits one ton of carbon dioxide for every ton of cement produced, representing 5% of global carbon emissions. To address this environmental challenge, scientists are researching the development of more environmentally sustainable alternatives such as ye'elimite-based cement, which is characterized by low carbon emissions and reduced need for limestone in the production process. In the research presented in this thesis, we prepared multi-phase composites based on ye'elimite, using natural phosphate (fluorapatite) from Djebel El Onk in Algeria as an alternative source of CaO instead of limestone. This study also investigates the effect of oxide additives such as natural quartz and magnesium oxide on the behavior and decomposition characteristics of fluorapatite.

The study examined the influence of varying SiO_2 content (0-5.4 wt%) on the reactive sintering of mixtures containing fluorapatite, bauxite, and gypsum. The resulting composites included multiple phases such as calcium hexaluminate, fluorapatite, ye'elimite, and gehlenite. Quantitative Rietveld analysis revealed that increased quartz content promoted gehlenite formation over ye'elimite at 1300-1350 °C, while also significantly modifying the microstructure-leading to the development of hexagonal and circular grains after heat treatment at 1400 °C. In addition, we examined the effect of MgO on the decomposition of natural fluorapatite during the synthesis of spinel-ye'elimite-based multiphase composites. Using advanced analytical techniques (XRD, Rietveld method, SEM-EDS, FTIR, and TG/DTG), we investigated the influence of temperature (1000-1500 °C) and MgO content (0-6 wt%) on phase formation, including fluorapatite, ye'elimite, spinel, hibonite, beta-tricalcium phosphate, and grossite. The results demonstrate that higher MgO content promotes spinel formation and stabilizes ye'elimite at elevated temperatures.

Keywords: Cement; Natural Phosphate; Fluorapatite; Calcium Sulfoaluminate; Ye'elimite; Rietveld Method.

الملخص

إنتاج الأسمنت يعتبر عنصراً أساسياً في صناعة البناء، لكنه يساهم بشكل كبير في التلوث البيئي، حيث ينبعث منه طن واحد من ثاني أكسيد الكربون لكل طن من الأسمنت المُنتج، مما يمثل 5% من انبعاثات الكربون العالمية. لمواجهة هذا التحدي البيئي، يبحث العلماء في تطوير بدائل أكثر استدامة بيئيا مثل الأسمنت القائم على اليليميت، والذي يتميز بانبعاثات كربونية منخفضة وحاجة أقل للحجر الجيري في عملية الإنتاج. في البحث المقدم في هذه الأطروحة، قمنا بإعداد مركبات متعددة الأطوار قائمة على اليليميت، باستخدام الفوسفات الطبيعي (فلوراباتيت) من جبل العنق في الجزائر كمصدر بديل لأكسيد الكالسيوم بدلاً من الحجر الجيري. كما تبحث هذه الدراسة أيضاً في تأثير إضافات الأكاسيد مثل الكوارتز الطبيعي وأكسيد المغنيسيوم على سلوك وخصائص تفكك الفلوراباتيت.

تناولت هذه الدراسة أيضا كيفية تأثير محتوى ثاني أكسيد السيليكون (0-5.4%) على التلبيد التفاعلي لخليط مكون من الفلورأباتيت والبوكسيت والجبس، مما أدى إلى ظهور عدة أطوار تشمل هيكسالومينيت الكالسيوم، والفلورأباتيت، واليليميت، والجيلينيت. أظهر تحليل ريتفيلد الكمي أن زيادة محتوى الكوارتز عززت تكوين الجيلينيت على حساب اليليميت عند درجات حرارة تتراوح بين 1300 و1350 درجة مئوية، كما أحدثت تغييرًا كبيرًا في البنية المجهرية، مما أدى إلى تكوين حبيبات سداسية ودائرية بعد المعالجة الحرارية عند 1400 درجة مئوية.

بالإضافة إلى ذلك، قمنا بفحص تأثير MgO على تفكك الفلوراباتيت الطبيعي أثناء تحضير المركبات متعددة الأطوار القائمة على السبينال-اليليميت. باستخدام تقنيات التحليل المتقدمة (XRD، طريقة ريتفيلد، SEM-EDS، FTIR، وTG/DTG)، مع فحص تأثير درجة الحرارة (1000-1500 درجة مئوية) ومحتوى MgO (0-6% بالوزن) على تكوين الأطوار، بما في ذلك الفلوراباتيت واليليميت والسبينال والهيبونيت وبيتا-فوسفات الكالسيوم الثلاثي والغروسيت. تظهر النتائج أن زيادة محتوى MgO يعزز تكوين السبينال ويثبت اليليميت عند درجات الحرارة العالية.

الكلمات المفتاحية: الأسمنت؛ الفوسفات الطبيعي؛ الفلوروأباتيت؛ سلفوألومينات الكالسيوم؛ اليليميت؛ طريقة ريتفيلد.